ISAS RESEARCH NOTE

ISAS RN 752

Contributions to SPIE Conference 4851 entitled X-ray and Gamma-ray Telescopes and Instruments for Astronomy

Y. Haba, H. Kunieda, Y. Maeda, K. Misaki,
H. Mori, R. Shibata, et al.

THE INSTITUTE OF SPACE AND ASTRONAUTICAL SCIENCE

THE INSTITUTE OF SPACE AND ASTRONAUTICAL SCIENCE
YOSHINODAI, SAGAMIHARA, KANAGAWA 229-8510

ISAS RESEARCH NOTE

ISAS RN 752

Contributions to SPIE Conference 4851 entitled X-ray and Gamma-ray Telescopes and Instruments for Astronomy

Y. Haba[a,b], H. Kunieda[a], Y. Maeda[a], K. Misaki[a], H. Mori[a], R. Shibata[a,b], et al.

November 2002

[a] *High Energy Astrophysics Division, Institute of Space and Astronautical Science, Yoshinodai, Sagamihara, Kanagawa 229-8510*
[b] *Department of Physics, Faculty of Science, Nagoya University, Furo-cho, Chikusa, Nagoya, Aichi 464-8602*

SPIE Conference 4851
"X-ray and Gamma-ray Telescopes and Instruments for Astronomy"
Waikoloa, Hawaii USA, August 24 – 28, 2002

Contents

Error budgets for the image degradation of X-ray telescope on board Astro-E

Kazutami Misaki[a], Ryo Shibata[b], Yasuhiro Hidaka[a], Hideyo Kunieda[a], Manabu Ishida[c], Hirohiko Honda[a], Yoshitomo Maeda[a], Takao Endo[a], Kohsuke Imamura[a], Yoshito Haba[a], Kei Itoh[a], Hideyuki Mori[a], Ryo Iizuka[a], Akira Hayakawa[c], Taijiro Morihisa[a]

[a]High Energy Astrophysics Division, Institute of Space and Astronautical Science, 3-1-1 Yoshinodai, Sagamihara, Kanagawa, 229-8510, Japan
[b]Department of Physics, Faculty of Science, Nagoya University, Furo-cho, Chikusa, Nagoya, Aichi, 464-8602, Japan
[c]Department of Physics, Tokyo Metropolitan University, 1-1 Minami-Osawa, Hachioji, Tokyo, 192-0397, Japan

ABSTRACT

X-ray telescopes (XRTs) of nested thin foil mirrors were developed for Astro-E, the fifth Japanese x-ray astronomy satellite. Although the launch was not successful, the re-flight of Astro-E mission is approved as Astro-E2 and will carry the same XRTs. Ground-based calibration of Astro-E XRT revealed that its image quality and effective area are somewhat worse than what are expected from the original design. Conceivable causes of these defects of the XRT performance (i.e., surface roughness, waviness, misalignment of reflectors, and so on) are examined by X-rays and optical microscopic measurements. In this paper, we distinguish quantitatively these causes to limit the performance of the Astro-E XRT. Using the detail measurements, we can attribute both degradation of the image quality and a deficit of the effective area from the design values mainly to a slope error with a mm scale in each reflector and shadowing effects of neighboring reflectors due to various factors. There is still room for improvement in the support system of reflectors (i.e., alignment bars) in the XRT. One of the main aims of the mirror system calibration is to construct response function. Therefore, it is important that the development of a representative numerical model and its validation against extensive ground-based calibration. Taking account of the results of the pre-flight calibration and the microscopic measurements, we develop and tune a ray-tracing simulator which constructs the XRT response function for a point source at an arbitrary off-axis angle and spatial distributions of celestial X-ray sources.

Keywords: X-ray telescope, surface waviness, Astro-E, Astro-E2, ray-tracing

1. INTRODUCTION

Astro-E is the fifth Japanese X-ray astronomy satellite which aims at high resolution spectroscopy and imaging in the band 0.5–10 keV with the X-Ray Spectrometer (XRS; X-ray microcalorimeter) and the X-ray Imaging Spectrometer (XIS: X-ray CCD camera), respectively, as well as covering the hard X-ray band $10 - 600$ keV simultaneously with the Hard X-ray Detector (HXD; phoswitch scintillator). In order to achieve a large photon-collecting area and a high signal-to-noise ratio, X-Ray telescopes (XRTs) are introduced for the XRS and the XIS.

Astro-E XRT is designed with the conical approximation of Wolter-I type optics. For high throughput within a severely limited weight allowance, an aluminum foil as thin as $\sim$160 μm was used for the reflector substrate, and nested as many as possible within geometrical constraint. We thus achieved the aperture efficiency of $\sim$50 %, which is the greatest among all the Wolter-I type telescopes so far in orbit. Due to the thin substrate, on the other hand, it is difficult to retain the reflectors in the ideal shapes required by the original Wolter-I optics (paraboloid and hyperboloid for the primary and secondary reflectors, respectively). Accordingly, we

Kazutami Misaki: E-mail: misaki@astro.isas.ac.jp, Telephone: +81-42-759-8138

approximated both the primary and secondary reflectors by cones. This conical approximation was also adopted for ASCA,[1-3] the previous Japanese X-ray astronomy satellite launched in 1993 February. The effective area and the imaging quality of Astro-E, however, are expected to be significantly better than those of ASCA, owing to a moderate scale-up and the replication process newly introduced.[4]

We prepared two types of XRTs according to two different types of detectors on board Astro-E. One is for the XIS, which is designated as XRT-I. XRT-I has a focal length of 4.75 m with reflectors' surface coated with gold. Totally 175 such reflectors with slightly different radii are arranged coaxially to have a common focus. The other is for the XRS, which is named XRT-S. XRT-S has a focal length of 4.50 m with 168 reflectors coated with platinum. The designed effective area per XRT module is $570-580$ cm^2 and $340-350$ cm^2 at 1.5 keV and 8.0 keV, respectively, for both XRT-I and XRT-S. The conical approximation gives half power diameter (HPD), a measure of the imaging capability, of 15 arcsec for both. On Astro-E were mounted four modules of XRT-I and one module of XRT-S. A picture and drawings of the XRT are shown in Fig. 1 and Fig. 2, respectively. As for the mechanical design, the expected performance including an effective area and imaging capability, fabrication, and an interface to the satellite, more details were fully described in Kunieda et al..[4]

Pre-flight calibration of Astro-E XRTs revealed that its image quality and effective area are somewhat worse than what are expected from the original design. These results of the ground-based X-ray characterization of the Astro-E XRT are summarized in Shibata et al.[5] in detail. To put it briefly, the effective area amounts only to $70-80$ % of the designed value, as shown in Table 1. The deficit of the effective area is larger at higher energies. On the image quality, HPD was also found to be 2 arcmin on the average, which is eight times worse than that calculated from the design.

Table 1. Effective Area of the Astro-E XRT. The quoted errors are twice as many as the standard deviation of the measured values of the individual quadrants.

XRT-S (Pt)			
Energy [keV]	Measured [cm^2]	Ideal [cm^2]	Ratio (Measured/Ideal) [%]
1.49	465 ± 3.1	582.7	79.8 ± 0.5
4.51	353 ± 2.2	439.3	80.4 ± 0.5
8.04	255 ± 1.2	344.5	74.0 ± 0.4
9.44	180 ± 1.2	244.9	73.5 ± 0.5
XRT-I (Au)			
Energy [keV]	Measured [cm^2]	Ideal [cm^2]	Ratio (Measured/Ideal) [%]
1.49	440.2 ± 8.7	566.5	77.7 ± 1.6
4.51	322.5 ± 5.2	419.8	77.0 ± 1.3
8.04	241.4 ± 4.0	340.2	71.0 ± 1.2
9.44	172.5 ± 3.4	244.5	70.6 ± 1.4

In this paper, we attempt to clarify the reasons leading to such performance degradation of the XRT, by inspecting components such as individual reflectors and their alignments. In § 2, we present results from measurements of individual reflectors. Section 3 is devoted to describe performance of a single pair of the primary and secondary reflectors. Synthesizing all the results above, we described the development of a representative numerical model and its validation against extensive ground-based calibration in § 4. We develop and tune a ray-tracing simulator which constructs the XRT response function.

The Astro-E satellite, after failure of launch in 2000 February, will revive in early 2005 as the Astro-E2 satellite. The response function of Astro-E will be applicable for Astro-E2 essentially. In addition, this study is quite important for the future developments to pursue higher throughput and better imaging capability. If we can resolve the performance degradation into its causes quantitatively, the points to be improved are identified clearly.

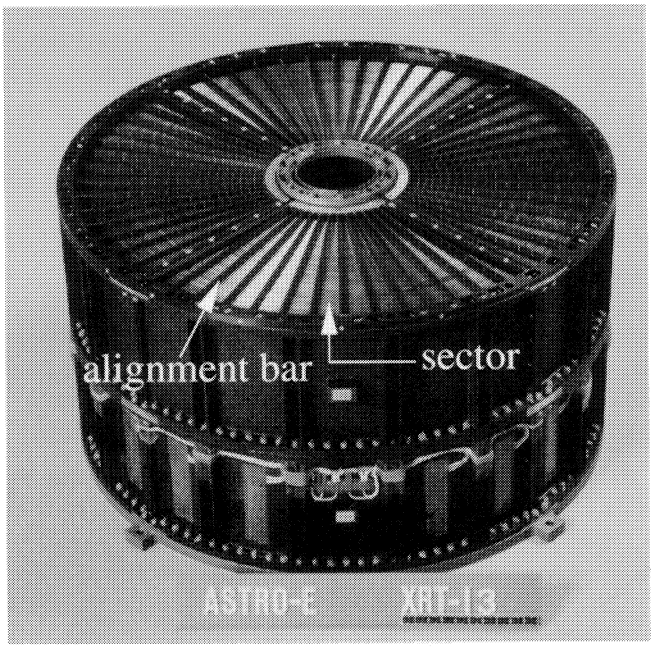

Figure 1. Astro-E XRT-I (without thermal shield).

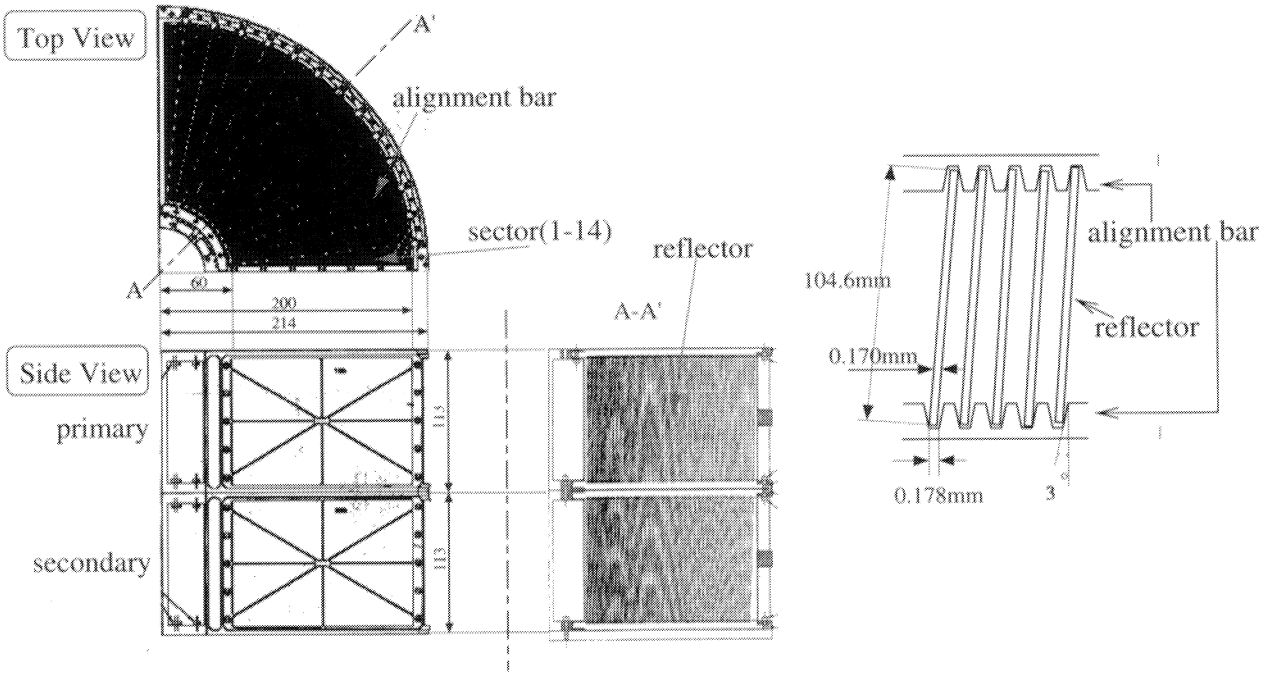

Figure 2. Quadrant of Astro-E XRT. The XRT shown in Fig. 1 consists of four equivalent quadrants of housings. Top left; the top view of a quadrant with 175 coaxial reflector shells and 13 radial spokes, called alignment bars. Bottom left; the side view of a housing in two stages (primary and secondary). Bottom right; the cross section of a housing, where each conical shell is supported by the grooves of the alignment bars on the top and bottom sides. The close-up view of reflectors in the grooves are shown in the right panel.

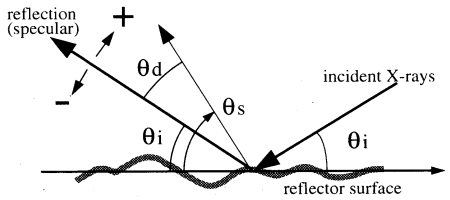

Figure 3. Definition of the angles used in the measurements. θ_i, θ_d, and θ_s denote incident angle, diffraction angle, and scattered angle, respectively. $\theta_d = \theta_s - \theta_i$.

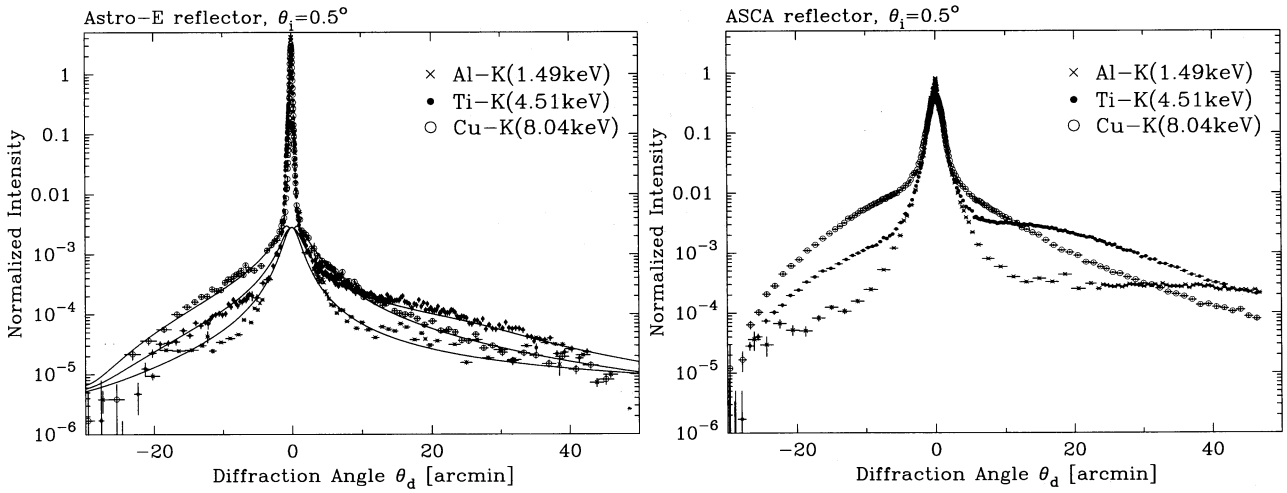

Figure 4. X-ray reflected profiles (left:Astro-E, right:ASCA). The abscissa indicates the diffraction angle θ_d. Intensity is normalized by total reflectivity. The results for 1.49 keV (cross), 4.51 keV (filled circle), and 8.04 keV (open circle) are shown. The scattered tail of Astro-E is well fitted by the PSD model plus Lorentzian which is indicated by smooth curves. Note that the same PSD model is applied to each energy, although the fitted curves appear separately according to the energy. See text in detail.

2. MEASUREMENTS OF INDIVIDUAL SINGLE REFLECTORS

In this section, we investigate characteristics of the surface of the Astro-E reflectors before installation into the housing of telescope. Various measuring devices and methods were used for characterization of the reflector surfaces. We formulate angular distribution of reflected X-rays incorporating these measurements data as described below.

2.1. Surface Roughness

2.1.1. X-ray reflected profile — scattered tail

We measured X-ray beam profiles reflected from the Astro-E reflectors using X-ray pencil beam of 0.1 mm at Nagoya University 10 m X-ray beam facility.[6] The incident angle (θ_i) is fixed at 0.5 degree which is the typical value of Astro-E XRT. Accordingly, the narrow X-ray beam illuminates about 10 mm projectional area of the reflector. The detector was a CCD, which has a 1024 × 1024 array of pixels whose size is 24 μm. The angle resolved scatters are measured from θ_d of -30 arcmin to $+50$ arcmin, θ_d is the diffraction angle from the direction of the specular reflection (Fig. 3). The measurements were carried out at three different energies, 1.49 keV (Al-Kα), 4.51 keV (Ti-Kα), and 8.04 keV (Cu-Kα), which are monochromatized by using a double-crystal monochrometer.

The obtained profiles are shown in Fig. 4, together with those from the reflectors used in the previous mission ASCA for comparison. Comparing with the ASCA reflector, we found that the level of the scattered tail of

the Astro-E's decreased roughly by an order of magnitude. These results indicate that the surface roughness has been reduced by introduction of the replication method in forming the reflector surface.[4] The level of the scattered tail of the Astro-E reflector is smaller than the peak of the specular component by four orders of magnitude.

The distribution of scattered X-rays reflects the small-scale structure on mirror surface. According to the Rayleigh-Rice vector perturbation theory,[7] the angular distribution of scattered photons can be estimated from the power spectral density (PSD) of the mirror surface as follows;

$$\frac{dI}{d\theta_s} = \frac{16\pi^2}{\lambda^3} \sin\theta_i \sin^2\theta_s \sqrt{\frac{R(\theta_s)}{R(\theta_i)}} \times PSD(f), \tag{1}$$

where $R(\theta)$ is the reflectivity for the incident grazing angle θ. PSD(f) is the monodimensional power spectral density of the mirror surface. The monodimensional scatter theory is a useful approximation for grazing incidence mirrors.[9] The relation between the surface spatial frequency f and the angle of scattering θ_s is given by the grating equation applied to the first order of diffraction

$$f = \frac{\cos\theta_i - \cos\theta_s}{\lambda}. \tag{2}$$

From equations 1 and 2 we can derive PSD of the Astro-E reflectors, which is shown in the bottom right-hand side of Fig. 5 ("X-ray scattering"). PSD of the Astro-E reflector is much less than that of ASCA by about one order of magnitude. Comparing the level of the derived PSD with those of Chandra[8] and XMM[9] in the region of surface wavelength of 1–30 μm, the surface roughness of the Astro-E reflector keeps the same level of the XMM reflector and comes close to Chandra.

The PSDs from Cu-Kα and Ti-Kα measurements agree very well, while the data from Al-Kα tend to exceed them slightly. This discrepancy is probably due to a contribution of the skirt (skewed wing) of specular reflection, which is originated from large figure errors treated in geometrical optics. It must be noted that the intensity of scattering strongly depends on the wavelength λ^{-3} (see Equation 1), while the distribution of the specular component is independent of λ. Thus, we may well assume that the excess of data of Al-Kα is caused by the skirt of deviations of specular reflection that is prominent only at the Al-Kα wavelength. Introducing Lorentzian to represent the skewed wing of the specular component, all the scattering tails measured at the three energies are well described with the PSD model plus Lorentzian wings which is indicated by solid lines in the left panel of Fig. 4. As is suggested by the linear fit in the log-log space (Fig. 5), the best-fit PSD function is a power-law form; $5.2 \times 10^{-9} \times f^{-1.25}$ with a cut-off around θ_d of 2 arcmin where is the boundary between the scattered tail and specular core. As for Lorentzian, obtained best-fit value of the normalization constant N_{lo} and the full width at half maximum σ_{lo} are 2.85×10^{-3} arcmin^{-1} and 2.50 arcmin, respectively.

2.1.2. Optical measurement

Besides the X-ray measurement, surface roughness is directly measured by 1-dimensional WYKO profilometer (WYKO TOPO-2D). The microscope is equipped with a 40 magnification objective which leads to a surface-wavelength coverage of 333 μm to 0.65 μm on the mirror surface.

PSDs evaluated from the surface profiles measured by WYKO are in good agreement with those estimated from X-ray scattered tail (Fig. 5). We can conclude that the surface roughness of the Astro-E reflectors is improved from those of ASCA by one order of magnitude. The standard deviations of the surface height ranges from 3Å to 5Å.

2.2. Slope Error

We move on to an angular dispersion of the specular component "core" caused by the surface undulation of the longer surface wavelength than that dealt with in § 2.1, namely a slope error of the surface. Resultant angular distribution is independent of energy of incident X-rays, unlike in the case of the surface roughness. We measure the slope error with the surface wavelength shorter than 3 mm directly with X-rays, while that between 3 mm to 100 mm are evaluated by a laser profilometer.

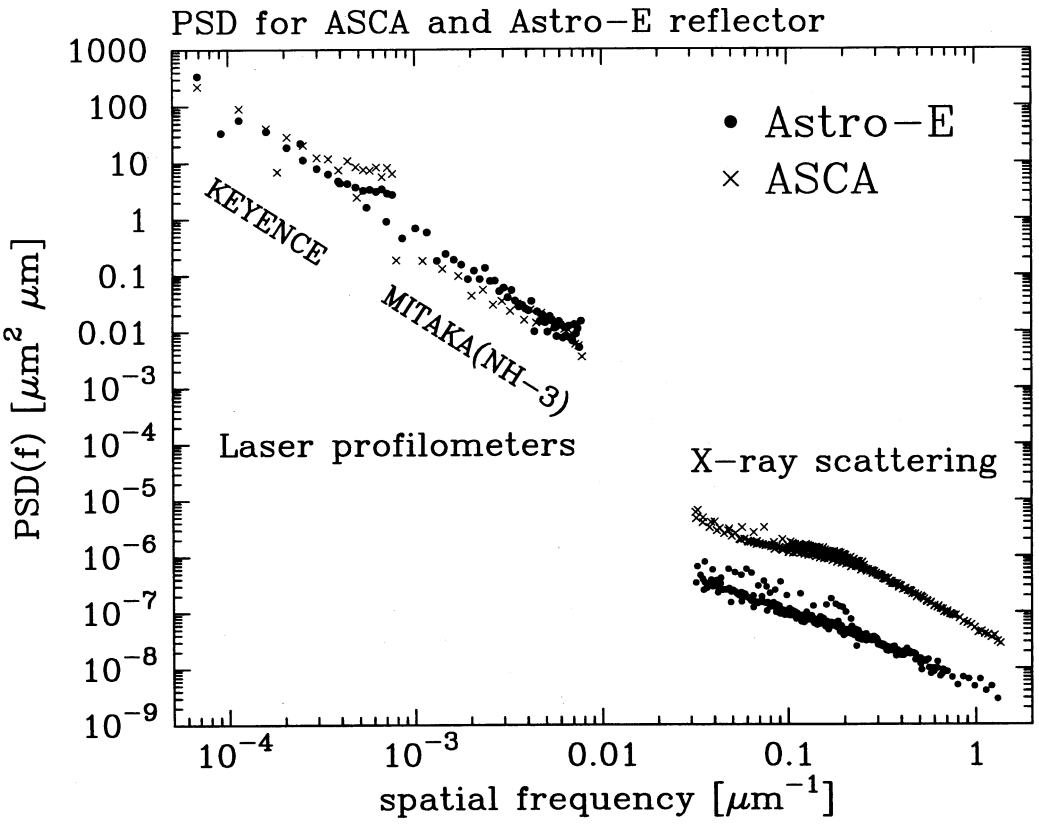

Figure 5. Overall PSD (Power Spectral Density) of Astro-E (filled circles) and ASCA (crosses) reflector surface. The data are evaluated from various measurements as denoted in the figure.

2.2.1. Mid-frequency waviness — broadening of specular component

The sub-mm and mm scale waviness causes the small dispersion of the specular component, resulting in "core" broadening. Our aim is to know the angular distribution of reflected X-rays, in other words, the point spread function (PSF) due to the surface waviness, so we directly examined the reflected profile putting emphasis on the specular component.

The measurements were carried out at Nagoya University under almost the same configuration as noted in § 2.1. In order not to sample local characteristics, we measured the reflected profiles on 3 independent points on a single reflector and add them to obtain the average profile. Removing the effect of the incident beam divergence from the measured profile by deconvolution, we obtained $\mathrm{PSF_{short}}$ shown in Figure 6. We named the PSF with the suffix "short" from the surface wavelengths concerned. The $\mathrm{PSF_{short}}$ is empirically well represented with a Gaussian plus an exponential function. The peak of $\mathrm{PSF_{short}}$ is well fitted by the Gaussian with σ_{gau} of 0.21 arcmin. The small-angle scatter around $|\theta_d| = 1$ arcmin, namely the wing of the core, is well fitted by the exponential function with σ_{exp} of 0.45 arcmin.

2.2.2. Low-frequency waviness — laser profilometer measurement

The larger scale slope error causes the direction of the reflected X-rays to deviate from the specular direction according to the local slope of the surface. The slope errors due to 3 mm to 100 mm (reflector length) scale were evaluated using laser profilometer developed by KEYENCE. This high precision measuring device allows to measure the height deviation with accuracy of 0.1 μm. Sampling pitch of measurements is 0.38 mm in the axial direction. The surface waviness of 29 reflectors of Astro-E (17 for primary and 12 for secondary) are examined along the direction of optical axis. We measured axial profiles at 5 azimuthal positions of each individual reflector, 145 axial profiles in total.

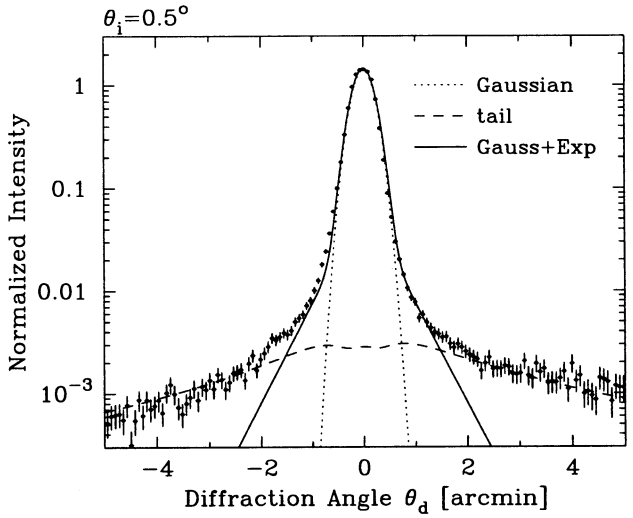

Figure 6. Point spread function due to the mid-frequency (sub-mm to mm) surface waviness ($\mathrm{PSF_{short}}$). The solid curve shows the fitted function; Gaussian plus exponential. Note that the extended tail ($|\theta_d| > 1.5$) is well represented with the scattering and Lorentzian as described in § 2.1. The function for extended tail (scattering plus Lorentzian) is indicated by dashed line.

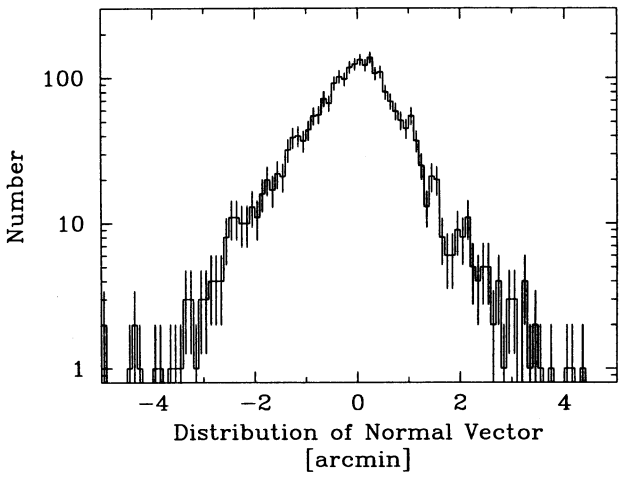

Figure 7. Angular distribution of the reflection due to the surface waviness of long surface wavelengths ($\mathrm{PSF_{long}}$). It was deduced from the distribution of normal vector of reflector surface using laser profilometer. Compared with $\mathrm{PSF_{short}}$ (Fig. 6), $\mathrm{PSF_{long}}$ is widely spread.

The normal vector of the reflector surface is derived at each 3 mm point. Slope errors are smaller than 0.5 arcmin on 70 % of the surface area, and 90% of the normal vectors are settled within ±1 arcmin around the specular direction. Large slope errors are mostly seen at the edge of the reflectors, which is natural because the Astro-E reflectors are so thin that the shape of the reflectors can be easily distorted especially at the edges. Note that the slope error of $\Delta\theta$ of the reflector causes the deviation of $2\Delta\theta$ in the reflection angle. Hence, the measured fluctuation of normal vector of the reflector surface $f(\theta)$ can be converted to the angle distribution of the reflection ($\mathrm{PSF_{long}}$), as $\mathrm{PSF_{long}}(\theta_d) = f\left(\frac{\theta_d}{2}\right)$ where $\mathrm{PSF_{long}}$ means point spread function due to the large-scale slope error. In Fig. 7, derived $\mathrm{PSF_{long}}$ is shown.

We derived the average PSD of the axial profiles, which is shown in the upper left side of Fig. 5 ("KEYENCE"). It is obvious that PSD of the Astro-E reflector rises rapidly at the mid-frequency around 0.01 $\mu\mathrm{m}^{-1}$, whereas PSD of the Chandra reflector seems to be expressed by simple power-law.[8] Though the level of PSD of Astro-E is comparable to XMM and Chandra in the high-frequency region as described above, that is far exceed by more than four orders of magnitude in the low-frequency region compared with Chandra. Note that the substrate for Astro-E reflectors is so thin that it is not so easy to keep the reflector surface as desired.

2.3. Formulation of the Angular Distribution of Reflected X-rays

The surface imperfectness in various scales of the Astro-E reflector have been examined as described above in the order of the increasing surface wavelength. We compile these results to formulate the angular distribution of reflected X-rays, which is the response function of the single Astro-E reflector. The angular distribution of reflected X-rays can be divided into two parts as follows,

$$\begin{aligned}\frac{dI}{d\theta} &= \left(\frac{dI}{d\theta}\right)_{specular} + \left(\frac{dI}{d\theta}\right)_{scatter} \\ &= \mathrm{PSF_{spec}} \times R_0(\theta_i) \exp\left[-\left(\frac{4\pi\sigma_{\mathrm{DW}}\sin\theta_i}{\lambda}\right)^2\right] \times \frac{R\left(\frac{\theta_i+\theta_s}{2}\right)}{R(\theta_i)} + \left(\frac{dI}{d\theta}\right)_{scatter} \end{aligned} \quad (3)$$

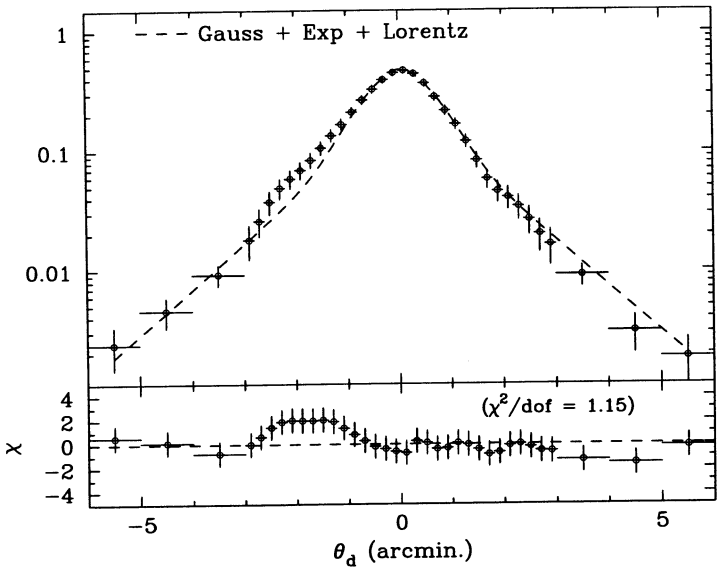

Figure 8. Point spread function (PSF) of specular component for the Astro-E reflector. Fitted function is indicated by dashed line. Residuals from the fitted function are indicated in the lower panel.

where R_0 is the Fresnel reflectivity on the surface, the exponential factor is called Debye-Waller factor, which is used to calculate the reflectivity of smooth surface with roughness $\sigma_{\rm DW}$.

As for the specular component, the angular distribution of reflected X-rays from the whole reflector ($\rm PSF_{spec}$) can be represented by the convolution of PSFs as follows, $\rm PSF_{spec} = PSF_{long} * PSF_{short}$, where $*$ means convolution. Figure 8 shows the $\rm PSF_{spec}$ which is the convolution of $\rm PSF_{short}$ (Fig. 6) and $\rm PSF_{long}$ (Fig. 7). The $\rm PSF_{spec}$ is well represented empirically with a Gaussian and an exponential function, similarly to $\rm PSF_{short}$. In fitting in Fig. 8, we obtained that the width of Gaussian σ_{gau} and $\sigma_{\rm exp}$ to be 0.65 and 1.11 arcmin, respectively, which are about three times larger than those for $\rm PSF_{short}$. This indicates the main cause of the dispersion of the specular component is not the sub-mm scale waviness but the longer scale slope error. Lorentzian function is also needed to express the wider wing of the specular component extending to a large diffraction angle. Hence, we regard $\rm PSF_{spec}$ = Gaussian + Exponential + Lorentzian.

On the scattered component, a formula is already described in Equation 1. $PSD(f)$ is well represented by a power-law with a cut-off, as described in § 2.1. More details are mentioned in Misaki et al..[10]

3. MEASUREMENTS OF A PAIR OF REFLECTORS

Since the response function of a single reflector is described in the previous section, we move on to investigation of the performance of a single pair of the primary and secondary reflectors installed in the housing of telescope.

3.1. Image Quality of Individual Pairs of Reflectors

In order to investigate the causes of the degradation of image quality, we measured a profile of the X-ray beam reflected by each pair of reflectors. The measurements were performed at ISAS X-ray beam facility.[11] The X-ray beam width in azimuthal direction was set to be 2 mm, and that in radial direction was adjusted for each reflector with movable slits so that the X-ray beam fully illuminate only one reflector. Using CCD, we obtained the focal-plane image from the pair of reflectors. The measurements were performed at 4.51 keV.

3.1.1. Distortion of images

The measurements were carried out for all 170 pairs of reflectors at 5 sectors. We thus obtained more than 800 profiles in total. Examples of the results are shown in Fig. 9. It is clearly seen that the profiles reflected by each pair of reflectors extend up to several arc minutes in radial direction. Besides extending, the reflected

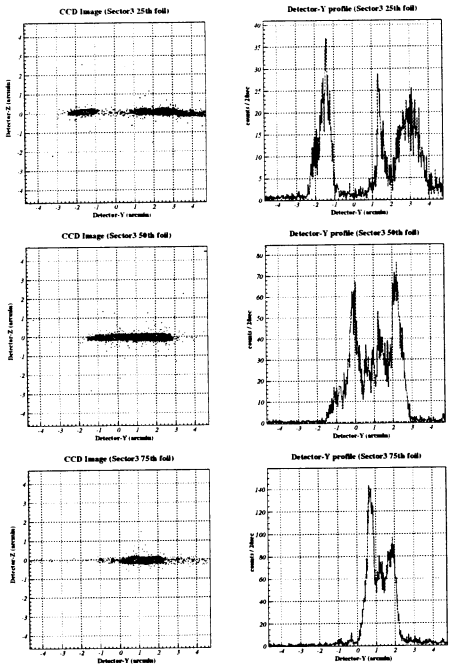

Figure 9. Examples of profiles reflected by a pair of reflectors. Left; focal-plane images, Right; their projections.

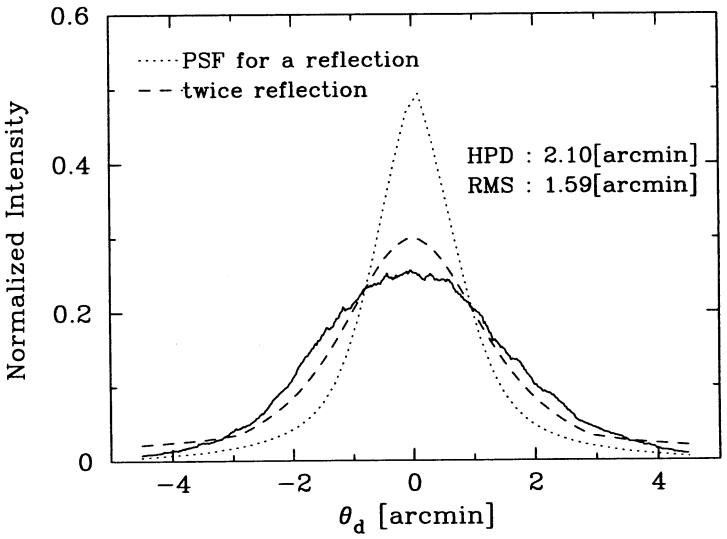

Figure 10. Averaged profile reflected by a pair of reflectors (thick line). Dotted line; the PSF reflected on the single Astro-E reflector (Fig. 8), dashed line; convolution of the PSF by itself for the twice reflection. As marked in the figure, the HPD and the root mean square (RMS) of the averaged profile are 2.10 and 1.59 arcmin, respectively.

profiles indicate very irregular distribution, such as, double peaks, one-sided profile, and so on. Note that these examples are not special, but more-or-less common for other reflectors. These results suggest that the slope error in longer than the mm-scale of the reflector surface brings divergence of the reflected beam directions and leads to the unexpectedly distorted profiles.

To evaluate the profile reflected by each pair of reflectors quantitatively, we added up all the profiles. Resultant averaged profile is shown in Fig. 10. It is well represented by a Gaussian with σ of 1.6 arcmin. HPD of the averaged profile is 2.10 arcmin which is equivalent to that of the whole XRT. Therefore, the degradation of image quality of the Astro-E XRT almost comes from the distorted profiles of pairs of reflectors.

To investigate the causes of the distortion of the profile, we have compared the averaged profile with the PSF of the single reflector (§ 2, Fig. 8) which is shown in Fig. 10 by a dotted line. Since the photons in the averaged profile undergo double reflections, we convoluted the PSF by itself, also shown in the figure by a dashed line. It is clearly seen in Fig. 10 that the averaged profile is somewhat blurred more than the convolution of the PSF. The remaining possible cause to introduce the image blur is a positioning error of the reflectors.

3.1.2. Distribution of foci

The distribution of foci on the focal plane among the pairs is also examined. Though the individual images are very distorted as is shown in Fig. 9, we regarded the centroid of flux as the focus of each pair. The distribution of the foci indicates the deviation of the average slope over the reflector, which arises from both the positioning error of reflector edges and the long-scale slope error of the reflectors.

The foci from all of individual pairs are very concentrated in azimuthal direction. On the other hand, the broad distribution of the foci is found in the radial direction. The radial standard deviation is $\sigma = 1.0$ arcmin, which is significant comparing to the HPD of ~ 2.1 arcmin obtained from XRT.[5] The divergence of the foci due to the positioning error and the slope error of the reflector has a significant effect for degrading the imaging capability of the XRT.

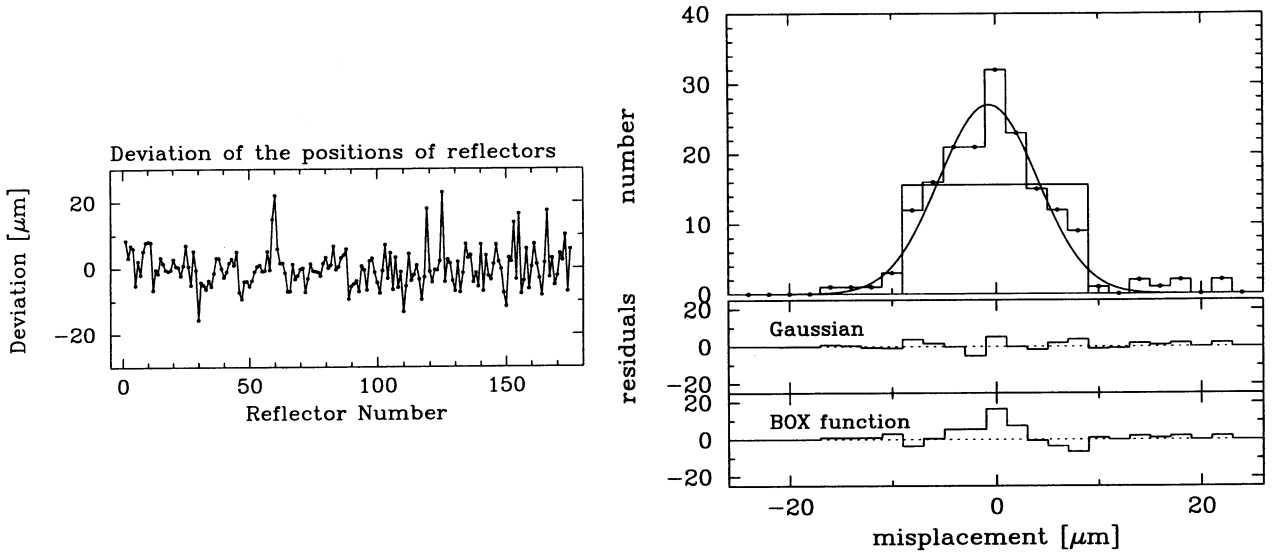

Figure 11. Positioning error of the reflectors. Left; deviation of the position of reflectors versus the number of the reflector. Right; distribution of the deviations. The fitted functions, Gaussian and box function, are also indicated in the panel. The residuals (data − model) for the Gaussian and box function are shown separately in the lower two panels.

3.2. Positioning Error of Reflectors

To evaluate the amount of the positioning errors of reflectors, we directly measured the positions of reflectors in the housing. The measurement system is equipped with an optical microscope and a mechanical stage controlled by servomechanism, which allows to measure the position of reflectors with an accuracy of 0.1μm.

The reflector positions were measured at the bottom of the quadrant of XRT-I for all the reflectors in sector 8. The measured positions deviate from the designed value as shown in the left panel of Fig. 11. The root mean square of the deviation is 5.9 μm and the peak-to-valley value is 38.6 μm. The 158 reflectors out of 175 are settled within $\pm 8\mu$m from the designed position, which is consistent with the expected margin according to the design (Fig. 2).

As indicated in the right panel of Fig. 11, we have attempted to represent the distribution of the positioning error with a Gaussian or a box function. The results of the fittings suggest that a Gaussian is preferable rather than a box function, which is clearly seen in the residuals. The obtained best-fit value of Gaussian σ is $4.8^{+1.2}_{-0.7}\mu$m.

4. PERFORMANCE EVALUATION USING RAY-TRACING SIMULATOR

We have developed the ray-tracing simulator based on the results described above. The validity of the representative numerical model is examined with the extensive ground-based calibrations.[5]

4.1. Image Quality

The slope error and the positioning error of the reflector are possible causes to degrade the image quality. In order to examine how the positioning error deteriorates the image quality, we have carried out the simulation with various levels of positioning errors. Figure 12 shows the HPD obtained by the simulation. It reveals that the PSF on individual reflector due to the slope error degrades image quality to 1.8 arcmin. Then, taking account of the positioning error of 5μm which is measured value as is stated above, the simulated HPD is well consistent with the ground-based calibration results.[5]

In summary, the degradation of image quality from design value (0.23 arcmin) to measured one ($\sim$ 2 arcmin) is attributed to the two causes; (1) PSF on individual reflectors due to slope error of the reflector : 0.23 $\rightarrow$ 1.8 arcmin, (2) the positioning error $\sigma \sim 5\mu$m : 1.8 $\rightarrow$ 2 arcmin. The slope error of the reflector is the major factor in the degradation of image quality.

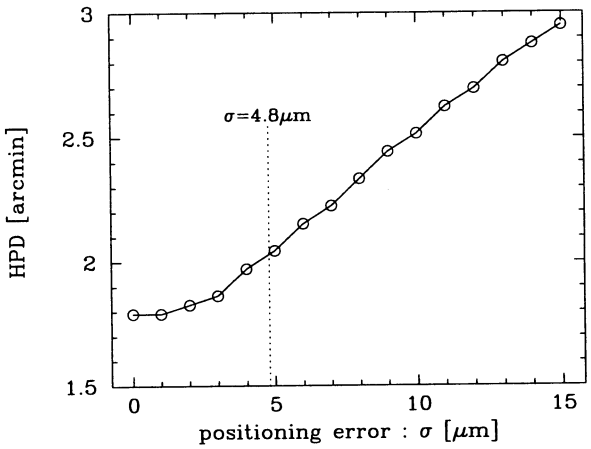

Figure 12. Simulated image quality depending on the positioning error. The measured positioning error (σ = 4.8μm) is indicated by vertical dotted line. The measured HPD($\sim$ 2 arcmin) is well consistent with the simulation at the point.

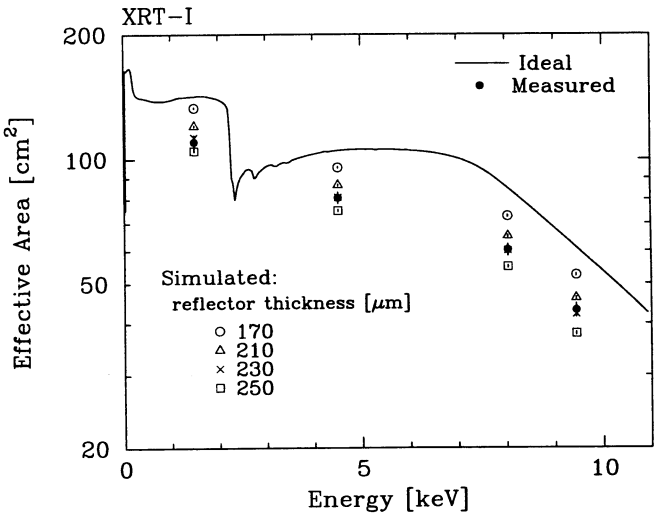

Figure 13. On-axis effective area of the quadrants. The ideal design curve and the measured values (Table 1) are indicated by solid line and filled circles, respectively. The other marks are simulated results with various reflector thickness as denoted in the figure. The simulated results with reflector thickness of 230μm (cross) well agree with the measured value (filled circle), so both the crosses and filled circles overlap each other at each energy.

4.2. Effective Area

In addition to all the parameters investigated in the previous sections, the shadowing effect is considerable to reduce the effective area. The shadowing should be caused by various factors, e.g, an insufficient shape of reflector edge, imperfect alignment between primary and secondary housings, and so on. The parameter "reflector thickness" can be regarded as the indicator of the shadowing effect, practically. Introducing this parameter, the measured effective area can be well represented by the simulation with the reflector thickness of 230μm, as is seen in Fig. 13. The simulation and the results of the ground-based calibrations are consistent within an accuracy of 3% at every energies. Note that this value of 230μm is not real thickness of the reflectors, but simple indicator of the shadowing effect. Considering the amount of the shift between the primary and secondary housings and the deformation of reflectors at the edge, it is possible that the surplus of reflector thickness is estimated to be 60μm.

We can attribute more than 20% loss of effective area to the causes; (1) PSF on individual reflectors due to slope error of the reflectors, (2) the positioning error of the reflector of $\sigma \sim 5\mu$m, (3) reduction of reflectivity because of surface roughness of the reflectors of σ_{DW} = 3.5Å, (4) the shadowing effect of the reflector thickness of +60μm. We estimated the contributions of these causes in deficit of effective area using the ray-tracing simulator. At Ti-Kα (4.51 keV), the fractional loss by each factor is estimated to be (1)5%, (2)2%, (3)3%, (4)15%. The shadowing effect is the major factor in the deficit of effective area. As for the energy dependence in the reduction factor, a steep energy dependence is found in the loss due to surface roughness. The deficit due to the surface roughness of 3.5Å is less than 1% at Al-Kα, while the loss is more than 7% at the higher energies (Cu-Kα, Pt-Lα). This steep energy dependence is the main reason to produce the energy dependence in the reduction factor of the effective area. The other factor also shows the energy dependence, although the dependences are small compared with that due to surface roughness. The spacing between the reflectors becomes smaller for the inner reflectors, therefore the fractional loss due to the reflector thickness and the positioning error is larger for the inner reflectors. At the Cu-Kα and Pt-Lα, only the inner reflectors are effective for collecting X-rays because of smaller critical angles. Hence the reduction of the effective area is larger at the higher energies. For example, the reduction factor due to the shadowing effect (4) is 15%, 15%, 17%, and 19%

at 1.49, 4.51, 8.04, and 9.44 keV, respectively.

5. SUMMARY AND CONCLUSION

To clarify the causes of the performance degradation of Astro-E XRTs, we evaluated the possible causes quantitatively with X-rays and optical microscopic measurements. We have developed the ray-tracing simulator based on those measurements. Taking account of the shadowing effect in addition to the measured parameters, on-axis effective area and HPD are well reproduced by the ray-tracing simulator.

It is revealed that the slope error of the individual reflectors is the dominant factor of the degradation of image quality. The deficit of effective area is mainly attributed to the shadowing effect. The loss of $15 \sim 20\%$ can be explained by the shadowing effect indicated by the reflector thickness of $+60\mu$m. The effect of the surface roughness of $\sigma_{\rm DW}$ of 3.5Å produces the energy dependence in the reduction factor of the XRT effective area. In order to build the ray-tracing simulator which constructs the XRT response function, we further need to perform a fine tuning so as to represent the vignetting function, and so on.

Through the series of measurements, we could understand and distinguish quantitatively the causes of the performance degradation of Astro-E XRTs. The results gives us the crucial keys and a proper guideline for the improvement of the performance of XRT.

More detail statements and discussions are found in the series of the Astro-E XRT papers (Ref. 4,5,10).

ACKNOWLEDGMENTS

We would like to express our gratitude to all the Astro-E XRT team members at NASA/GSFC for the extensive developments and production of XRT. We are also grateful to the members at Nagoya university for their continuous collaboration. We all hope that the Astro-E2 will be successfully launched in February 2005 and give us new exciting discoveries.

REFERENCES

1. Y. Tanaka, H. Inoue, and S. S. Holt, "The X-ray astronomy satellite ASCA," *Publ. Astron. Soc. Jpn.* **46**, pp. L37–L41, 1994.
2. P. J. Serlemitsos et al., "The X-ray telescope on board ASCA," *Publ. Astron. Soc. Jpn.* **47**, pp. 105–114, 1995.
3. Y. Tsusaka et al., "Characterization of the Advanced Satellite for Cosmology and Astrophysics X-ray telescope: preflight calibration and ray tracing," *Applied Optics* **34**, pp. 4848–4856, 1995.
4. H. Kunieda et al., "X-ray telescope onboard Astro-E: optical design and fabrication of thin foil mirrors," *Applied Optics* **40**, pp. 553–564, 2001.
5. R. Shibata et al., "X-ray telescope onboard Astro-E. II. Ground-based x-ray characterization," *Applied Optics* **40**, pp. 3762–3783, 2001.
6. H. Kunieda et al., "Roughness measurements of x-ray mirror surfaces," *Jpn. J. Appl. Phys.* **25**, pp. 1292–1299, 1986.
7. P. Z. Takacs and E. L. Church, "Figure and finish of grazing incidence mirrors," *Nucl. Inst. Methods in Phys. Res.* **A291**, pp. 253–264, 1990.
8. D. E. Zissa, "AXAF-I High Resolution Mirror Assembly image model and comparison with x-ray ground-test image," *Proc. SPIE* **3766**, pp. 36–50, 1999.
9. Ph. Gondoin, B. Aschenbach, M. Beijersbergen, R. Egger, F. Jansen, Y. Stockman, and J. P. Tock, "Calibration of the first XMM flight mirror module I - Image quality," *Proc. SPIE* **3444**, pp. 278–289, 1998.
10. K. Misaki et al., "X-ray telescope onboard Astro-E. III. Guidelines to performance improvements and optimization of ray-tracing program," in preparation.
11. H. Kunieda et al., "Thirty-meter X-Ray pencil beam line at the Institute of Space and Astronautical Science," *Jpn. J. Appl. Phys.* **32**, pp. 4805–4813, 1993.

ASTRO-E2 XRT Pre-Collimator for Stray Light Protection I. — Design and Expected Performance

R. Shibata[a], H. Mori[b], Y. Maeda[b], K. Misaki[b], Y. Haba[b], K. Itoh[b], R. Iizuka[b], T. Morihisa[b], H. Kunieda[b], A. Hayakawa[c], and M. Ishida[c]

[a] Department of Physics, Nagoya University, Furo-cho, Chikusa-ku, Nagoya 464-8602, Japan

[b] Institute of Space and Astronautical Science, 3-1-1 Yoshinodai, Sagamihara, Kanagawa 229-8510, Japan

[c] Department of Physics, Tokyo Metropolitan University, 1-1 Minami-Osawa, Hachioji, Tokyo 192-0397, Japan

ABSTRACT

Next Japanese ASTRO-E2 satellite carries five X-ray telescopes (XRTs), and the pre-collimators for the stray light protection will be installed on them. The pre-collimator is composed of the vertical foil cylinders which line up at the top of the primary reflectors of the XRT. This configuration is effective to reject the stray light of the "secondary only" reflection, which is the most of the stray light from large off-axis angles up to 70′ to the focal plane detector within 18′ × 18′. If the height of the pre-collimator is 30 mm (15% of the total height of XRT), we can protect all the "secondary only" component at > 30′ off-axis. The field of view will become only about 10% less due to the collimation effect of the 30 mm high pre-collimator. However, new stray light component is generated by the reflection and scattering by the pre-collimator itself, especially at small off-axis angles. As a result, we estimate the total flux of the stray light to be about 10% at 30′ off-axis and 5% at 60′ off-axis, compared with the case without pre-collimators.

Keywords: ASTRO-E2, X-ray telescope, stray light, collimator, vignetting

1. INTRODUCTION

ASTRO-E2, the next Japanese X-ray astronomy satellite to be launched in February 2005, will carry five X-Ray Telescopes (XRTs)[1]. They adopt the conical approximation of Wolter Type-I optics with nested thin foil reflectors, and have high throughput up to 10 keV, as in the cases of ASCA and ASTRO-E. In the focal plane, four X-ray Imaging Spectrometers (XIS) which adopt X-ray CCD cameras[2], and one X-Ray Spectrometer (XRS) which is the micro-calorimeter[3], are placed as detectors. In addition, ASTRO-E2 also has a Hard X-ray Detector (HXD) designed to observe high energy X-rays (10−600 keV), which utilize well-type phoswich scintillators with embedded silicon-pin detectors.

The nesting structure of XRT, however, causes flux contamination in the focal plane detectors due to stray light, which comes from the outside of field of view (FOV). The stray light makes it difficult to perform the mapping observations of spatially extended sources, i.e., clusters of galaxies and cosmic X-ray background, as well as considerable bright point-like sources outside of FOV. To cope with these, we adopt the pre-collimator for the stray light protection.

In this paper, we report the current design and expected performance of the ASTRO-E2 XRT pre-collimator based on the ray-tracing simulation. In §2, we describe the XRT design and characteristic of the stray light. In §3, we explain the pre-collimator including the design concept. Expected performance of ASTRO-E2 XRT pre-collimator is reported in §4. Summary and conclusions are given in §5.

Further author information: (Send correspondence to R. Shibata)
R. Shibata: E-mail: shibata@u.phys.nagoya-u.ac.jp

2. ASTRO-E2 XRT AND STRAY LIGHT

2.1. Structure of ASTRO-E2 XRT

Similarly with several X-ray astronomy satellites so far in orbit, the ASTRO-E2 XRT also adopts the Wolter type-I optics in principle. To cope with lack of the geometrical area due to the grazing incidence optics, we nests a large number of reflectors radially. Then we obtain large effective area up to 10 keV. The thin substrate, however, prevents us from realizing paraboloids and hyperboloids for the reflectors. We thus substitute conical surfaces for both.

In table 1, we summarize parameters of the XRTs on board ASTRO-E2. For ASTRO-E2, we have two kinds of telescopes with different focal lengths. One is for the XIS with $f = 4.75$ m (4 modules, named as XRT–I), and the other is for the XRS with $f = 4.50$ m (1 module, XRT–S). In ASTRO-E2, as well as in ASCA, each XRT is composed of the equivalent four "quadrants". Each quadrant comprises a primary and a secondary housing which contain the reflectors for the primary and the secondary reflection. The numbers of reflectors per housing are 175 and 168, for the XRT–I and the XRT–S, respectively. The reflectors of each housing are supported by thirteen alignment bars, which are evenly spaced in azimuth, from both the top and the bottom sides. Each alignment bar has grooves to catch the reflectors, determining the positions of the reflectors as well as sustaining their shape.

For ASTRO-E2 XRT, some kinds of improvements are made since ASCA and ASTRO-E. Compared with ASCA, one is the improvement for the reflector production method, thus a replication technique. Because the replication method can print the surface of the finely polished mandrel on the reflecting surface, reducing both the surface roughness of a few to a hundred μm scale and the surface undulation with a scale down to mm which are inherent to the substrate, the X-ray image quality is greatly improved. And the other is the scale up effect. Owing to a larger diameter and a longer focal length of the XRT, the effective area becomes significantly larger than that of ASCA by a factor of 1.5 and 2.5 at the X-ray energy of 1.5 keV and 8.0 keV, respectively[4]. As improvement from ASTRO-E, a new groove shape of the alignment bar and a supporting method of the reflectors in housings are adopted, and image quality will be further improved to be $\sim 1.2'$.

Table 1. Parameters of X-ray telescopes on board ASTRO-E2

	XRT–I (for XIS)	XRT–S (for XRS)
Number of Telescope	4	1
Focal Length	4750 mm	4500 mm
Plate Scale	0.72 '/mm	0.76 '/mm
Number of Nestings	175	168
Primary Incident Angle	0.178° – 0.599°	0.188° – 0.634°
Telescope Weight	18.0 kg	18.0 kg
Reflector Substrate		
Material	Aluminum	Aluminum
Thickness	150 μm	150 μm
Length	101.6 mm	101.6 mm
Reflecting Surface		
Material	Au	Pt
Thickness	> 1000 Å	> 1000 Å
Geometric Area	873 cm^2	887 cm^2
Effective Area† @ 1.5 / 8.0 keV	450 / 250 cm^2	460 / 260 cm^2
Spatial Resolution† (HPD††)	2.0 '	2.0 '
Field of View† @ 1.5 / 8.0 keV	19 ' / 14 '	20 ' / 15 '

† : Results of pre-flight calibration for ASTRO-E2 XRTs [4]

†† : Half Power Diameter

2.2. Classification of Stray Light

Because of the thin reflector-nesting configuration of the XRT, it is possible that X-rays intrude from outside the FOV. In figure 1, we have shown patterns of the stray lights. They are classified as (a) primary reflection, (b) secondary only reflection, (c) multiple (backside) reflection, and (d) no reflection. Among them the backside reflection is expected to have a strong energy dependence, because it includes reflection at the backside of the reflector which is a bare aluminum. The backside reflection is thus expected to be more intense for lower X-ray energies.

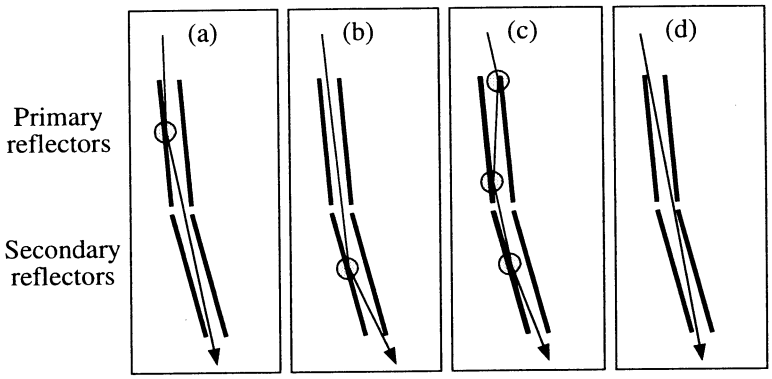

Figure 1. Four examples of stray light paths: (a) reflection only by primary reflectors, (b) reflection only by secondary reflectors, (c) multiple reflections (or backside reflection) by front and back surface of reflectors, (d) direct path (no reflection). Gray circles show reflecting points on the reflectors.

Figure 2 illustrates the coordinate system of the ray-tracing simulation, and figure 3 shows examples of simulated stray light images on the focal plane of ASTRO-E2 XRT–I without the pre-collimator. Monochromatic parallel X-ray beam of 1.49 keV and off-axis angle of 30′ are assumed. The FOV of XIS as the focal plane detector is shown as central square with 24.6 mm × 24.6 mm size.

From the stray light images per each component shown in figure 3, it is clear that the image shapes of them indicate distinctive features one another. At 30′ off-axis, we can recognize that the three components classified as the primary only, secondary only, and backside reflections, reach in the XIS FOV. The secondary only component, which is dominant up to ∼ 70′ off-axis, has strongest flux contribution among them, and fills half of the XIS FOV. The primary only component distributes on the edge of XIS. However, the its intensity is smaller by about two order than that of secondary only, and appears only at small off-axis angles of < 30′.

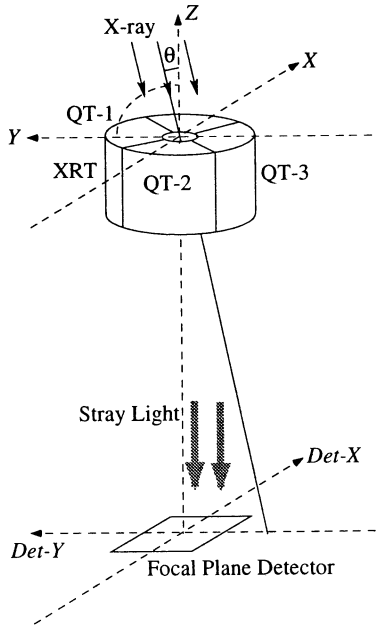

Figure 2. Coordinate system of the ray-tracing simulation for studying the XRT and pre-collimator response. We define the off-axis angle θ along the $Y - Z$ plane throughout this paper.

The backside component is also faint, but spreads over widely. As expected, this component decreases with increasing X-ray energy because of the reflection on the bare aluminum surface. In fact, the intensity of the backside reflection is smaller by at least a factor of several than that of ASCA. The direct component has no flux contamination at any off-axis angles in the case of this imaging size of XIS.

Figure 4 indicates the same stray light image as figure 3, but showing per each quadrant. The configuration of quadrants are shown in figure 2. We can recognize that the secondary only and backside components which look through the QT–1 and the primary only component from the opposite QT–3 reach in XIS FOV. Note that the other two quadrants (QT–2 and 4) are not concerned with the flux contamination within XIS FOV.

As noticed from figure 3 and 4, the on-axis position (at which the detector locates in orbit) is contaminated by the three components of the stray light, thus primary only, secondary only, and backside reflections. Then, the rejection of the secondary only, which has most of the stray light flux, is most effective for resolving the stray light problem.

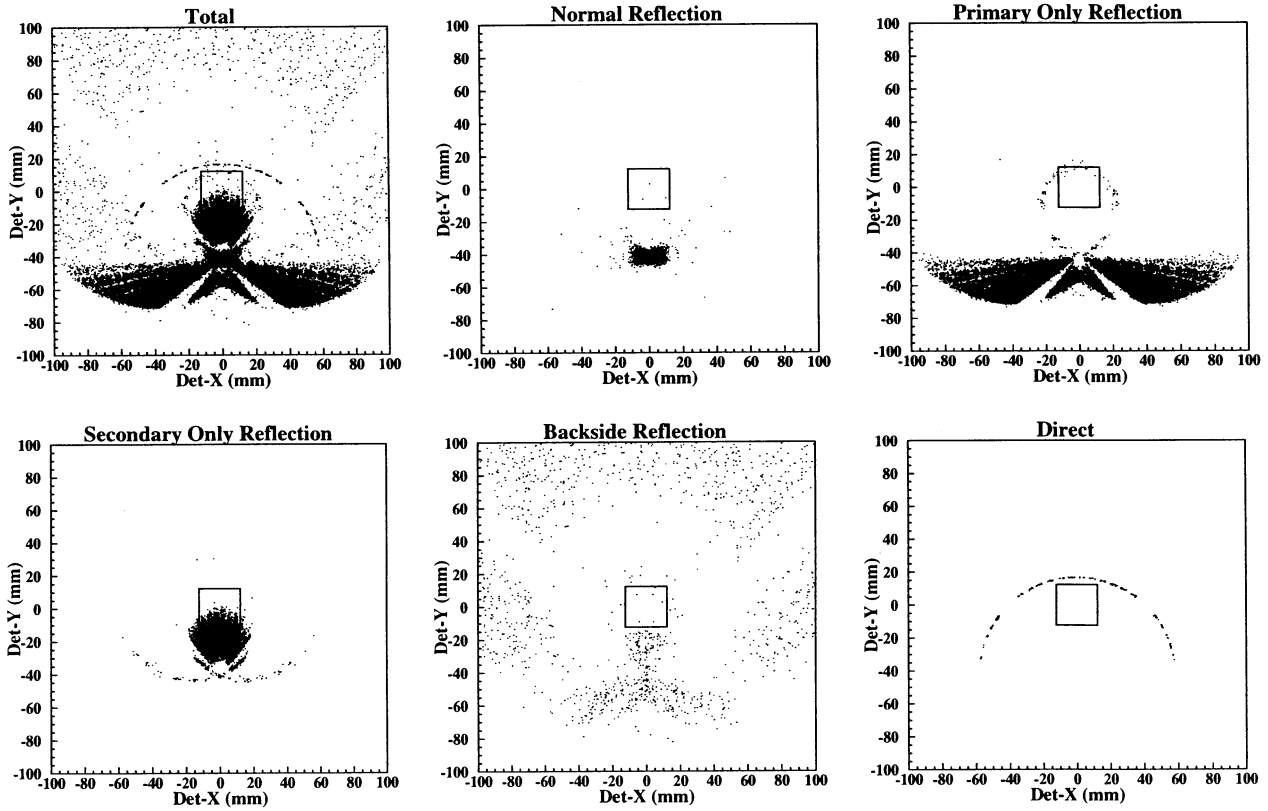

Figure 3. Simulated stray light images on the focal plane of ASTRO-E2 full telescope (4 quadrants, XRT-I) without the pre-collimator. Monochromatic parallel X-ray beam of 1.49 keV and off-axis angle of 30′ are assumed. Image size is 100 mm × 100 mm, and the field of view of XIS as the focal plane detector is shown as central square with 24.6 mm × 24.6 mm size. (*top-left*): Total image combined with all normal and stray light components. (*top-middle*): Normal reflection component. (*top-right*): Primary only reflection component. (*bottom-left*): Secondary only reflection component. (*bottom-middle*): Multiple (backside) reflection component. (*bottom-right*): No reflection (direct) component.

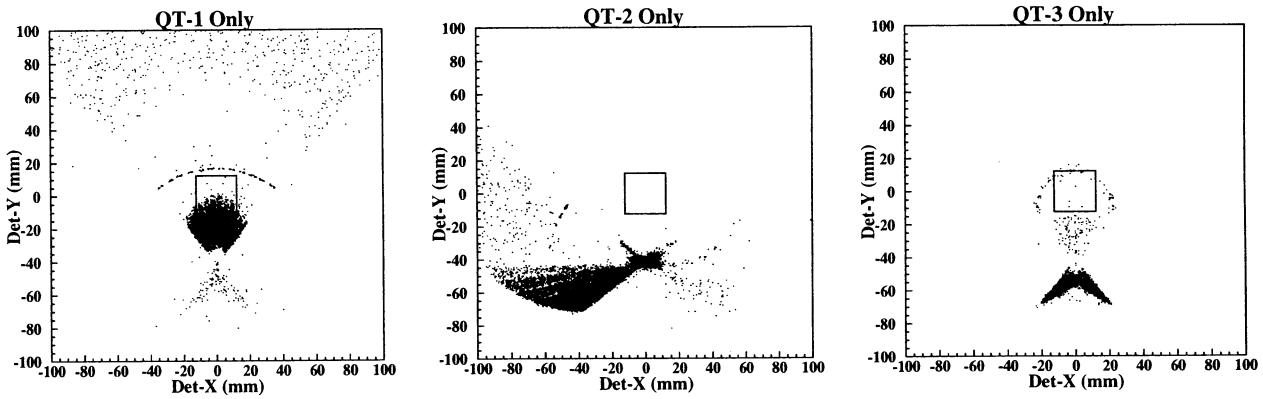

Figure 4. Simulated stray light images on the focal plane of ASTRO-E2 XRT. Same as figure 3, but showing the images per quadrant. Quadrant configuration are shown in figure 2. (*left*): Quadrant-1 only image. (*middle*): Quadrant-2 only image. Quadrant-4 image is axisymmetric along the function of *Det-X* = 0 . (*right*): Quadrant-3 only image.

3. PRE-COLLIMATOR FOR STRAY LIGHT PROTECTION

3.1. Design Concept

At large off-axis angles, the stray light components which come in XIS FOV are primary only, secondary only, and backside reflection, already mentioned in section 2.2. Among them, it is effective to protect the secondary only component, which has most of the stray light flux. Since this component mainly passes near the top of the primary reflector of XRT, it is desirable that we make vertical foil cylinders line up at the top of the primary reflectors. If these foils are thinner than the reflectors, we can keep the effective area at on-axis and utilize the collimation effect of them at any off-axis angles.

Figure 5 shows a design concept of XRT pre-collimator. In order to reject the secondary only component, we make thin vertical blades arrange at the top of the primary reflectors. Because of the thin reflectors ($\sim 170\mu$m), it is difficult to reduce the area of the blade surface using circular rings which the XMM-newton satellite adopts[8]. The height needed for these blades to be effective depends on radius. Such a pre-collimator has a merit for the effective protection of the secondary component even if the XRT adopts the thin-reflector nesting structure. On the other hand, it makes weak points about the decrease of XRT FOV due to shadowing effect and possibility of new stray light reflected by itself. The above properties for ASTRO-E2 XRT pre-collimator are evaluated in section 4.

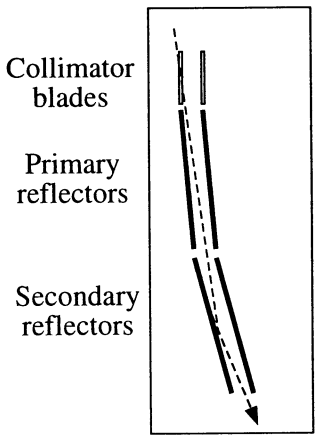

Figure 5. Design concept of ASTRO-E2 XRT pre-collimator. In order to reject the secondary only component effectively, we make vertical foil cylinders line up at the top of the primary reflectors.

Here we consider the needed height of the blades for the pre-collimator in the case of XRT-I. Left panel of figure 6 shows the classification of reflection paths as functions of an incident X-ray position r (telescope radius) on XRT and X-ray incident angle θ. If we define the grazing angle of the primary reflector from the optical axis to be τ, the secondary only reflection causes the ghost image under the condition of $\theta/2 < \tau < \theta$. Then the telescope radius of the primary reflector with $\tau = \theta/2$ corresponds the minimum radius caused the secondary only reflection, and the position required the minimum height (= 0) of the blade. It satisfies the relation of

$$r_{\rm min} = 1.67 \times 10^2 \ \ \theta + 2.97 \times 10^{-2} \quad [\rm mm]$$

, where θ is in degree. On the other hand, the maximum radius caused the secondary only reflection in XIS FOV is not limited by the condition of $\tau = \theta$, but the half size of the focal plane detector with 12.3 mm. Since the path of the single reflection on the secondary reflectors is satisfied with the relation of $r \propto 2\ Det\text{-}r$, $r_{\rm max}$ is described to be

$$r_{\rm max} = r_{\rm min} + 24.6 \quad [\rm mm] \ .$$

For example, at 30′ off-axis angle the radius range on XRT, which caused the secondary only reflection in XIS FOV, corresponds to be 83.5 – 108.1 mm.

Next we calculate the maximum height at the $r_{\rm max}$. The height is decided by the positions of the primary-top radius at the $r_{\rm max}$ and the primary-bottom radius of neighboring inner reflector, and is obtained to be

$$h_{\rm max} = \frac{r^{\rm pt}_{\rm max} - r^{\rm pb}_{\rm max-1} - t}{\tan\theta} - \ell \quad [\rm mm]$$

, where ℓ and t are the length and thickness of the reflector. Therefore the maximum heights of the pre-collimator for 30′ and 60′ off-axis angles are calculated to be 30.8 mm and 15.7 mm, respectively. Right panel of figure 6 shows the needed height of the pre-collimator blade as a function of the XRT radius for all off-axis angles. Shaded portion also shows that for arbitrary single off-axis angle. In the ideal case, we need the height of 76 mm at the innermost radius.

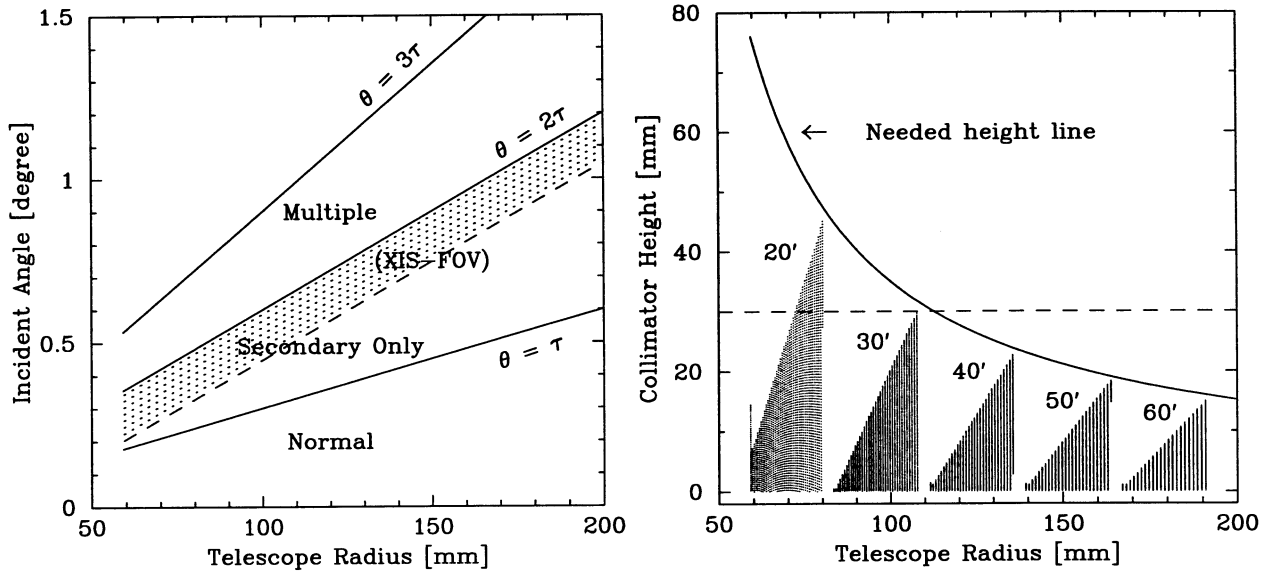

Figure 6. (*left*): Classification of reflection paths as functions of an incident X-ray position on XRT and incident angle ($\tau > 0$). τ indicates the grazing angle of the primary reflector from the optical axis. Shaded portion shows that the secondary only reflection is reached in XIS FOV. (*right*): Needed (ideal) blade height as a function of the XRT radius for all off-axis angles. Shaded portion shows that for arbitrary single off-axis angle.

3.2. ASTRO-E2 XRT Pre-Collimator

For ASTRO-E2 XRT pre-collimator, we adopt the constant height of 30 mm, which the secondary only reflection with the off-axis angle $\theta > 30'$ can be protected, because of limiting the space on the optical bench in the satellite. The pre-collimator is scheduled to be installed on all five XRTs.

Figure 7 shows a picture and drawing of the ASTRO-E2 XRT pre-collimator (EM) of one quadrant. Table 2 also summarizes parameters of the ASTRO-E2 XRT pre-collimator. For the blade material, the aluminum with mil-finish surface which is characterized by low reflectivity with X-ray is utilized. The blade is 50 μm thinner than reflector in order to cancel the misalignment of the pre-collimator. To reduce the roundness error of the blade, the heat forming process is performed similarly with the reflector production. The blades in the housing are supported by 13 alignment plates, which are evenly spaced in azimuth, from both the top and the bottom sides. Each alignment plate has grooves to catch the blades, determining the positions of the blades as well as sustaining their shape. We need to keep the distance between the primary reflector and blade as short as possible in order to prevent the stray light which passes through directly. For the limitation of the XRT housing structure, we allow the space of 8 mm, which means the sufficient protection of the secondary only reflections with off-axis angles of $\theta < 62'$. The housing size is the same as the XRT one, except for the height. The total weight is 2.6 kg per quadrant and 35% of the weight is occupied by the blades.

For ASTRO-E2, the quadrant of the telescope comprises the pre-collimator, primary, and secondary housings. The four quadrants are connected by inner and outer rings from the top and the bottom sides, and are made into one full telescope. The thermal shield is installed on top of the pre-collimator. The alignment procedure among them is mentioned in Mori et al. (2002)[7].

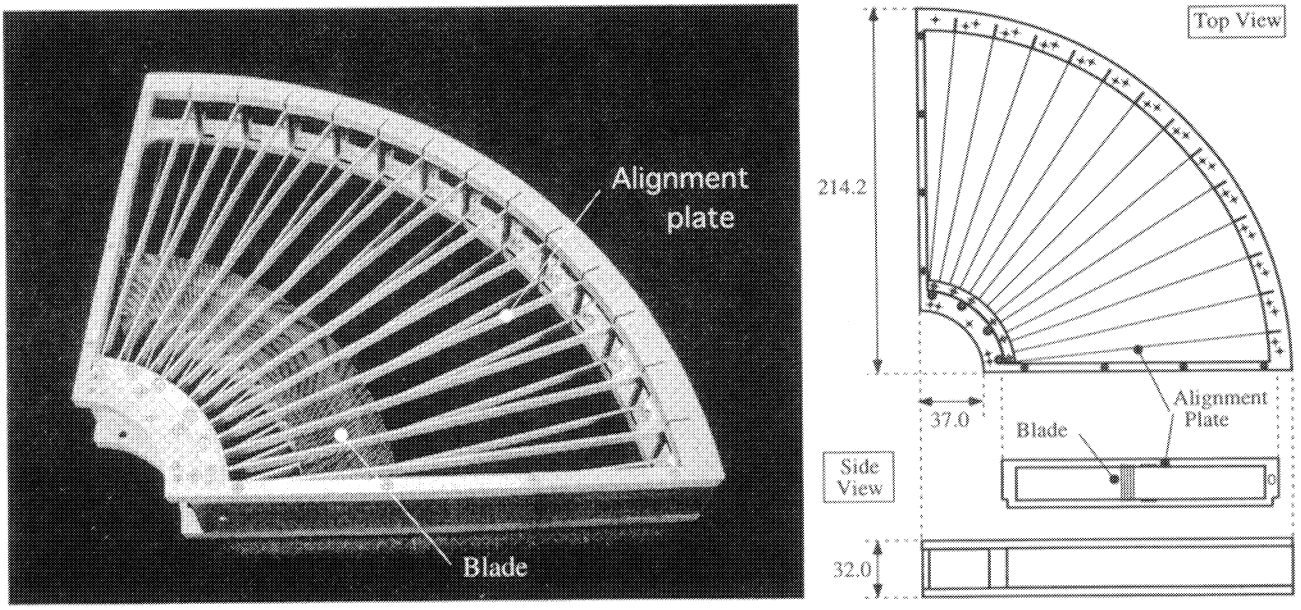

Figure 7. (*left*): Picture of ASTRO-E2 XRT pre-collimator (1 quadrant unit). This is an engineering model, and blades are installed only with radii of 80 – 110 mm from the center. (*right*): Quadrant housing of pre-collimator. 175 or 168 blades are installed in the housing. Also shown are the 13 alignment plates for supporting the blades in the housing.

Table 2. ASTRO-E2 XRT pre-collimator parameters

Blade		Housing	
Material	Aluminum	Inner Diameter	74 mm
Thickness	120 μm	Outer Diameter	428.4 mm
Height	22 mm	Height	32 mm
Offset†	8 mm	Weight	1.7 kg
Effective Height	30 mm		
Number of Nestings‡	175 / 168		
Weight	0.9 kg		

† :Distance between top of primary reflector and bottom of blade.

‡: For XRT-I and XRT-S.

4. EXPECTED PERFORMANCE OF PRE-COLLIMATOR

4.1. Ray-Tracing Simulation

In order to investigate an expected performance of the ASTRO-E2 XRT pre-collimator, we utilize the ray-tracing simulator which is developed by NASA/GSFC and is improved by us. The parameters which represent the XRT property are tuned up by referring the results of the pre-flight calibration of ASTRO-E XRTs[4]. As the property of a single reflector, thus the surface roughness with Å scale, waviness with μm $\sim$ mm scales, a point spread function (PSF), and a reflectivity on the backside, the measurement data are used and installed in the simulator. The misalignment of the reflectors in the housing is estimated by the simulator. Details are reported by Misaki et al. (2002)[5] [6]. The parameters which represent the pre-collimator property are also installed by utilizing the measurement data. The results of the surface shape, X-ray reflectivity, and X-ray reflected profile of the pre-collimator blade are summarized and discussed in Mori et al. (2002)[7].

Evaluated items are listed as follows.

- Stray light images on the focal plane with off-axis angles of 30′ and 60′.
  We check the protection effect of the secondary only reflection and a new stray light component which reflects by the pre-collimator itself (section 4.2).
- Off-axis dependence of the stray light intensity per component up to 90′ off-axis.
  We study the main component per off-axis angle and estimate the performance of the pre-collimator quantitatively (section 4.3).
- Vignetting function of XRT.
  We evaluate the XRT FOV from the off-axis dependence of the effective area, and the collimation effect due to the pre-collimator (section 4.4).
- Response for the extended sources (section 4.5).

Incident X-ray is assumed the monochromatic parallel X-ray beam (point-like source) with energy of 1.49 keV. It corresponds Al-Kα emission line utilized in the pre-flight calibration and the low energy which we can easily recognize the backside reflection. Figure 2 illustrates the coordinate system of the ray-tracing simulation.

4.2. Stray Light Image

We perform the simulation about the focal plane images with off-axis angles of 30′ and 60′, in order to check the protection effect of the secondary only reflection and a new stray light component which reflects by the pre-collimator itself. Results are shown in figure 8.

From the middle two panels [(b) and (e)] which represent the geometric effect of the pre-collimator with no reflection on the blades, it is clear that the pre-collimator well protects the secondary only reflection in the XIS

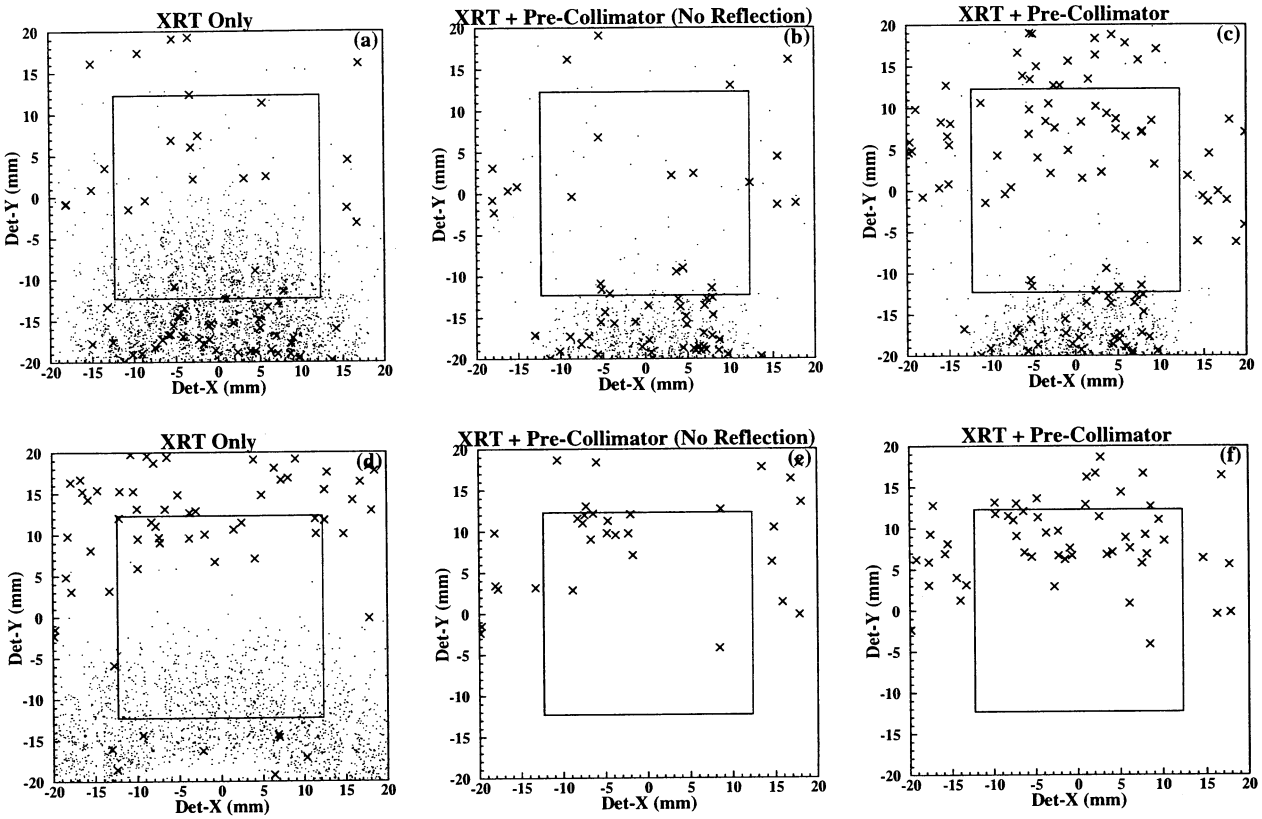

Figure 8. Simulated focal plane images with the energy of 1.49 keV. Top three panels show the images with 30′ off-axis. Left, middle and right panels indicate those in the case of the XRT only, XRT + pre-collimator with no reflection on the blades, and with reasonable reflection based on the measurement. Bottom three panels also show the same images, but showing with 60′ off-axis. Filled circle and cross marks indicate the photons classified to the secondary only and backside reflection, respectively. The XIS FOV is shown as central square with 24.6 mm × 24.6 mm size.

FOV. Since the current height of the blades (30 mm) is almost comparable with the needed height of those shown in figure 6, the area filled by the secondary only component is extremely close to the edge of the XIS FOV. In the case of $\theta = 60'$, it is sufficient height compared with the needed height for this off-axis. Then the secondary only components disappear on the focal plane perfectly.

The results, which are considered the reasonable reflection on the blades based on the measurement, are shown in right two panels [(c) and (f)] in figure 8. We can recognize the new stray light added to the backside components. These additional components roughly correspond the another secondary only component which passes through the opposite quadrant with off-axis angle of $-\theta$ after the reflection on the blades. Therefore we have to choose the blade surface which an X-ray reflectivity is as low as possible.

4.3. Off-Axis Dependence of Stray Light

Next we research the off-axis dependence of the stray light intensity per component. Results are shown in figure 9. Integration region accumulated the photons is XIS FOV, and the each intensity is normalized by the on-axis effective area. Similarly to the previous section, three conditions are assumed.

At $\theta > 8.9'$, the normal reflection component drops rapidly because of outside of XIS FOV, and stray lights appear instead. In the case of XRT only [panel (a)], the secondary only component is dominant up to $\theta \sim 70'$ with a normalized flux of 4 $\times 10^{-4}$. The primary only component disappear at $\theta > 30'$ and the backside component

stay on the FOV up to $\theta \sim 90'$. Under the condition with XRT + pre-collimator [panel (b)], Secondary only component decreases at the level of the scattering tail of the XRT PSF (thus normal component). If we consider the reasonable reflection on the blades [panel (c)], new stray light component is produced by factors of $1\sim 2$ compared with the backside component. At the small off-axis angles within $\theta < 10'$, this component increases by about an order compared with XRT only case. Finally, as more quantitative evaluation, we summarize the stray light intensities at $\theta = 30'$ and $60'$ in table 3.

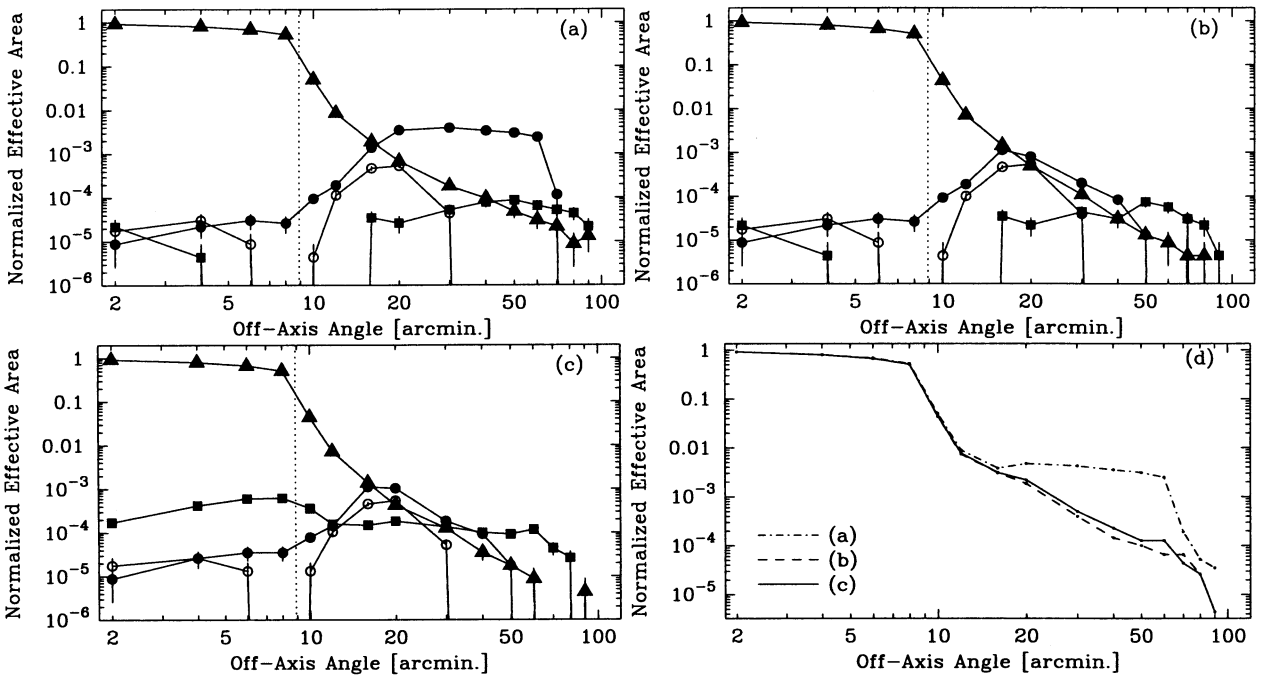

Figure 9. Off-axis dependence of the stray light intensity per component. Panels of (a),(b), and (c) indicate that in the case of the XRT only, XRT + pre-collimator with no reflection on the blades, and with reasonable reflection based on the measurement. Panel of (d) is the comparison of the other panels with total X-ray intensity. Vertical axis is normalized by the on-axis effective area. Triangle, square, filled circle, and open circle indicate the components of normal, backside, secondary only, and primary only reflections, respectively. Integration region accumulated the photons is XIS FOV. Vertical dot line corresponds the edge of the XIS FOV.

Table 3. Effective area with large off-axis angle normalized at on-axis

	Secondary Only		Multiple	
@ 30′ off-axis				
XRT Only	4.0×10^{-3}	(100%)	5.3×10^{-5}	(1.3%)
XRT + Pre-Collimator (No reflection)	2.0×10^{-4}	(5%)	4.4×10^{-5}	(1.1%)
XRT + Pre-Collimator	1.8×10^{-4}	(5%)	1.4×10^{-4}	(3.5%)
@ 60′ off-axis				
XRT Only	2.4×10^{-3}	(100%)	6.9×10^{-5}	(2.9%)
XRT + Pre-Collimator (No reflection)	~ 0	($\sim$ 0%)	5.7×10^{-5}	(2.4%)
XRT + Pre-Collimator	~ 0	($\sim$ 0%)	1.2×10^{-4}	(5.0%)

NOTE : Monochromatic parallel X-ray beam of 1.49 keV are assumed. Values in bracket show the relative value for the secondary only component without pre-collimator.

4.4. Vignetting Function of XRT

The effective area is a function of the incident X-ray angle as well as the incident X-ray energy. Figure 10 shows the angular response of the effective area at the energy of 1.49 keV. The effective area gradually decreases with the off-axis angle because of neighboring reflectors shadowing and the increase of the average incident angle. Because the former phenomenon is also made by the newly additional pre-collimator, it is possible for one of the demerit of the pre-collimator. From this figure, the vignetting function with the XRT added the pre-collimator is steeper than that of the XRT only. At the energy of 1.49 keV the FOV, which we define the off-axis angle at which the effective area becomes half of the on-axis value, is narrow by 12%.

Table 4 summarizes the FOV at the three energies, 1.49, 4.51, and 8.04 keV. In the case of XRT + pre-collimator configuration, we can confirm that the reduction rate of the FOV has slightly energy dependence. Thus it is more smaller in proportion to more higher X-ray energy. Because the current blade height (30mm) is too enough for the outer region of the telescope with $r > 110$ mm. Then such a outer region has more large grazing angles of the primary reflectors. Therefore, at more lower energies, the shadowing effect due to the collimator blades at the off-axis angles is more effective.

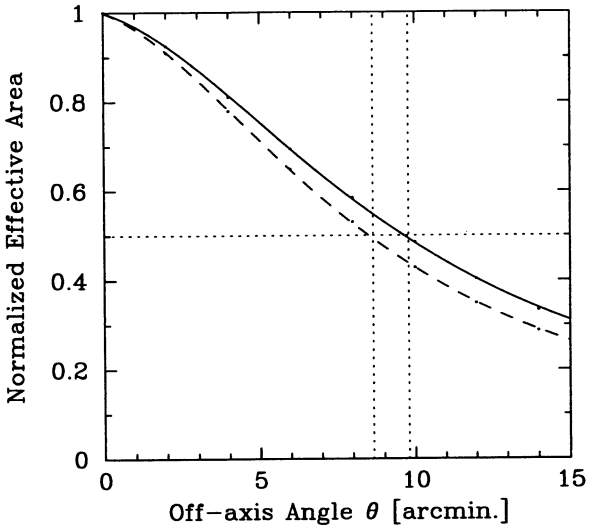

Figure 10. Vignetting function of the XRT at the energy of 1.49 keV. Vertical axis is normalized by the on-axis effective area. The FOV is defined as the off-axis angle at which the effective area becomes half of the on-axis value. Continuous and broken lines indicate the angular response in the case of the XRT only and the XRT + pre-collimator, respectively.

Table 4. Field of view of the XRT

	Field of view [arcmin.]					
	@ 1.49 keV		@ 4.51 keV		@ 8.04 keV	
XRT Only	19.5	(100%)	18.0	(100%)	13.4	(100%)
XRT + Pre-Collimator	17.1	(88%)	16.0	(89%)	12.2	(91%)

NOTE : Field of view is defined as the angular diameter at half the on-axis effective area.

4.5. Application to Extended Sources

Finally we discuss about the XRT response added the pre-collimator for the extended sources. The stray light makes it difficult to observe the extended sources, i.e., clusters of galaxies and cosmic X-ray background, as well as considerable bright point-like sources outside of FOV. Here we inspect the response for the spatially extended object with degree scales which has an uniform X-ray intensity.

For such a flat sky model, the photons in the XIS FOV which comes from the corresponding sky is calculated to be 86 % total of the accepted photons which are composed by normal reflection and stray light components,

in the case of XRT only configuration. In other words, 14 % of the total photons come from the outside of FOV. In the case of the ASCA XRT, more than half of the photons came from the outside of FOV. This improvement can be explained by the following reasons. One is remarkably small intensity of the backside reflection due to the raw aluminum surface of ASTRO-E2 XRT. The other is more smaller detector FOV than that of the ASCA GIS (FOV $\sim$ 50 mmϕ or 50$'\phi$). By applying the good performance of the ASTRO-E2 XRT pre-collimator mentioned in previous sections, we can make the photons from the corresponding sky improve to be 99% total of the accepted photons. For the next step, we need to resolve the new stray light problem due to the reflection on the blades themselves. in order to achieve the best performance.

5. SUMMARY AND CONCLUSION

Pre-collimator for the stray light protection will be installed on the X-ray telescope on board ASTRO-E2, the next Japanese X-ray astronomy satellite to be launched in February 2005. Together with the production of its engineering model, we have performed to inspect the expected performance of the pre-collimator. In order to protect effectively the secondary only reflection which has most of the stray light flux, we make vertical foil cylinders line up at the top of the primary reflectors. For further improvement, we evaluate the expected performance and weak points of the pre-collimator by utilizing the ray-tracing simulator.

If we choose the height of the pre-collimator blades to be 30 mm, we can protect all the secondary only component at $\theta > 30'$ off-axis. By the reflection on the surface of the blade, however, new stray light component is generated, especially at small off-axis angles. As a result, we estimate the total flux of the stray light to be about 10% at 30$'$ off-axis and 5% at 60$'$ off-axis, compared with the case without the pre-collimator. In order to achieve the best performance, especially for the application to the spatially extended sources, it is important to choose the blade material which has low X-ray reflectivity. On the other hands, the XRT FOV is estimated to be only about 10% less due to the collimation effect of the 30mm high pre-collimator, with slightly energy dependence.

ACKNOWLEDGMENTS

We would like to express our thanks to Richard L Fink for constructing excellent framework for the ray-tracing simulation. RS acknowledges support from the Japan Society for the Promotion of Science (JSPS) for Young Scientists.

REFERENCES

1. Kunieda, H., et al., *X-ray telescope onboard Astro-E: optical design and fabrication of thin foil mirrors*, Appl. Opt. **40**, 553, (2001)
2. Hayashida, K., et al., *Soft X-ray response of the prototype CCD camera (XIS) for Astro-E, Proc. SPIE* **3445**, 278, (1998)
3. Mitsuda, K., et al., *The XRS system — the first cryogenic X-ray detector in orbit*, Nucl. Instrum. Methods in Phys. Res. A **436**, 212, (1999)
4. Shibata, R., et al., *X-ray telescope onboard Astro-E. II. Ground-based x-ray characterization*, Appl. Opt. **40**, 3762, (2001)
5. Misaki, K., et al., *Error budgets for the image degradation of X-ray telescope onboard Astro-E, Proc. SPIE, this proceedings*
6. Misaki, K., et al., *in preparation*
7. Mori, H., et al., *ASTRO-E2 pre-collimator for stray light protection II: fabrication and X-ray calibrations, Proc. SPIE, this proceedings*
8. Chambure, D. de., et al., *The X-ray telescopes for the ESA XMM Spacecraft, Proc. SPIE* **3444**, 313, (1998)

ASTRO-E2 XRT Pre-Collimator for Stray Light Protection II. — Fabrication and X-ray Calibration

Hideyuki Mori[a], Ryo Shibata[b], Yoshitomo Maeda[a] Kazutami Misaki[a], Yoshito Haba[a], Kei Itoh[a], Ryo Iizuka[a], Taijiro Morihisa[a], and Hideyo Kunieda[a] Akira Hayakawa[c], and Manabu Ishida[c]

[a]Institute of Space and Astronautical Science,
3-1-1, Yoshinodai, Sagamihara, Kanagawa, 229-8510, Japan
[b]Department of Physics, Nagoya University,
Furo-cho, Chikusa-ku, Nagoya 464-8602, Japan
[c]Tokyo Metropolitan University,
1-1, Minamiohsawa, Hachiohji, Tokyo, 192-0397, Japan

ABSTRACT

ASTRO-E2 XRTs adopt Wolter Type-I optics and have nested thin foil structure to enhance their throughput. But this structure allows stray X-rays to come from the sky out of the XRT field of view. Stray light contaminates focal plane images, especially in the case of extended source observations. We intend to mount pre-collimators on top of the ASTRO-E2 XRTs to intercept stray light. On the other hand, reflection by the pre-collimator itself newly creates secondary stray light. To decrease these additional stray light as possible, the mil finish aluminium with its roller mark normal to the incident X-ray beam has been used for the slat material, whose reflectivity is reduced down to 1/20 of ideal specular reflection. Optical profilers tell us these samples have very rough surfaces, whose height varies with σ = 1-2 μm. According to the design parameters as are described in the related paper in this symposium (Paper I), an engineering model pre-collimator is fabricated with 46 slats out of 175. Before EM pre-collimator is mounted onto XRT, alignment plates are adjusted to align slats to the same position of XRT primary reflectors. In X-ray measurements, stray light images and the flux of each stray light component at 30′ off axis are measured with/without EM pre-collimator. The secondary only reflection component is reduced down to 3.6%, and the backside reflection component becomes more remarkable. On the other hand, X-ray measurement of the effective area at on axis with/without EM pre-collimator verifies that pre-collimator does not interfere the telescope aperture. In addition, the decrease of XRT field of view is ~10%, which is the same as the ray-tracing simulations. As a whole, EM pre-collimator reduces stray light to 27% level with only ~10% decrease of the XRT F.O.V..

Keywords: XRT, stray lights, pre-collimator

1. INTRODUCTION

1.1. Stray Light

At present, for the X-ray astronomical satellite, X-Ray Telescopes (hereafter XRTs) are necessary observational modules because of the improvement of X-ray photon collection and background reduction, for example, due to cosmic X-ray background, charged particles and so on. Different from visible light, X-ray has the nature that it is not subject to total reflection until its incidence becomes the extreme grazing angles.

Further author information: (Send correspondence to H. Mori)
H. Mori: E-mail: mori@astro.isas.ac.jp
Institute of Space and Astronautical Science, 3-1-1, Yoshinodai, Sagamihara, Kanagawa, 229-8510, Japan

Therefore, present XRTs adopt Wolter Type-I grazing optics which consists of confocal hyperboloid and paraboloid reflectors. In this optics, X-rays are reflected only one time on each reflector and reaches the focal plane.

ASTRO-E2 to be launched in 2005 is equipped with five XRTs (four XRT-Is and one XRT-S) which adopt the conical approximation of Wolter Type-I optics. Especially, ASTRO-E2 XRTs have the structure called "nested thin foil mirrors" which consists of coaxially nested 170 micron thin reflectors in order to achieve large effective area despite of light weight.

But this structure, because of tightly nested reflectors, X-rays which have slightly tilting angle of incidence from telescope optical axis go through the complicated paths in the XRTs, reach to the focal plane, and contaminate the images in the detector. These X-rays are called "Stray lights".

Actually, in the ASCA, previous Japanese X-ray astronomy satellite, these stray lights were serious problem with the prototype of the nested thin foil mirror telescope. Especially, in the observations of diffuse targets, for example, the envelope of clusters, survey of the Galactic plane and the cosmic X-ray background, stray lights contaminate the images and degrade the statistical precision of spectrum.

1.2. Pre-Collimator

To solve this problem, we are going to mount a pre-collimator on top of ASTRO-E2 XRTs. Pre-collimator has coaxial thin cylinders about 30mm high located at the position of the top of XRT primary reflectors. Therefore pre-collimator protects XRTs from the "secondary only" reflection component effectively, which is the dominant component of the stray lights (Paper I. Shibata et al. 2002 in this symposium) and goes just above the primary reflectors.

We have made the engineering model (hereafter EM) of pre-collimator for the XRT-I spare quadrant. In this paper, we report the results from the EM pre-collimator fabrication to the X-ray calibration. We show the fabrication of EM pre-collimator and adjustment of EM pre-collimator relative to XRT in §2. Then, in §3, we mention the material selection of pre-collimator slats from the view points of reflectivity to reduce the secondary stray light by the pre-collimator reflection itself. Finally we describe the EM pre-collimator performance based on the X-ray measurements in §4.

2. FABRICATION OF ENGINEERING MODEL PRE-COLLIMATOR

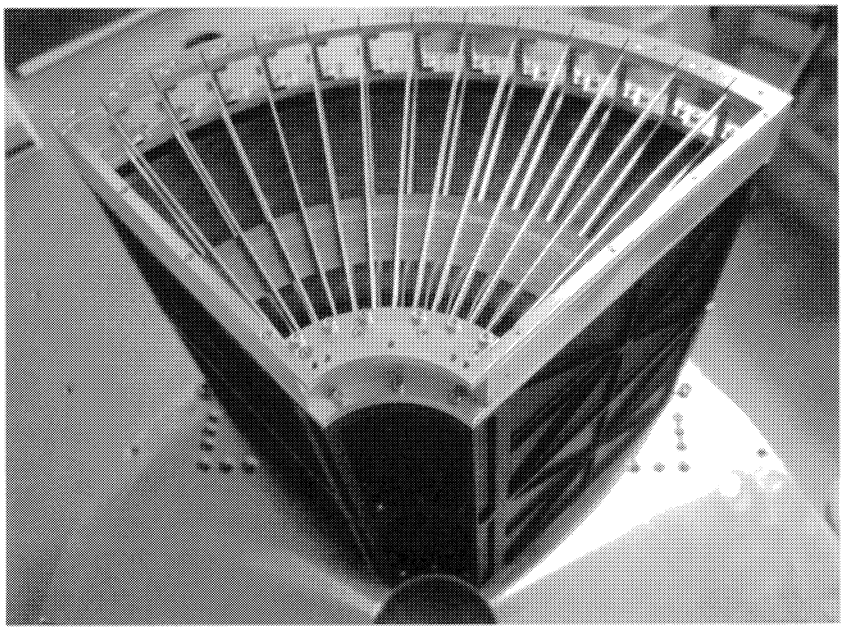

Figure 1. Picture of the EM pre-collimator mounted onto XRT-I spare quadrant — Slats are installed at the radial position of R = 80.9mm - 109.6mm to protect the secondary only reflection component at 30′ off axis

Detail of EM pre-collimator design and its structure are described in Paper I. In Fig. 1, we show the picture of the EM pre-collimator mounted on the XRT-I spare quadrant. Our main purpose is to verify the rejection of stray light by pre-collimator. As a result of the ray-tracing simulations, the secondary only reflection component, which is dominant in stray light, becomes most outstanding at ~30′ off axis. At this off axis, the R = 80 – 110mm reflectors contribute to this component. Therefore we have prepared only 46 slats at these radii for the EM pre-collimator. In this section, we mention briefly the procedure of EM pre-collimator fabrication, especially slats insertion into the housing, and adjustment of the plates which keep slats at the precise radial position.

2.1. Preparation of Slats Insertion

As a consequence of ray-tracing simulations, space between the primary reflector top and the pre-collimator slat bottom should be less than 8mm to avoid the secondary only reflection component through this gap. Distance between the top of primary reflectors and telescope surface is 5mm and the bottom plate of pre-collimator housing has 5mm thickness. On the basis of this configuration, we design the groove bottom to be 3mm from the surface of XRT. Before slats are inserted into alignment plates, we should lift the alignment plates 2mm to escape from the bottom plate thickness. For this process, alignment plates have the elongated hole to keep them on the outer side (See Fig. 2 (upper panel)).

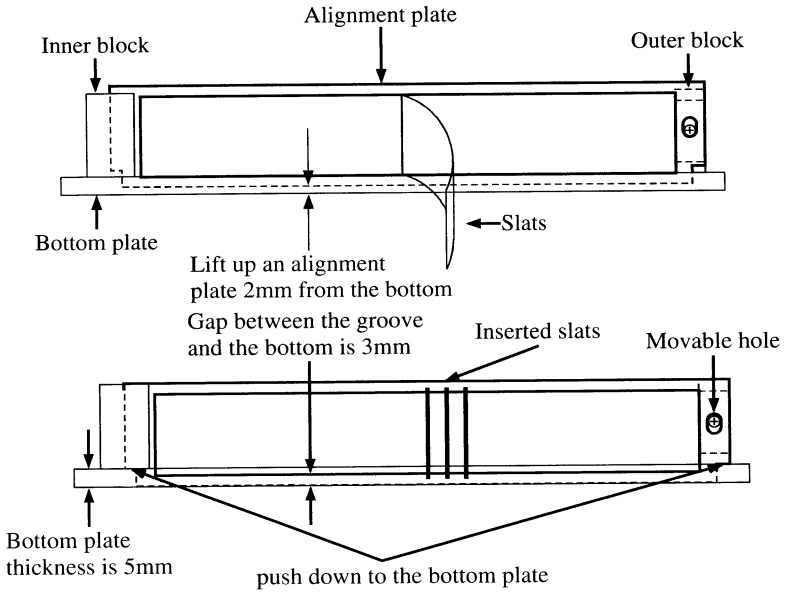

Figure 2. Schematic view of inserting slats into the alignment plate — To avoid the bottom plate thickness, alignment plates are lifted up and attached to the outer block (upper panel). After insertion of slats, alignment plates are pushed down to the bottom (lower panel).

2.2. Alignment Procedure of the Plates

First of all, we have inserted #40 slat into the pre-collimator for the time being. Then we have examined the position of the #40 groove by using the microscope equipped with a CCD camera mounted on a movable stage. This stage has a ring against which the R = 37.0mm flange of XRTs and pre-collimator can be mated, hence we can measure the radial distance from the reference point of the housing (R = 56.8mm). Then the alignment plate has been adjusted to locate the #40 slat at the nominal position of R = 80.9mm.

After adjusting 13 alignment plates in the same way, the other slats have been inserted into alignment plates. After all slats have been installed in the pre-collimator, alignment plates are pushed down to the bottom to return the slats to nominal height. (See Fig. 2 (lower panel)).

Next we have investigated the primary reflector position of XRT-I spare quadrant by using the same system. Here the #40 reflector actual position from the ring center has been measured. Then we have adjusted alignment plates for the #40 slat to be located at the same radial position as the XRT reflector #40.

Finally the EM pre-collimator has been mounted onto XRT-I spare quadrant to match the inner flanges of R = 37.0mm. Then we have illuminated the XRT-I spare quadrant + EM pre-collimator with an optical parallel beam created by an inverse telescope. The collected optical flux measured by the photo diode sensor has been compared with/without pre-collimator. When both flux becomes almost the same, we are sure that 46 slats are aligned without interfering the telescope aperture.

3. CHARACTERISTICS OF PRE-COLLIMATOR SLATS

Pre-collimator on XRTs has not only the merit of protecting from stray lights but also some demerits. One of these demerits is secondary stray lights which are created by pre-collimator reflection itself. To reduce these stray lights, we should select the adequate material of the pre-collimator slats. We have selected aluminium which is the same material used for the substrates of XRT reflectors and housings because thermal expansion coefficient is the same. Then X-ray characteristics, especially the incident angle dependence of reflectivity and scattered beam profile, have been measured about with samples with various surface processings.

3.1. Measuring System

Measurements of reflectivity and reflected X-ray beam profile have been performed in the X-ray beamline facility of the Institute of Space and Astronautical Science (ISAS). In Fig. 3, we show the schematic view of the ISAS X-ray beamline.

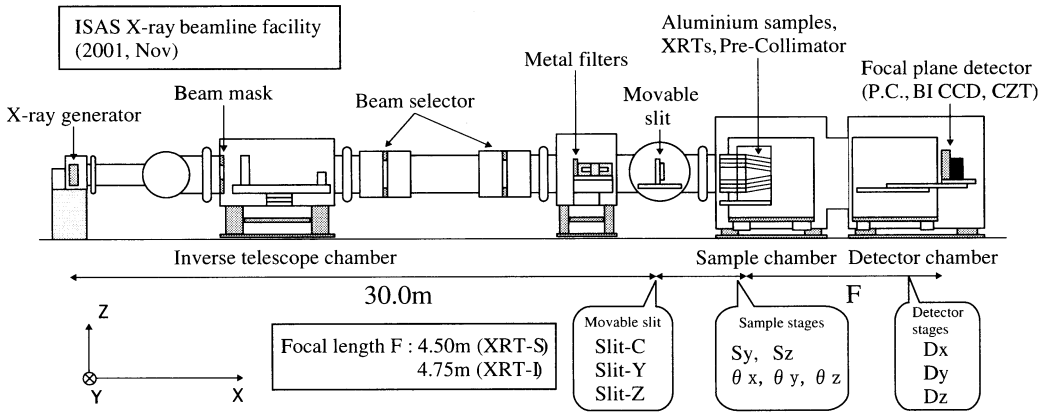

Figure 3. The ISAS X-ray beamline facility

The X-ray generator (RIGAKU RU-200) is equipped with a water-cooled rotary type target. High voltage of the 5 – 20 kV between the cathode W filament and anode metal target produces continuum X-rays by bremsstrahlung and characteristic X-ray lines of the target metal. Currently C, Al, Ti, Cu and Pt are available. In this paper, Al target is always used because stray lights become outstanding at low energies.

In the filter section, there are Al, Ti and Ni metal filter and double crystal monochromator. To get pseudo-monochromatic Al-Kα line, Al metal filter with 15μm thickness is used. 30m away from X-ray generator, movable slits are installed. We can control the size of the slit widths in the Y and Z directions, and the center position of the slit window in the Y direction. Here X-ray beam is narrowed efficiently and reached to pencil beam with highly parallelism ~15" at the beam size of 2mm × 2mm.

To illuminate the full aperture of XRT by the X-ray pencil beam, we install the movable stages in the sample chamber and the detector chamber to move the XRT and detectors simultaneously. Both stages can move in

the Y and Z directions. The detector stage can also move in the X direction to adjust the distance between the XRT and the detectors. The X stage in the sample chamber is moved manually. In addition, we have triaxial rotational tables for XRT. Among them, the rotational tables around the Y and the Z axes are used for off axis measurements.

Three kinds of detectors, Propotional Counter (P.C.), CCD and CZT are now available in the ISAS X-ray beamline.

P.C. is operated with the P10 gas (90% argon and 10% methane) flow at 1 atm. At the entrance of P.C. window, aluminized mylar is attached to cover 12mmϕ area. Note that P.C. has no imaging capability, and is mainly used to measure the absolute X-ray flux.

The charge coupled device (CCD), which is back-illuminated type, has a 1024 × 1024 array of pixels, and the size of each pixel is 24μm × 24μm. It can thus cover 18.4′ × 18.4′ for the XRT-I. In spite of operating temperature at –70°C, CCD backgrounds have some distribution, therefore it is used to investigate the image quality for XRTs or image position with its image capability.

3.2. X-ray Reflectivity and Reflected Beam Profile of a Slat

We show the schematic view of the measuring method for reflectivity and reflected beam profile in Fig. 4. Aluminium foil is rolled, hence we make their generated line to be parallel to the X-ray beam.

After the sample is adjusted to be parallel to the incident X-ray beam, we rotate the sample so that the angle between the generated line and the incident X-ray is θ_z. And the detector Y stage (Dy) is simultaneously controlled to move P.C. at the specular position of reflected X-ray beam (If the distance between the sample and detector is L, the specular position is calculated to be $L \times \tan 2\theta_z$). Here the reflected X-ray beam intensity is measured by P.C.. In addition, we move the P.C. to Dy = ±12mm from the specular position and reflected intensity at each point is measured to know the tail intensity, if there is.

On the other hand, reflected beam profile is measured in the following way. The sample is kept at the rotation angle θ_z. Then P.C. is scanned from the position at the diffraction angle $\theta_{diff} = -\theta_z$ to the position at $\theta_{diff} = 2°$ with ΔDy = 6mm pitch. Here the diffraction angle is defined as the angle measured from the specular position. The reflected beam profile in large angle is measured by P.C.. In the following figures, the reflected beam intensity is normalized by the direct beam intensity.

Note that the reflectivity calculated by the some of the measured intensity at the specular position and ΔDy = ±12mm represents only a part of the reflected X-ray beam within three times of P.C. F.O.V.. Therefore the total reflectivity is calculated by multiplication of the normalization factor based on the comparison of the intensity within three times of P.C. F.O.V with the intensity integrated over the wide distribution.

First of all, the samples which used for the substrate of ASTRO-E reflectors, "1100 name plate", "1100 mil finish" and "2024 mil finish", have been examined. Aluminium is classified by its purity and surface processing. Generally speaking, the series of 1000 are almost pure aluminium. Other series from 2000 to 7000 are mixed with other metals, for example, Cu, Mg, Zn to increase the hardness. Surface processing is represented by "name plate", "bright finish" and "mil finish" and the aluminium surface becomes rougher in this order. Especially, roller marks appear more clearly on the mil finish surface. The reflectivity and reflected beam profile is shown in Fig. 5. As a result, the 2024 mil finish sample has the lowest reflectivity and its reflected beam profile has the broad tail to the large diffraction angle without the specular core.

Next 1100 name plate, 1050 mil finish and 5056 mil finish which is easily obtained commercially have been examined. Since the diffraction becomes larger when the marks are perpendicular to the incident beam, the aluminium slats are oriented so that the roller marks is normal to the X-ray beam. The result of these reflectivity is shown in Fig. 6. Based on these measurements, it is confirmed that the processing of mil finish is proper for the slat material of pre-collimator and that purity does not influence the reflectivity. In addition, roller marks oriented to be normal to the incident X-ray reduces the reflectivity as an exponential function of the incident angle.

Therefore we have finally decided the mil finish aluminium, classified into 1N30 as the material of EM pre-collimator slats. This aluminium has been examined for the reflectivity and reflected beam profile by using three

kinds of energy, 1.49keV (Al-Kα), 4.51keV (Ti-Kα), and 8.04keV (Cu-Kα) at the 10m ISAS X-ray beamline facility. The 10m X-ray beamline has the almost same structure of 30m X-ray beamline described in §2.1. The reflectivity and reflected beam profile is shown in Fig. 7.

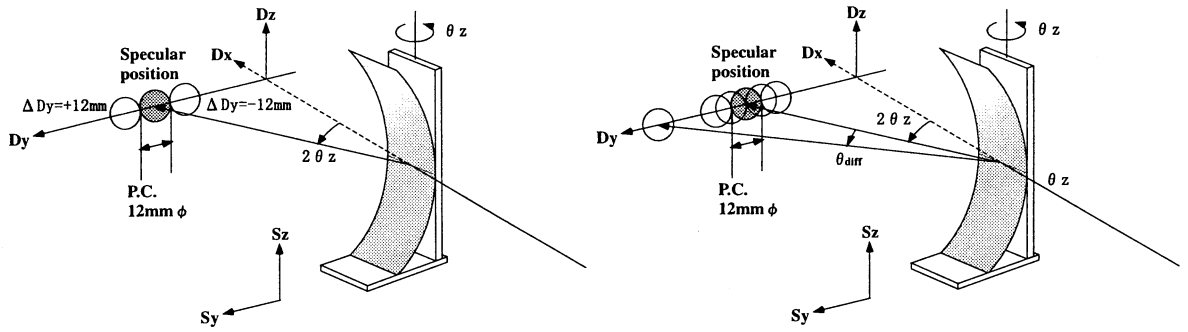

Figure 4. Schematic view of the measurement of reflectivity (left) and reflected X-ray beam profile (right)

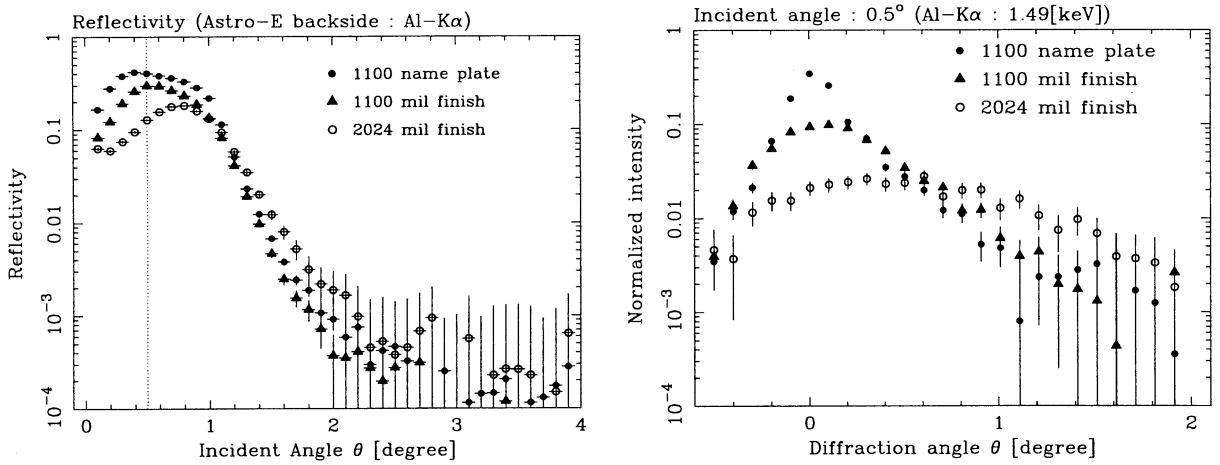

Figure 5. Reflectivity (left) and reflected beam profile (right) of aluminium used for the substrate of ASTRO-E reflectors — Note that the reflectivity at the left side of dotted line is underestimated because the effective width of aluminium surface is smaller than the X-ray beam size.

3.3. Surface Examination by Using Optical Profiler

We have examined the alminium surfaces directly by using optical profiler (MITAKA NH-3, NH-6). NH series are the system which consists of the X and Y mechanical stages with the 1μm accuracy and the cylinder with optical laser movable to Z direction. Laser spot size reaches to 1μm by using the objective lens. Some aluminium surface profiles have been measured in the range of 5mm with 1μm pitch in the two scanning directions, normal and parallel to the roller mark. These results are showed in Fig. 8. It tells us that mil finish surface is very rough with the height distribution fitted by Gaussian with $\sigma \sim$ 1-2μm and that the waviness measured in the normal direction to the roller mark has more power in shorter surface wave length than the one in the parallel direction.

3.4. Alminium Reflectivity with Very Rough Surface

Understanding the reflectivity and the reflected beam profile with very rough surfaces is necessary for ray-tracing to reproduce the results of X-ray calibration of XRTs + pre-collimator. But multiplying the ideal reflectivity

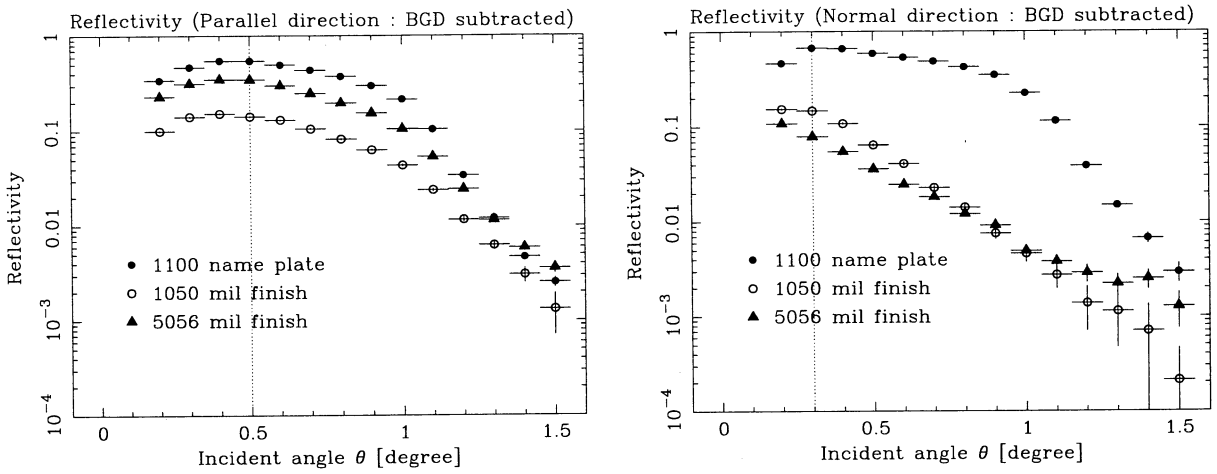

Figure 6. Reflectivity for some aluminium samples — The roller mark is set to be parallel (left) and normal (right) to the incident X-rays. The reflectivity at the right side of dotted line is reliable.

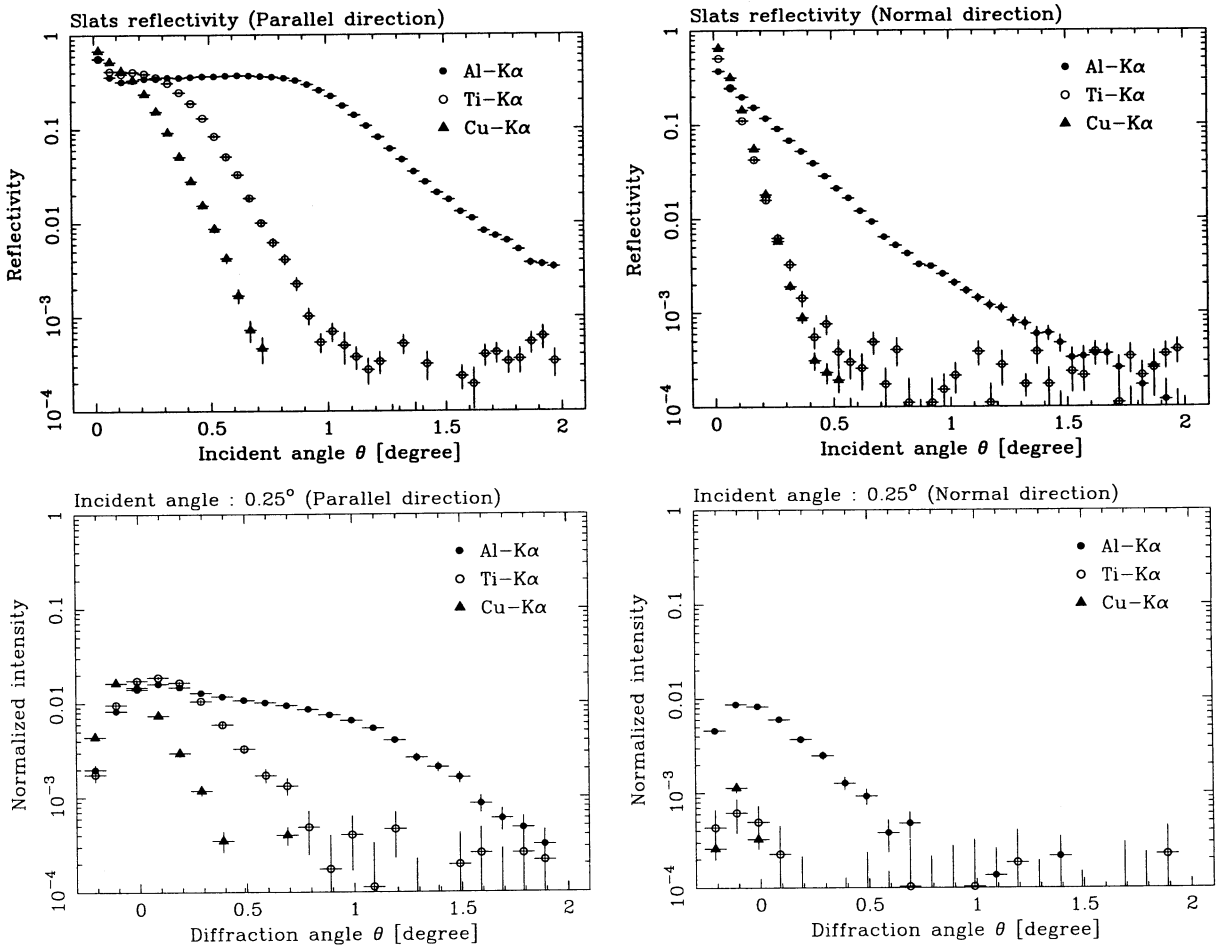

Figure 7. Reflectivity and reflected X-ray beam profile for 1N30 which is used to the slat material for EM pre-collimator — The roller mark is located to the parallel (left) and normal (right) direction to the incident X-rays.

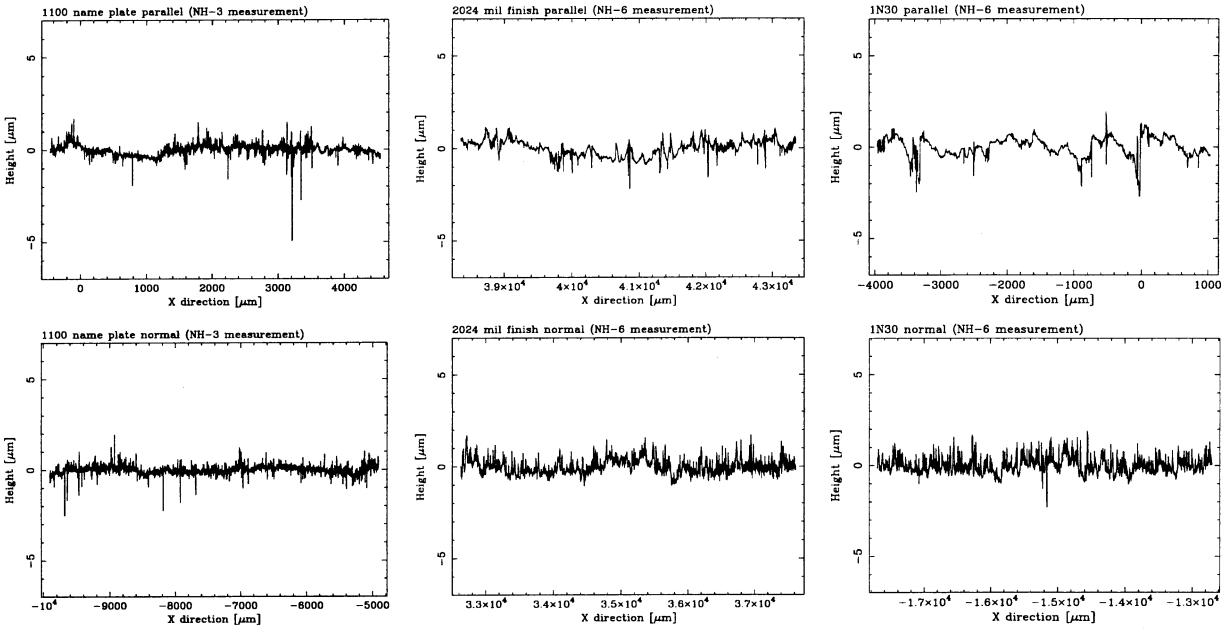

Figure 8. Aluminium surface examined by the optical profiler — scanning path is set to the parallel direction (upper panel) and normal direction (lower panel) to roller marks, and aluminium samples are 1100 name plate (left), 2024 mil finish (center), 1N30 (right) respectively.

by Debye-Waller factor is inadequate because the roughness is much larger than the wavelength of incident X-ray. We interpret this result in the following. In the parallel direction, the groove of the roller mark has the gradual undulation, hence X-ray beam can be strongly scattered to the small diffraction angle. But in the normal direction, the roller marks make shadow on the aluminium surface, then the reflection is occured within the only small fraction of the surface. Thus the reflectivity is decreased rapidly and reflected beam profile has the narrower shape compared to the parallel one.

4. X-RAY MEASUREMENT OF PRE-COLLIMATOR PERFORMANCE

We have measured X-ray characteristics of XRT with EM pre-collimator at the ISAS X-ray beamline facility. At first, on axis throughput or effective area of XRT is measured with and without the pre-collimator to confirm that pre-collimator does not obscure the opening area of XRT. The angular response of XRT is measured with and without the pre-collimator, which should reduce the XRT field of view (F.O.V.). At 30′ off axis, the focal plane images are compared with and without the pre-collimator, to confirm the performance to protect stray lights through XRT. Here we have equipped Al target into X-ray generator which is operated by 6kV10mA and have used the 15μm Al filter to get pseudo-monochromatic Al-Kα (1.49[keV]).

4.1. EM Pre-Collimator Transmission

First we have examined the characteristics of EM pre-collimator itself, especially slat thickness.

The pre-collimator orientation is first adjusted to give maximum transmission. The shadow of a slat is observed by a CCD camera. It tells the effective thickness of 120 ± 24μm (CCD pixel size) after subtracting the beam divergence.

Then we have measured the X-ray flux with/without EM pre-collimator by the scanning with the X-ray pencil beam over the area where slats are installed at the radial position of R = 80.9 – 109.6mm. As a result, both X-ray flux are 35.96 ± 0.27cm^2 and 50.73 ± 0.34cm^2 respectively and X-ray transmission of the EM pre-collimator is calculated to be 68.9 ± 0.7%. This transmission is less than the geometrical transmission of

72.8%. It is considered that the decrease of transmission is caused by slats waviness and slight tilting in the groove. Finally the effective thickness of slats has been estimated to be 132μm. Above result tells us that pre-collimator does not reduce the XRT effective area, because the XRT reflectors thickness is 170μm and slats are 38μm thinner, and have no more than 10μm play at one side of the groove.

4.2. Effective Area

As is described in §2.2 and §4.1, optical parallel beam and slats effective thickness indicate that EM pre-collimator by no means intercepts the telescope aperture. Then we have compared the effective area at on axis in the case of XRT-I only and XRT-I + EM pre-collimator as the next step. We have measured the effective area over the all of spare quadrant and the area where slats are installed (R = 80.9 – 109.6mm) by scanning with X-ray pencil beam, called "raster scan method" (Shibata et al. 2001, the schematic view in Fig. 9). In Table 1, we summarize the effective area at on axis with/without pre-collimator and its loss rate. These result prove that the loss of XRT effective area at on axis by the pre-collimator slats is avoided by the accurate alignment described in §2.

Table 1. Effective area at on axis with/without EM pre-collimator

	XRT-I only [cm^2]	XRT-I + pre-collimator [cm^2]	(%)
All parts	109.2 ± 0.8	107.4 ± 0.8	98.4 ± 1.0
pre-collimator parts	18.82 ± 0.18	18.39 ± 0.18	98.9 ± 1.1

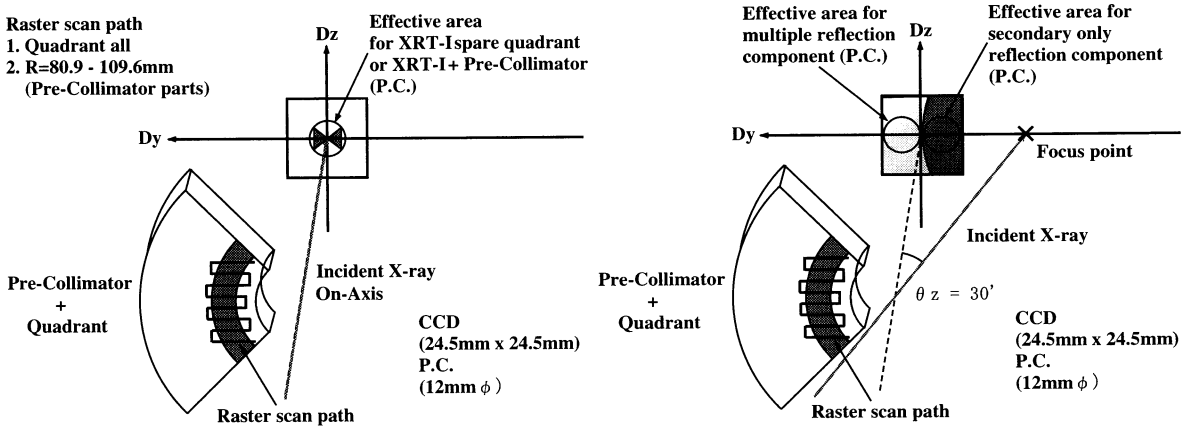

Figure 9. Schematic view of the measurement of the effective are at the on axis (left) and the stray light images at the 30′ off axis (right)

4.3. XRT F.O.V.

The pre-collimator placed onto a XRT reduces the XRT F.O.V.. Here the XRT F.O.V. is defined by FWHM of the angular response. X-ray flux becomes half compared to the one at on axis. We have measured the X-ray flux with/without EM pre-collimator at several off axis angles to get the vignetting function (See Fig. 10). The X-ray beam scanned over the slats part (R = 80.9 – 109.6mm) in the radial direction parallel to the tilting where the vignetting effect becomes most remarkable. These results are fitted with Gaussian and each σ, is 3.74′ (θ_{FWHM} = 8.80′) and 3.46′ (θ_{FWHM} = 8.15′) respectively. About 10% reduction of σ is consistent with the ray-tracing simulations. We can estimate the reduction of XRT F.O.V. in the case of full telescope to ∼ 10% based on the ray-tracing simulations.

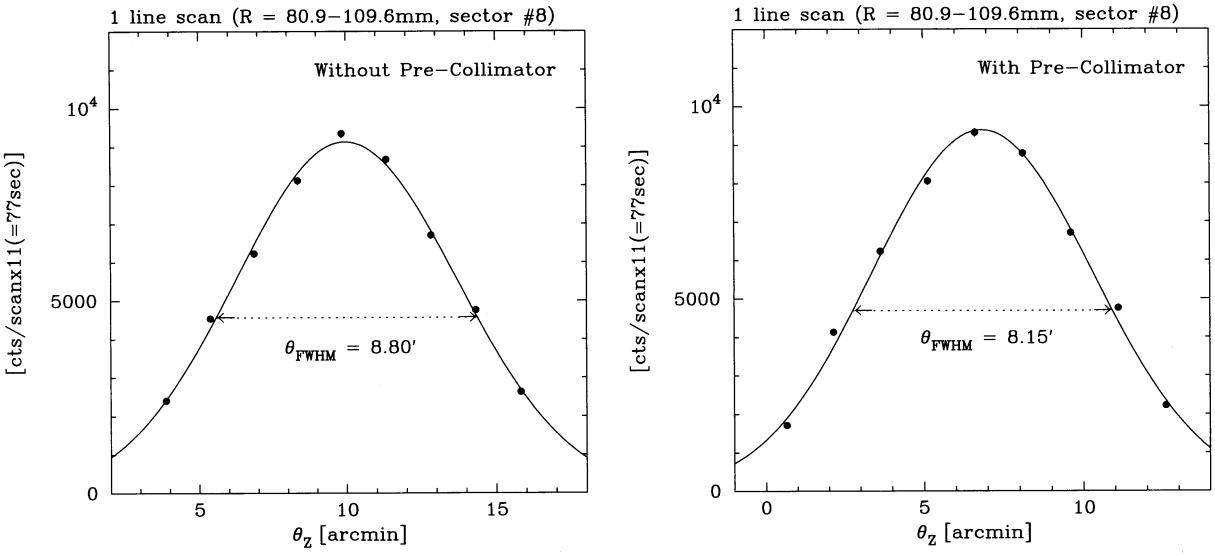

Figure 10. The angular response of the effective area with (right) and without (left) EM pre-collimator

4.4. Stray Light

Finally we have seen the focal plane image at 30′ off axis by using CCD camera. Without EM pre-collimator, the secondary only reflection component is clearly visible at the near side of the telescope axis (See Fig. 11). On the other hand, the backside reflection component appears in the opposite side much weaker than the secondary only. Once the EM pre-collimator is attached, the bright stray component seen in Fig. 11 (left) perfectly disappears in the right panel.

Then we have measured the effective area of each component to get the accurate reduction rate of stray lights by using P.C. (In Fig. 9, each circle represents the P.C. field of view, 12mmϕ). These results are summarized in Table 2. It shows that the secondary only reflection component is decreased to $\sim$ 3.6% level compared to the case without EM pre-collimator. On the other hand, the backside reflection components seem to be the same. These are consistent with the results of ray-tracing simulation for ASTRO-E2 XRTs.

Table 2. Effective area of each stray light component

	XRT-I[cm^2]	XRT-I + pre-collimator [cm^2]	(%)
30′ Off-Axis			
Secondary only	0.584±0.007	0.021±0.004	3.6±0.7
Backside	0.114±0.003	0.115±0.003	–
–30′ Off-Axis			
Pre-collimator + Secondary only	–	0.028±0.004	–
Pre-collimator + Backside	–	0.024±0.004	–
Total	0.698±0.008	0.188±0.008	26.9±0.3

We have also investigated the secondary stray lights by the pre-collimator itself. The pre-collimator and XRT-I spare quadrant has been tilted at –30′ off axis, then secondary stray lights are expected to reach to the CCD camera because the reflection by the pre-collimator slats reverses the incident angle of –30′ to +30′. But we cannot find the secondary stray lights significantly and P.C. measurement of effective area indicates that the secondary stray lights is comparable to reduced secondary only reflection component. As a whole, backside

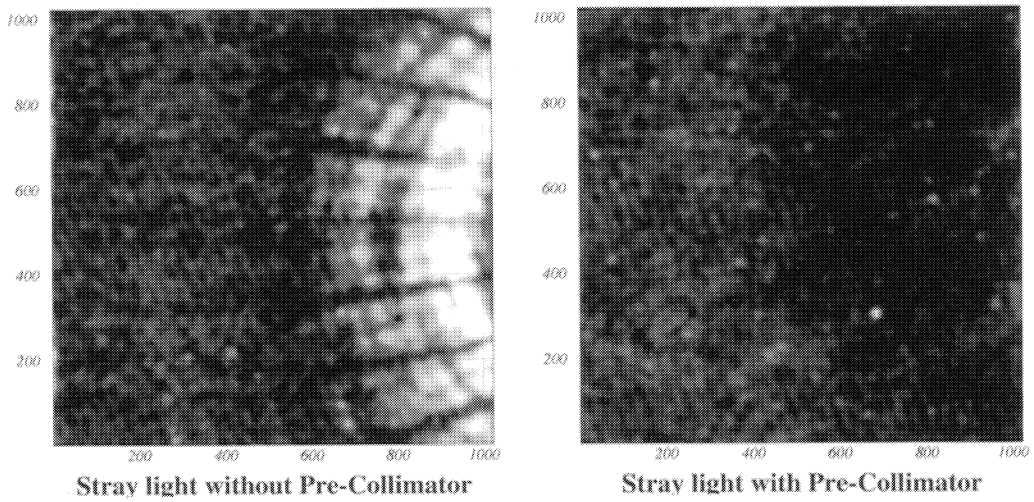

Figure 11. Stray light images at the 30′ off axis — XRT-I spare quadrant only (left) and XRT-I + EM pre-collimator (right)

reflection components become dominant in stray lights and stray lights are reduced by EM pre-collimator to ∼ 27% level.

5. SUMMARY AND CONCLUSION

X-ray characteristics of EM pre-collimator for protection the secondary only reflection component of stray lights have been examined. In the EM pre-collimator, we have decided to select the rolled alminium foil as the slat materials whose roller marks are oriented to the normal direction to the incident X-ray beam for the reduction of secondary stray lights as possible. In addition, the alignment plate with grooves is used to locate slats at the precise radial positions. X-ray measurements confirmed that EM pre-collimator decreases the secondary only reflection component to 3.6% without any loss of the effective area of XRT at on axis and that the secondary stray lights is negligible. On the other hand, the backside reflection component becomes dominant, then stray light is reduced down to 27% by EM pre-collimator as a whole. The effective width of pre-collimator slats is ∼ 132μm, therefore this does not interfere the XRT aperture because the width of the reflectors is 170μm.

We are going to the next stage of production and X-ray calibration of the prototype model pre-collimator into which all of 175 slats are installed to protect the secondary only reflection component at any off axis. And the vibration test will be carried out to examine the mechanical stiffness of pre-collimator under the actual launch of ASTRO-E2 in 2005.

REFERENCES

1. R. Shibata, M. Ishida, H. Honda, T. Endo, J. Ishida,
H. Kunieda, Y. Tawara, A. Furuzawa, Y. Ogasaka, M. Watanabe, K. Misaki, T. Yoshioka,
P. J. Serlemitsos, Y. Soong, K.-W. Chan, Y. Terashima,
"X-ray calibration of the telescopes on board ASTRO-E satellite",
X-Ray Optics, Instruments and Missions, Proc. SPIE, 1998.
2. R. Shibata, M. Ishida, H. Kunieda, T. Endo, H. Honda, K. Misaki, J. Ishida,
K. Imamura, Y. Hidaka, M. Maeda,
Y. Tawara, Y. Ogasaka, A. Furuzawa, M. Watanabe, Y. Terashima, T. Yoshioka, T. Okajima, K. Yamashita,
P. J. Serlemitsos, Y. Soong, K.-W. Chan,
"X-ray telescope onboard Astro-E. II. Ground-based X-ray characterization",
Applied Optics, 40, 3762-3783, 2001.

3. R. Shibata, H. Mori, Y. Maeda, K. Misaki, Y. Haba, K. Itoh, R. Iizuka, T. Morihisa, H. Kunieda, A. Hayakawa, M. Ishida,
"ASTRO-E2 XRT pre-collimator for stray light protection I. – design and expected performance",
in this symposium, 2002.

Normal incidence multilayer telescope for soft X-ray beam expander

Hideyo Kunieda[a], Kazutami Misaki[a], Yoshito Haba[a], Manabu Ishida[b], Kei Itoh[a], Hideyuki Mori[a], Ryo Shibata[a]

[a] Institute of Space and Astronautical Science, 3-1-1 Yoshinodai, Sagamihara, 229-8510, Japan
[b] School of Science, Tokyo Metropolitan University, Tamagawa, Chofu-shi, Tokyo, 182-0025, Japan

ABSTRACT

Normal incidence optics have been used with multilayers in EUV region. The 2d of the multilayers has to be equal to the wavelength of interest. At the same time, the reflectivity of the multilayers should decrease with the increase of the interfacial roughness much faster than grazing optics. In general, 2d of 10 nm is the shortest d-spacing available for multilayers in normal incidence. As a challenge of shorter wavelength application, we made NiCr/C multiplayer mirror for the laboratory use at 4.47 nm(carbon K alpha line). The main dish of the Cassegrain optics is 20 cm diameter spherical mirror and the secondary mirror is a reflector in aspherical shape to correct astigmatisms. Its focal point is placed at the X-ray source to create a broad parallel beam of 20 cm in diameter. The flux of the parallel beam is slightly less than the expected value, and gradually decreases about 40 % toward the outer region. The measured parallelism is about 25 arcsec, which is a little larger than the design value. More pricise positioning of the focal point to the X-ray generator may reduce such divergence. The beam profile through a slit shows a core of about 20 arcsec and an extended tail which might be due to scattering tail by the roughness of 0.3 nm. An application of this system is demonstrated with the Astro-E X-ray telescope. The image core is sharper but the scattering tail is considerable. Even after the subtraction of the tail, still some wing is left. This system is bright and parallel enough to examine the optical alignment much faster than previous method, while careful measurements are necessary for quantitative calibration of X-ray telescopes.

Keywords: Multilayer, normal incidence optics, beam expander

1. INTRODUCTION

At the Institute of Space and Astronautical Science (ISAS), all launched X-ray telescopes have been calibrated by X-ray pencil beam scanning of them.[1] The distance of 30 m from the X-ray generator to the pinhole of 2 mm provides us with a pencil beam with the divergence of 15 arcsec. The telescope and detectors are moved simultaneously to illuminate whole aperture by a fixed X-ray pencil beam. It, however, takes long time and some fluctuation has to be expected because of the wobbling and jittering of the stages. If a broad parallel X-ray beam is available as visible parallel beam, the calibration of telescopes becomes quicker and accurate. However, grazing optics in X-rays makes such inverse telescopes or a beam expander much more difficult than visible regime. The shortest wavelength for normal incidence optics was limited in EUV region, say 10 nm. A normal incident telescope is produced as an inverse telescope or a beam expander with multilayer coating tuned for the carbon K alpha X-ray at 4.4 nm by Nikon.[2] Present paper discribes its optical design, X-ray performance and test measurements with an X-ray telescope.

Further author information: (Send correspondence to Hideyo Kunieda)
Hideyo Kunieda: E-mail: kunieda@astro.isas.ac.jp, Telephone: 81 42 759 8154

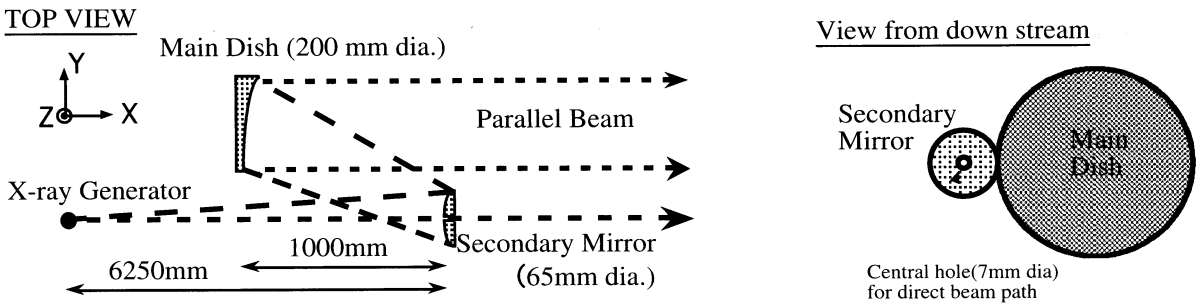

Figure 1. Configuration of the inverse telescope at ISAS.

2. OPTICAL DESIGN

The optical design of the system is a modified Cassegrain with a spherical main dish (r = 2246 mm) and the secondary reflector with special curvature designed to produce parallel beam within 5 arcsec within 20 cm diameter(Fig. 1). The combined focal length is 7250 mm from the main dish. The whole system is tuned with visible light and installed so that the focal point comes to the emitting point of the X-ray generator(Rigaku RU-200). If we assume the spot size of the X-ray source is 1 mm, we need to expect beam divergence of 15 arcsec (half width).

If we put parallel beam from the down stream, it will be converged to the X-ray generator, so that we can call this system as an "Inverse Telescope". From X-ray source point of view, the narrow X-ray beam is expanded to a broad parallel beam. Therefore, this system can be called an X-ray beam expander.

The 2d of NiCr/C multilayer is 4.47 nm and 50 and 40 layer pairs are stacked on the main dish and the secondary mirror respectively. The thickness ratio of the heavy element(NiCr) to the d-spacing is chosen as 0.5 to reduce the secondary peak of reflectivity. The fluctuation of the thickness was guarnteed less than 0.1 nm.

3. MEASURED RESULTS

The X-ray beam property has to be well established before the real use in calibration of flight telescopes. Following three characteristics are examined with a proportional counter with 4 micron polypropylene window and a CCD camera with a back illuminated chip, both sensitive for carbon K alpha X-rays.

3.1. Mirror reflectivity

Before the assembly of the inverse telescope, each mirror was examined with C-K X-rays and Al-K X-rays. Measured results are summarized in Table 1. The measured 2d is very uniform within 0.01 nm in each mirror, though the average value is a little thicker in the main dish. The measured reflectivity seems to be factor of several less than we expected from the simulation. It is partly because of the interfacial roughness and the intrinsic broadening of the C-K X-ray energy. Since the error of reflectivity at C-K is 0.05 %, the main dish is almost uniform in reflectivity, while the variation is real in the secondary mirror. The reflectivity of Al-K shows gradual decrease of reflectivity toward +Y direction in the secondary mirror. Here, we expect total efficiency of about 10**-5 after two reflections.

3.2. Intensity Distribution

The beam intensity of the 20 cm diameter parallel beam was measured by scanning of a proportional counter with a window of 12 mm diameter. Fig. 2 shows the measured beam profile looked from the down stream. Outer circle corresponds to the diameter of the vacuum duct after the inverse telescope. The C-K parallel beam is located at about 50 mm off center of the duct toward right hand side(+Y). The X-ray beam diameter seems to be about 180 mm. The flux at the center is 10-15 counts /s/cm2 with the high voltage of 10 kV and the plate current of 100 mA. The projection to horizontal direction is shown in the right panel of Fig. 2. The top

Table 1. Mirror reflectivity and multilayer parameter.

Main Dish (n = 50 layer pairs)					
Measured position	-75mm	-50mm	-25mm	0mm	+25mm
Reflectivity (C-K)	0.37	0.46	0.38	—	0.42
Reflectivity (Al-K)	1.33	1.17	1.02	—	—
2d (nm)	4.496	4.492	4.48	—	—
Secondary Mirror (n = 40 layer pairs)					
Measured position	-25mm	-10mm	10mm	15mm	25mm
Reflectivity (C-K)	0.32	0.44	0.44	—	0.28
Reflectivity (Al-K)	0.52	1.21	1.18	0.99	—
2d (nm)	4.464	4.447	4.476	4.4464	—

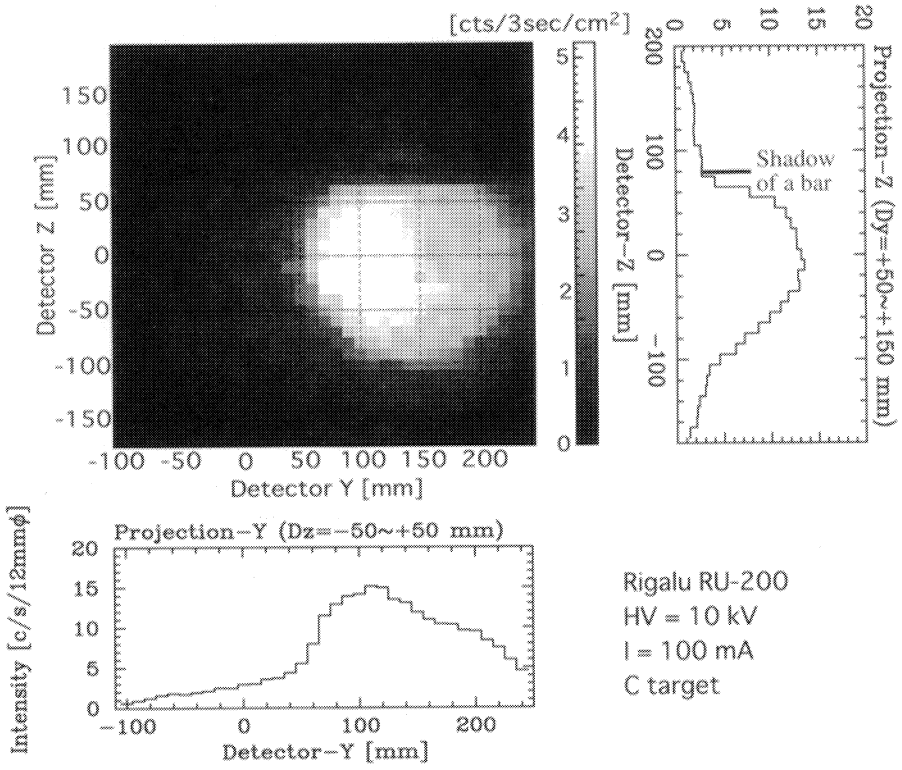

Figure 2. Measured intensity distribution of the C-K beam.

part is obscured by a metal bar in the vacuum duct. In the bottom panel, the projection in vertical direction is shown. There is a gradual decrease toward right hand side(+Y) down to 60 % of the central flux. One of the possible reasons of such tendency is the gradual decrease of reflectivity of the secondary mirror as is seen in Table 1. Another reason is the geometrical effect, where the projection size on the main dish from the same solid angle from the secondary becomes larger in the outer part of the main dish. This effect causes about 20 % gradual decrease of intensity toward +Y.

In Fig. 2, the intensity distribution has broad and strong tails in both directions at a level of 10 % of the beam center.

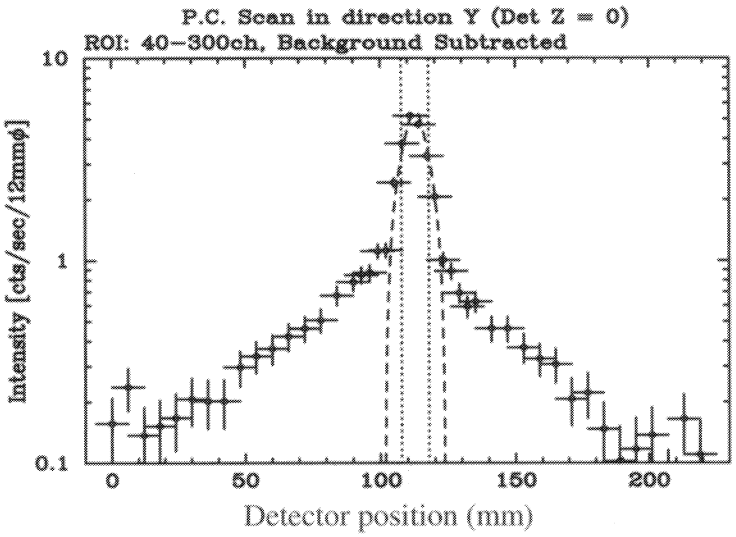

Figure 3. Measured beam profile from a slit.

3.3. Parallelism

Two reflectors are optically designed to provide the parallelism better than 10 arcsec at any spot of the 20 cm diameter beam. If the positioning of the focal point of the inverse telescope has an offset from the X-ray source, we have to expect some beam divergence. For example, if the X-ray source is placed 20 mm off in Y(horizontal) direction, about 10 arcsec more divergence (20 arcsec in total) is expected in horizontal plane based on simulations. Other deviations in X and Z directions cause additional divergence less than 5 arcsec.

We have measured the direction of beams at 4 positions (top, bottom, right and left end of the main dish). In vertical direction, two beams are parallel within 5 arcsec. In horizontal direction, two beams are 26 arcsec different each other. Since the measurement errors are about 10 arcsec, a significant off set of about 20 mm seems to be there in Y direction or an angular off set of about 8 arcmin. We may need more accurate positioning of the inverse telescope against the X-ray generator.

3.4. Scattering

In order to measure the beam divergence and scattering at each position, a 10 mm slit is placed one meter away from the main dish. The beam profile was measured by a proportional counter with 12 mm diameter window placed 30 m away. Fig. 3 shows the measured results with crosses and the expected profile in an ideal beam with a dashed line. It seems to be clear that the core is almost identical to the nominal profile, while broad tail is quite high. It means that X-rays coming out from the main dish is the combination of a straight parallel beam and beam diverging in various directions. The integrated intensity of the scattering component is comparable to the central beam. It is possible to explain such strong scattering by the surface or interfacial roughness of 0.3 - 0.5 nm. It is because the equation[3] to estimate the scattering intensity from the surface roughness has the " sine " factor of incident angles. In grazing incidence, this factor (= sin 1 (degree)) is 1/60, while it becomes 1 for the normal incidence. Therefore, even with an extremely smooth mirrors we need to expect such strong scattering component. The loss of flux into the scattering component also causes lower reflectivity (0.3 %) than we expected ($\sim$ 1 %).

4. APPLICATION FOR THE TELESCOPE CALIBRATION

A spare telescope of AstroE XRT[4] was illuminated by the parallel C-K X-ray beam and its X-ray image was detected by a back illuminated CCD camera. When the telescope was illuminated by the ordinary pencil beam, the image shown in the right panel of Fig.4 is detected by the same CCD camera. This is the focal plane image

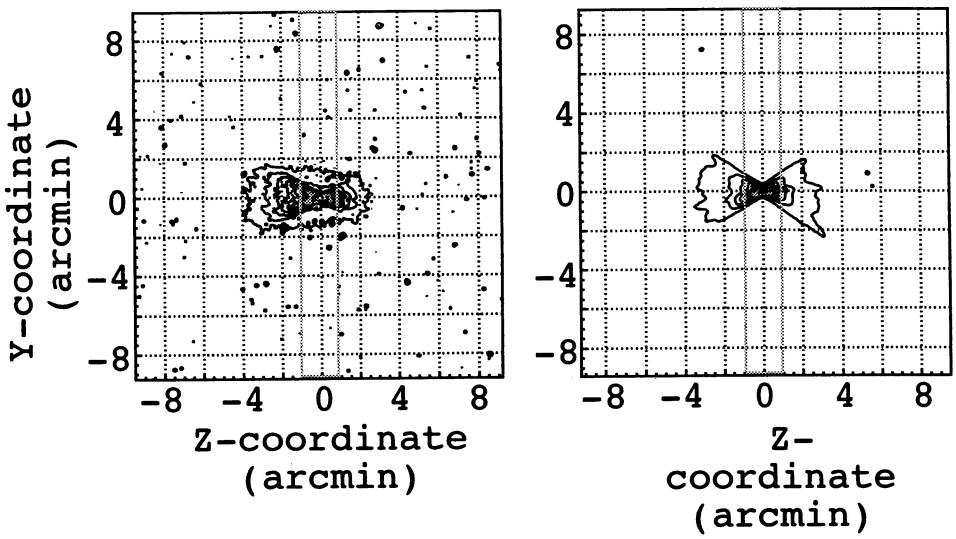

Figure 4. Measured focal plane images of XRT with the parallel beam (left) and a pencil beam (right).

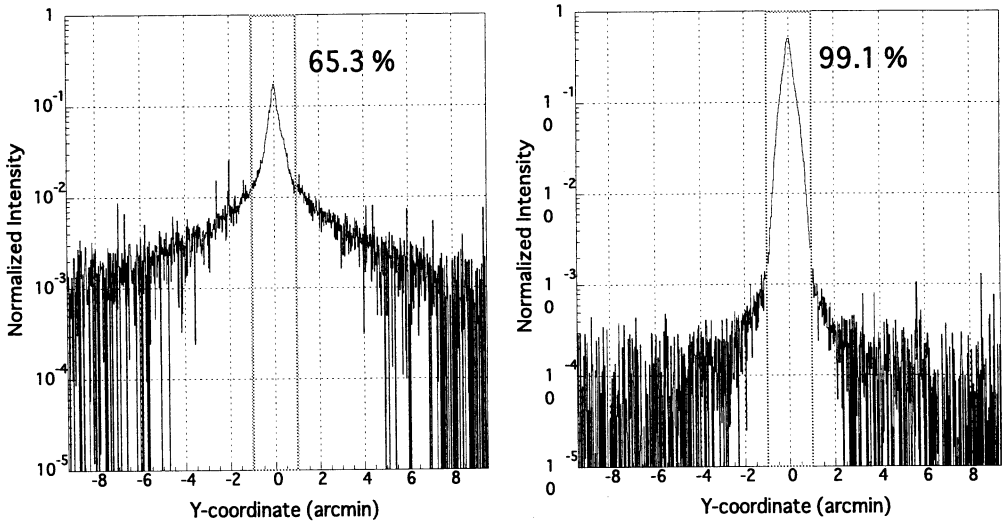

Figure 5. Projection of the focal plane images with the parallel beam (left) and a pencil beam (right).

of a quadrant and then it is limited in the azimuthal angle +/- 45 degrees from horizon. Similar image is taken with the parallel C-K beam as is shown in the left panel of Fig. 4.

In two panels of Fig. 5, the intensity distribution in the belt between two vertical lines at +/- 1 arcmin in Fig. 4. As is mentioned above, X-ray flux is limited within +/- 45 degrees from the horizontal axis. Therefore the intensity distribution in vertical direction at the image center should not have wings or tails and 99 % flux should be included within +/- 1 arcmin, as is seen in the right panel of Fig. 5. In other words, the tails seen in the left panel (65.3 % in the core and 34.7 % in the wing) have to be attributed to the beam divergence and scattering. This distribution is clearly identical to the profile in Fig. 3 obtained in the slit measurements (8 arcmin in Fig. 4 corresponds to 58 mm in Fig. 3 for the distance of 25 m from the main dish to the detectors).

In order to evaluate the image quality, the point spread function (PSF) and the encircled energy function (EEF) are calculated as are shown in the left and right panels of Fig. 6. The scattering component of the

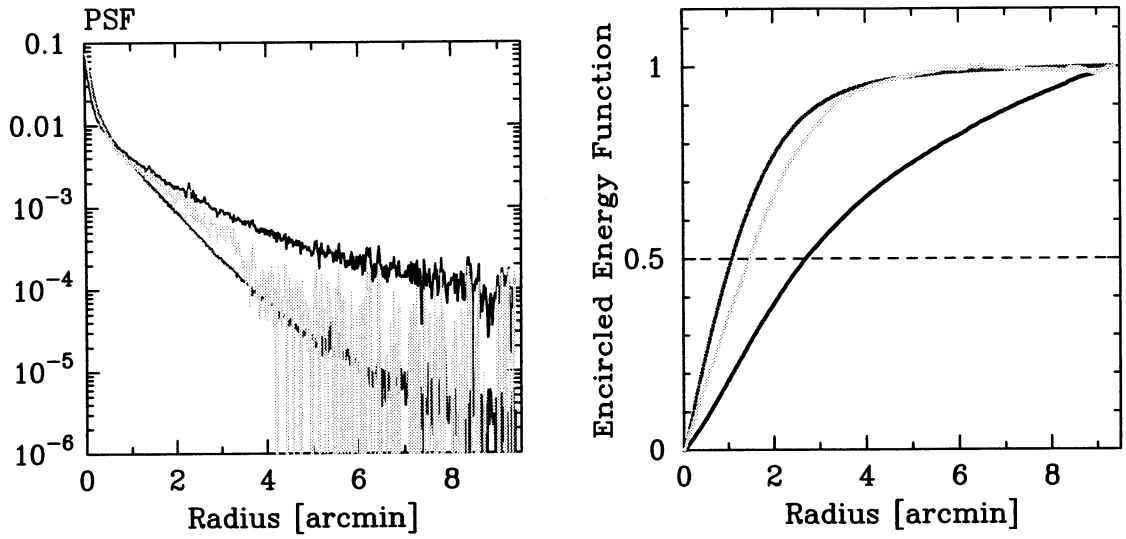

Figure 6. Measured Point Spred Function and Encircled Energy Functions of XRT.

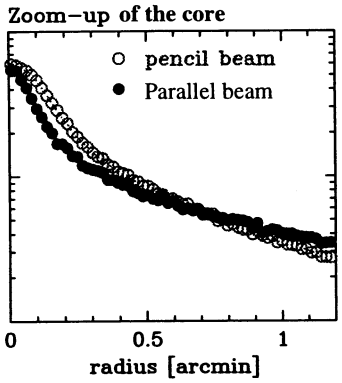

Figure 7. Measured core profile of focal plane images.

parallel beam gives much stronger tail in PSF and the dull increase in EEF. In order to remove the scattering component, we used the scattering profile in Fig. 5. It is assumed that the scattering profile in Y-Z plane is symmetrical around the peak with the radial distribution shown in Fig. 5 (left). If this tail is subtracted from the observed image, PSF and EEF are improved as are shown by the middle lines in two panels of Fig. 6. However, some more residuals are still seen between 0.5 and 3 arcmin, even with this correction. It is because the distribution in Fig. 5 is the profile of a point like source, while the real scattering component is the convolution of the horizontally elongated image seen in the right panel of Fig. 4 and the distribution of Fig, 5 (left). Therefore, more scattering is produced in the horizontal direction, which causes broader residual wings between 0.5 and 3 arcmin in the PSF and EEF.

Fig. 7 shows the enlarged plot of PSF with the parallel beam and the pencil beam. The peak of the core is sharper with the C-K parallel beam. As is mentioned in section 2, we expected similar divergence as the pencil beam. This estimation, however, is based on the X-ray spot size of 1 mm. The electron bombardment may not have a flat top distribution with sharp edges but could be some peak profile narrower than 1mm. It is now proven that the calibration with the present C-K parallel beam allow us to examine precise structure of the image core.

5. DISCUSSION AND SUMMARY

A soft X-ray parallel beam of 18 cm diameter is created by a normal incidence optics with multilayer coatings. It is installed at the X-ray beam facility of ISAS to calibrate X-ray telescopes. The focal point of the system is placed at the X-ray generator to provide a wide parallel beam of C-K X-rays at 4.4 nm. It works as a beam expander in visible light.

The beam flux is 10-15 counts/sec/cm2 and is strong enough to calibrate X-ray telescopes, because the collecting area of a quadrant is about 100 cm2 or more at this energy. Several minute observation will give us 45000 counts, which is enough to get statistical accuracy better than 1 %. The image shown in Fig. 4 is obtained in 5 minutes. It is a few tens of times faster than the pencil beam scaning.

However, the beam intensity has gradual distribution in horizontal direction. The minimu flux in the beam is 60 % of the peak flux. It puts more weight for -Y direction when a telescope is illuminated by the parallel beam.

The parallelism of the X-ray beam is about 20 arcsec or so at any points. However, the scattering component is quite high because of the diffraction due to the interfacial and surface roughness of about 0.3 nm. It causes strong scattering tail in the focal plane image of the telescope, which disturbs us to examine the PSF quantitatively. One thing I want to emphasize is that the sharp core is found with this parallel beam. It means this system is capable to look into the core images.

Our conclusion is that this system is very useful to examine otical alignment (on axis direction, image position, etc). It is much faster than pencil beam system and capable to see the core image, which can be easily disturbed by the diffraction in visible region. For the quantitaitve calibration, we need more careful treatment of the sattering component. It may be ideal to use the combination of this sytem with the ordinary pencil beam system for optical alignment and quantitative evaluation of X-ray telecopes, respectively.

ACKNOWLEDGMENTS

Authors want to present appreciation to Nikon for designing the reflector shape and multilayering the mirror surfaces. Authors also thank Dr. Hirohiko Honda(Shounan Institute of Technology), Dr. Takao Endoh (Mitsubishi Electric), Mr. Yasuhiro Hidaka (Nikon) and Mr. Kousuke Imamura (JSAT) for their contribution in the experiment and discussion. This research was supported in part by a grant-in-aid for scientific research on Specially Promoted Research contract 01702007 from the Ministry of Education, Science, Sports and Culture, Japan.

REFERENCES

1. Ryo Shibata, Manabu Ishida, Hideyo Kunieda, Takao Endo, Hirohiko Honda, Kazutami Misaki, Jun ' ichi Ishida, Kohsuke Imamura, Yasuhiro Hidaka, Masamichi Maeda, Yuzuru Tawara, Yasushi Ogasaka, Akihiro Furuzawa, Manabu Watanabe, Yuiichi Terashima, Tsutomu Yoshioka, Takashi Okajima, Koujun Yamashita, Peter J. Serlemitsos, Yang Soong, and Kai-Win Chan, *X-ray telescope on board Astro-E, -II. Ground based X-ray Charcterization*, Appl. Opt. Vol. 40, 3762-3783, 2001.
2. K. Misaki, Y. Hidaka, R. Shibata, K. Imamura, K. Itoh, H. Mori, M Ishida, H. Kunieda and K. Yamashita *Characterization of C-K Inverse-Telescope in the ISAS X-ray Beam Facility*, Proc. New Century of X-ray Astronomy, ASP Conf. Series Vol. 251,568-569, 2001.
3. H. Kunieda, S. Hayakawa, T. Hirano, T. Kii, F. Nagase, N. Sato, Y. Tawara, F. Makino, and K. Yamashita *Roughness Measurement of X-ray Mirror Surfaces*, Japanese Journal of Applied Phys. 25, No. 9. 1292-1299, 1986.
4. Hideyo Kunieda, Manabu Ishida, Takao Endo, Yasuhiro Hidaka, Hirohiko Honda, Kohsuke Imamura, Jun ' ichi Ishida, Masamichi Maeda, Kazutami Misaki, and Ryo Shibata, Akihiro Furuzawa, Kazutoshi Haga, Yasushi Ogasaka, Takashi Okajima, Yuzuru Tawara, Yuiichi Terashima, Manabu Watanabe, Koujun Yamashita, Tsutomu Yoshioka, Peter J. Serlemitsos, Yang Soong, and Kai-Win Chan *X-ray telescope on board Astro-E, - I. Optical Design and Fabrication of Thin Foil Mirrors*, Appl. Opt. Vol. 40, 553-564 2001.

An X-ray Calibration Facility with a Dynamical Pencil Beam for the Post Astro-E2 Telescopes

Yoshitomo MAEDA[a], Akiharu ITOH[a], Kei ITOH[a], Hideyo KUNIEDA[a],
Yoshito HABA[a], Akira HAYAKAWA[b], Ryo IIZUKA[a], Chiaki INOUE[b],
Manabu ISHIDA[b], Kazutami MISAKI[a], Hideyuki MORI[a], Ryo SHIBATA[a]

[a]Institute of Space and Astronautical Science, 3-1-1 Yoshinodai, Sagamihara, 229-8510, Japan
[b]Tokyo Metropolitan University, 1-1 Minamiosawa, Hachioji, Tokyo, 192-0397, Japan

ABSTRACT

We report a new calibration system for large size X-ray optics at ISAS. We adapted a "dynamical" pencil beam collimated from an X-ray generator, the maximum voltage for which is 50 kV. By combining two stage systems for the X-ray generator and a collimator, the pencil beam dynamically sweeps across a circular region of a telescope with the radius of 60 cm at maximum. In this case, the X-ray telescope and the focal plane detector are both statically fixed. A 4.4 m long rail for detector stage and two positions of the telescope stage provide focal lengths from 4.5 to 12 m, while the previous system can accommodate 4.5 or 4.75 m focal length. The preliminary performance of this system is summarized in this paper. For the post-Astro-E2 satellite, a hard X-ray multi-layer supermirror with an unprecedented sensitivity up to 80 keV (Tawara et al. 2002) is strongly expected. This beam facility is of importance because the hard X-ray mirrors always require a long focal length of 8-12 m due to the small reflection angle (about 0.3 degree). Focal length and diameter of future telescopes are always decided by the boundary conditions of the mission at the last moment of the design freeze. Our new X-ray beam facility is designed to match with any kind of X-ray telescope parameters.

Keywords: X-ray, Optics, Calibration

1. INTRODUCTION

New X-ray Telescope (NeXT) is a post Astro-E2 X-ray mission, possibly launched in FY 2009. One of the key instrument of NeXT is a hard X-ray supermirror with an unprecedented sensitivity up to 80 keV (Tawara et al. 2002). The mirror consists of Wolter-I-type reflecting optics like ordinary soft X-ray telescope but with reflecting surface coated with multi-layers. By grading periodic length of multi-layer into depth direction, wide band X-rays up to 80 keV can satisfy Bragg's condition at the same incident angle. However, the incident angle can be allowed by 0.3–0.4 degree, so that the focal plane length should be at least about eight meter long to archive the effective area of an order of 100 cm^2. In fact, "InFOCμs", the first balloon experiment loaded with a supermirror telescope, has a focal length of 8 meter long (Okajima et al. 2002).

The 30 m X-ray beam line at the Institute of Space and Astronautical Science (ISAS) is designed and built to calibrate the X-ray telescopes for the ASCA and Astro-E/E2 satellites (Kunieda et al. 1993; Serlemitsos et al. 1995; Shibata et al. 2001). In order to minimize the measurement system, a pencil beam line is introduced: illuminating and scanning the entire aperture of X-ray instruments with a pencil beam of $\sim$ 10 arcsec parallelism

Y. Maeda: E-mail: ymaeda@astro.isas.ac.jp, Telephone: +81-42-759-8150

is provided by a 1.5 mmϕ pinhole placed 30 m away from the X-ray source. Since the X-ray beam fixed, mirrors and detectors must be synchronously translated, as a whole. The system has advantages that we can directly measure the mirror response to the parallel X-ray beam in such a short beam and can concentrate the beam to a narrow enough width, even in a single reflector, to check the quality of the reflectors after fabrication. In fact, response function of X-ray telescope for Astro-E was directly measured using this system (Misaki et al. 2002). However, the system can accommodate 4.75 m focal length and 40 cmϕ telescope at maximum, so that it is impossible to focus the supermirror telescope onboard NeXT. In order to realize a pencil beam that can illuminate the telescope, we installed a new system at ISAS which co-exists the present system. We here report the design and preliminary performance of the system.

2. SYSTEM

2.1. ISAS X-ray Beam Facility

The ISAS beam facility was first built in 1991. A schematic view of the standard configuration is shown in the top panel of Fig. 1. The system is composed of an X-ray generator and measured chambers jointed by a 30 m long evacuated tube. The details of this system are given in Kunieda et al. (1993) and Shibata et al. (2001). We modified the system for the NeXT mission in 2002. Three large size chambers manufactured by Osaka Vacuum, Ltd, which accommodate the movable X-ray generator, movable collimator and X-ray telescope, were newly inserted between the inverse telescope chamber and the movable slit (Fig. 1). The three chambers are connected each other by a vacuum tube of 650 mmϕ. The distance between the movable generator and collimator is 10 m long.

By combining the previous equipments with newly installed ones, we can provide at least three configurations of calibration system for X-ray telescopes, which are summarized in Fig. 1. The configuration C was designed for NeXT, which we report here. For the 30 m beam (Configuration A) and inverse telescope (B), one can refer to Shibata et al. (2002) and Kunieda et al. (2002).

2.2. X-ray Generator

The X-ray generator adopts a liquid cooled packaged X-ray tube Oxford 5020LC while the overall system is developed by Rigaku Co.. Oxford 5020LC features an electron gun assembly packaged in a stainless steel lead lined tube. The tube is filled with a oil cooled by a cold water. W and Cu anode targets are currently available at ISAS. Their primary emission lines appears at 8.04 keV (Kα), and 8.40 keV (Lα), respectively. The maximum bias voltage and anode current are 50 kV and 2 mA. The exit window is 127μm Be. Oxford 5020LC is surrounded by an aluminum housing box under the atmospheric pressure. An X-ray shutter module is mounted between the exit window and a 400μm Be window sealed from the vacuum chamber. The total weight of the box including the X-ray tube is 15 kg while the size is as small as 200 mm (W) $\times$ 150 mm (D) $\times$ 300 mm (H).

An additional brass buffle with the length of 154 mm is attached at the Be window of the box. At the end of the buffle, a 1 mmϕ pinhole is mounted to collimate the X-ray beam coursely.

2.3. Collimator and Filters

In order to achieve a high parallelism, we collimate X-ray beam using a circular pin-hole located 10 m away from the X-ray generator (Fig. 1). Three pin-holes with 0.2, 0.5 or 1.0 mm were punched on 1 mm thick Ta sheet by Machine shop of the School of Science, Nagoya University. By manually sliding the Ta sheet, we can

Table 1. Performance of the new system.

Movable X-ray generator	
Bias voltage	4–50 kV
Anode current	0–2 mA
Electron spot size	0.4 mm×0.9 mm[a]
Window thickness	Be 527 μm
	Air 55.6 mm
Anode Target	W, Cu
Vacuum tube	
Length	10 m
Diameter	650 cm
Pressure	$< 10^{-5}$ Torr
Collimator	
Material	Ta (1mm thickness)
Pin hole	0.2, 0.5, 1.0 mm ϕ
X-ray beam characteristics	
X-ray energy	4–50 keV
Beam divergence	$17'' \times 27''$[a,b]

a: Preliminary results (FWZI).
b: 0.5 mmϕ pin hole

Table 2. Operation parameters of the mechanical stages.

Axis	Pulse Weight [/pulse]	Stroke
X-ray generator chamber:		
Θ_Z	0.001 °	±1 °
Y	0.002 mm	±300 mm
Z	0.0002 mm	±300 mm
Collimator chamber:		
Y	0.002 mm	±300 mm
Z	0.0002 mm	±300 mm
Mirror chamber:		
Θ_X	0.00002°	360°
Θ_Y	0.00002°	±3°
Θ_Z	0.00002°	±5°
Detector chamber:		
Rail	–	4400 mm
X	0.002 mm	±50 mm
Y	0.004 mm	±150 mm
Z	0.002 mm	±50 mm

Monimum and maximum pulse rates are 1,000 and 10,000 pulse s^{-1}.

pick one from the three pin-holes. An energy filter can be put either on the X-ray generator or the collimator chamber.

2.4. Detectors

Three kinds of focal plane detectors, the proportional counter the CdZnTe detector and the charge-coupled device (CCD), are currently available in the ISAS X-ray beam facility. (1) Proportional Counter (PC): PC available in the ISAS X-ray beam facility is the gas-flow type. We use so-called P10 gas (90 % argon and 10 % methane) at 1 atm for the flowing gas. The entrance window is a circle with 12 mmϕ covered with the aluminum-coated Mylar film with a thickness of 15 μm. The depth of the gas measured from the entrance window is 22 mm. (2) CdZnTe (Amptek XR-100T-CZT): CZT has medium energy resolution ($\sim$ 5 % @Cu-K_α; 8.04 keV), but has no imaging capability. The detector size is 5 × 5 [mm^2] and detector thickness is 2 [mm], which achieve the 65 % detection efficiency at Cu-K_α. (3) Backside-illuminated CCD (SITe): It has a 1024 × 1024 array of pixels, and the size of each pixel is 24 [μm]. The data from the CCD is taken with the frame mode, therefore we can use either the flux or photon-counting mode.

2.5. Stages

In order to simulate parallel X-rays from celestial objects, we introduced mechanical stages both in the X-ray generator and the collimator chambers (Fig. 3). The detailed parameters are given in Tab. 2. Two linear stages

along the y and z axes were inserted in the X-ray generator and collimator chambers. The stroke is 600 mm long each. We carefully aligned and tuned the stages, so that the accuracy of better than 60μm within 600 mm stroke is archived. The parallelism of each axis between the generator and collimator stages was then found to be better than $\sim$1 arcmin. By synchronously translating the stages, the parallelism of $\lesssim 5''$ is archived between the two stages.

Rolling of y stage and yawing of y and z stages of X-ray generator were measured to be smaller than $\sim 30''$ within 600 mm stroke while the yawing of z stage has not been measured yet. The rolling or yawing of $30''$ at the generator chamber shakes the beam position by 1.5 mm at the collimator chamber, which is about an order of smaller than the flat peak of the beam (see section 3).

Another stage systems were also installed in the mirror and detector chambers to simulate a telescope in space (Fig. 3). In the mirror chamber, we have triaxial rotational stages actuated by stepping motors. A telescope with 60 cm at maximum can be installed on the stages.

For the chamber accommodating the focal plane detector, we use both the sample and the detector chambers in the previous system. We can choose the course focal length by operating the 4.4 m long rail manually. Three dimensional linear stages (X, Y, Z), translating focal plane detectors, move along the rail. The fine focal position can be adjusted by the three dimensional stages.

By combining the stage systems, the pencil beam dynamically sweeps across a circular region of a telescope with the radius of 60 cm at maximum. The X-ray telescope and the focal plane detector are both statically fixed. Two positions of the mirror chamber provide focal lengths from 4.5 to 12 m. In addition, the other θ stage is installed in the X-ray generator chamber, so that we can measure the off-axis image by changing the beam angle. All the stages are developed by Kohzu Precision Co., Ltd.

3. DYNAMICAL X-RAY PENCIL BEAM

3.1. Energy Spectra

In order to take a beam spectrum, we temporally mounted the CdZnTe detector on the collimator stage. The spectrum for the maximum voltage of 50 keV is shown in Fig. 4. We confirmed the spectrum shows W-L complex lines and bremsstrung continuum with a cut-off at 50 keV. In addition, a low-energy cut-off at $\sim$ 5 keV was detected, which is identified to the absorption at the two Be windows (127 and 400μm) and the atmospheric shutter module (56 mm). The total count rate of 1×10^4 counts s^{-1} was obtained for the maximum current 2 mA with the pin-hole diameter 0.2 mmϕ^{-1}. The counts identified to W-Lα, Lβ and Lγ are 24%, 22% and 6% of the total.

Fig. 4 shows the beam spectrum filtered by a Cu 30μm filter, the K edge of which appears at 8.9 keV. The bias voltage was set to 20 kV to reduce the continuum flux in the high energy band. The count rate for 2 mA with the 0.5 mmϕ pinhole was 220 counts s^{-1}, about 3/4 of which are identified with W-Lα line. By excluding the counts above 9 keV, we can exclude most of the continuum in the 9–20 keV band. Consequently, the purity of W-Lα reaches $\sim$90% but low energy continuum in 4 $\sim$ 8 keV still remains in the spectrum. Note that this method can be applied if we take the spectrum with PC or CCD in the photon counting mode.

3.2. Beam Pattern

The X-rays radiated from the generator show a beam pattern of an elliptical shape elongated to Z axis: 13 mm $\times$ 33 mm (FWHM) at the distance of the collimator chamber. The beam within $\sim$1 cm from the peak remains 90% or higher level of the peak flux.

In addition, X-rays extended over the entire chamber, possibly due to the scattering at the buffle, was detected. The flux of the extended X-rays is about three or four orders of magnitude lower than the beam peak. In order to block the extended X-rays at the collimator chamber, we currently cover the pin-hole with a 2 mm lead sheet of 40 cm$\times$ 40cm. With this blocking sheet, no significant extended X-rays should illuminate the quadrant telescope with an aperture of $\lesssim$40 cm.

The beam pattern collimated by the pinhole was obtained by a CCD camera placed at the focal plane of Astro-E2 XRT (Fig 5). The pin hole diameter is 0.5 mm. The beam shows the elliptical shape elongated to z direction: 1.2 and 1.6 mm on y and z axes (FWZI), respectively. The elongation can be explained if the projected electron impact area of the X-ray tube is $\sim$ 0.4 mm and $\sim$ 0.9 mm on y and z axis, respectively. The beam divergence (FWZI) can be then derived as 17" and 27", respectively.

3.3. Raster Scan

In order to demonstrate the raster scan by the dynamical pencil beam, we installed the spare quadrant of the Astro E2 telescope (XRT-I) into the mirror chamber. The principle of the raster scan is summarized in Shibata et al. 2002. PC and CCD were mounted on the detector stage and were used to measure an effective area and the image quality. The scan pitch along the Z direction was 5 mm height while the scan speed of Y stage was 4 mm s^{-1}. We used the W-Lα line at 8.40 keV filtered by 30μm Cu. The 0.5 mmϕ pin-hole was selected, so that the beam paralelism for the raster scan is dominated by the beam divergence: 17" and 27" on y and z axis (FWZI), respectively.

Fig. 6 shows the focal plane image on the boresight were successfully taken by the CCD camera. We found the half power diameter was 2.0 arcmin which is consistent with that measured by the previous system (Shibata et al. 2002). The effective area was derived as 64 cm^{-2}, which is higher by $\sim$10–20%. The effective area of the Astro-E2 XRT is known to have large energy dependence ($\sim$81 cm^{-2} at 4.51 keV, Ti-Kα and $\sim$43 cm^{-2} at 9.44 keV Pt-Lα; Shibata et al. 2002), so that the overestimate of the effective area may be due to contamination of the low-energy photons.

4. CONCLUSION AND SUMMARY

A new system by a dynamical pencil beam joined in the ISAS beamline facility. The unique feature, the movable X-ray generator and collimator, allows us to calibrate supermirror telescopes onboard NeXT (an aperture of 40–60 cmϕ and a focal length of 8–12 m). The beam paralelism for the 0.5 mmϕ collimator is 17" and 27" on y and z axis (FWZI), respectively.

There are, however, several points to be improved for future measurements. (1) Fully automated operation must be established for general users. (2) Extended X-rays, possibly scattered at the generator exit, illuminate the mirror chamber unless the long buffle is installed on the generator stage. Since the long buffle currently interferes with the upper wall of the X-ray generator chamber, the buffle must be replaced to a shorter one. (3) The window thickness of the generator exit should be reduced to save the soft X rays below 4 keV. (4) A kind of monochromator or photon counting detector with a good energy resolution will be installed to measure the effective area precisely. (5) Beam stability will be determined by a long-term monitor.

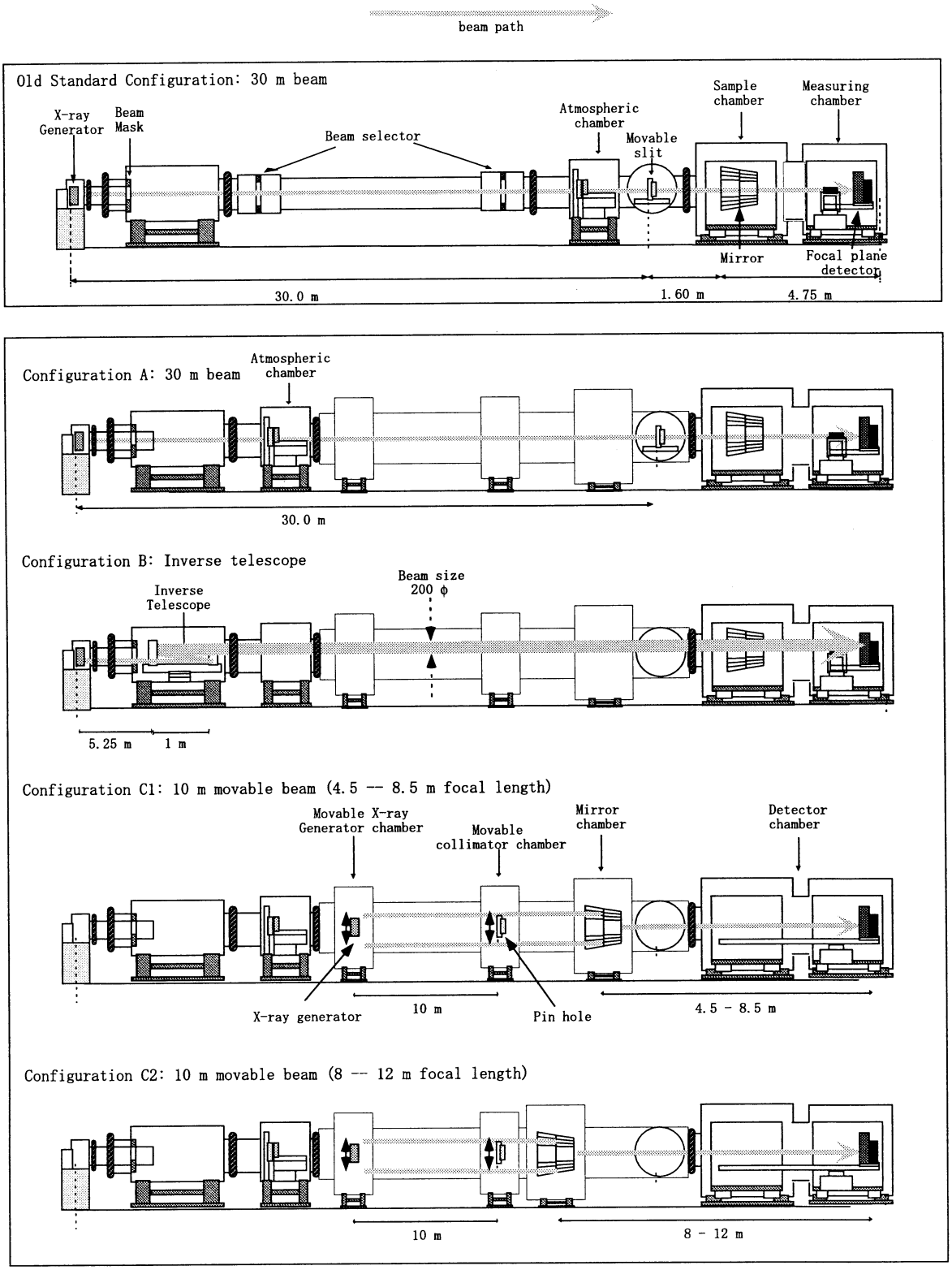

Figure 1. Schematic view of the ISAS X-ray beam line. The old/previous system was shown in the top panel while the four different configurations for the new system were shown in the lower panels.

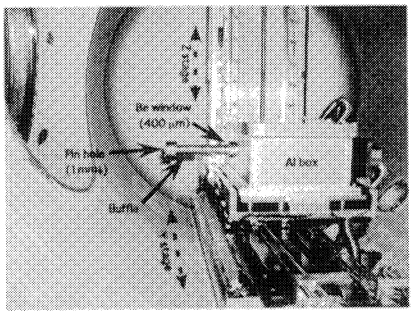

Figure 2. Picture of the X-ray generator. The X-ray tube Oxford 5020LC and the shutter module are equipped in the aluminum box under the atmospheric pressure.

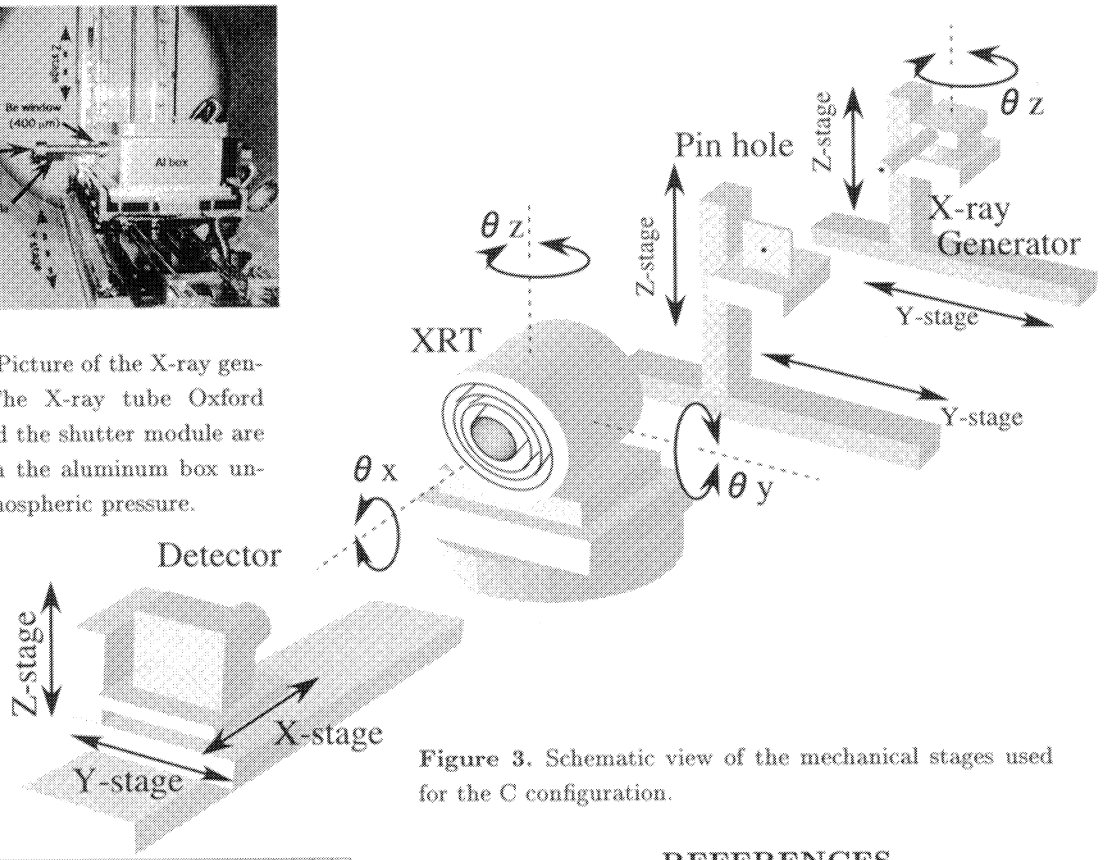

Figure 3. Schematic view of the mechanical stages used for the C configuration.

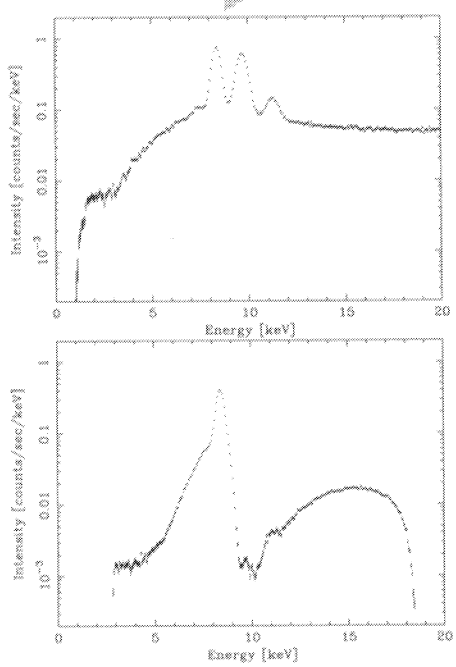

Figure 4. Spectra of X-ray beam from W target without (top) and with (bottom) a Cu filter. The voltage/current of the X-ray generator is 50kV/0.1mA, and 20kV/1mA, respectively

REFERENCES

1. Kunieda H. et al., "Thirty-Meter X-Ray Pencil Beam Line at the Institute of Space and Astronautical Science", JJAP 32, 4805–4813 (1993)
2. Kunieda, H. et al., "Normal incidence multilayer telescope for soft X-ray beam expander", SPIE in this volume (2002)
3. Misaki, K. et al., "Error budgets for the image degradation of X-ray telescope onboard Astro-E", SPIE in this volume (2002)
4. Okajima et al., "Characterization of the supermirror hard-X-ray telescope for the InFOCuS balloon experiment", Applied Optics, Vol. 41, No. 25 in press (2002)
5. Serlemitsos P. J. et al., "The X-ray Telescope on board ASCA", Pub. Astr. Soc. Japan 47, 105–114 (1995)
6. Shibata, R. et al. 2001, Applied Optics, 40, 3762
7. Tawara, Y., et al. "Broad Band X-ray Imaging mission *NeXT*", SPIE in this volume (2002)

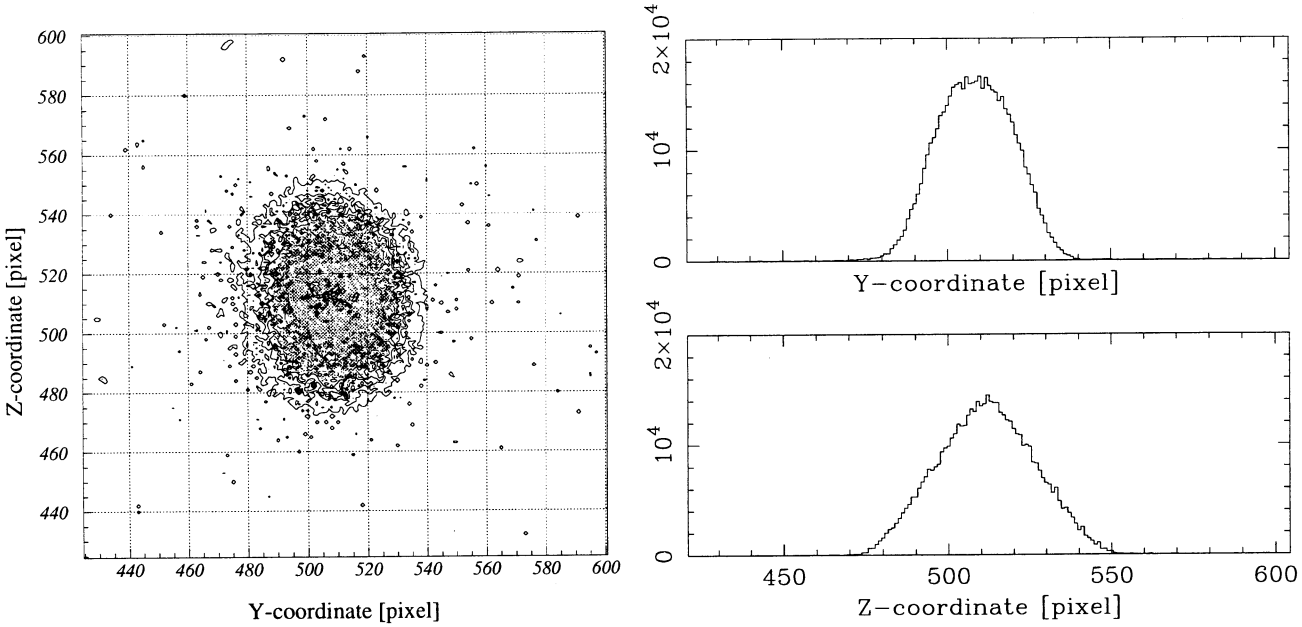

Figure 5. CCD image of the collimated beam by the 0.5 mmϕ pin hole (left) and the profiles projected onto (upper right) y-axis and (lower right) z-axis. The image (1 pixel= 24μm) is viewed from the side of X-ray generator.

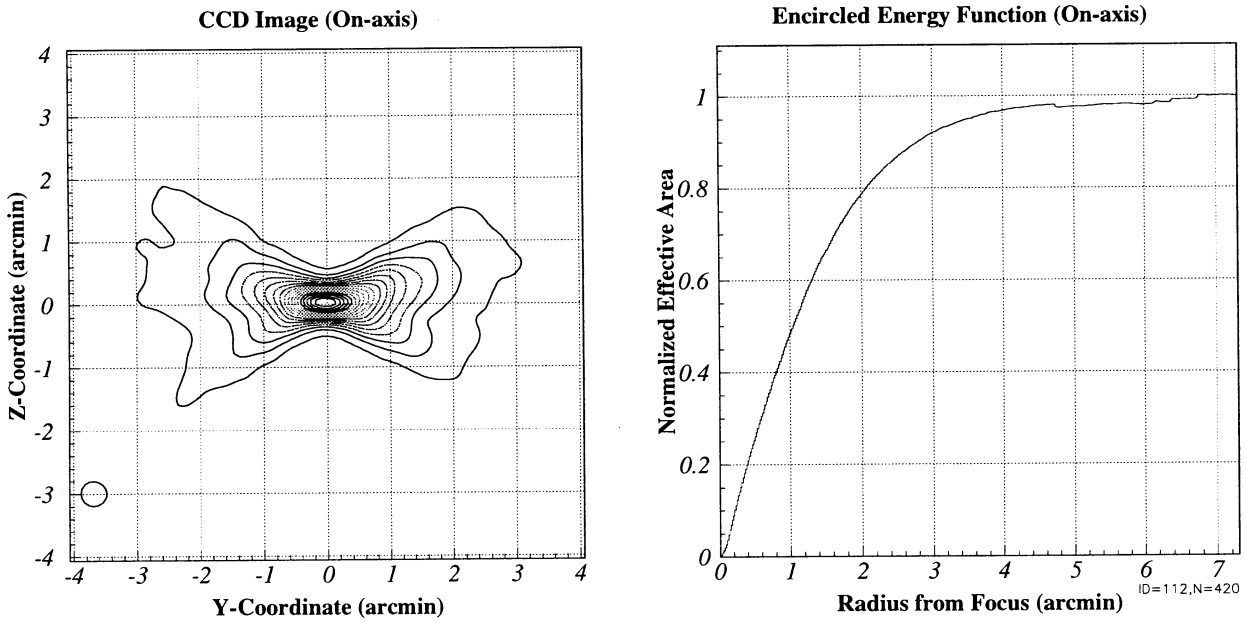

Figure 6. Boresight look-down smoothed image (left panel) and encircled energy finction (EEF: right) of Astro-E2 XRT-I measured at W-Lα (8.40 keV).

X-ray Characterization of Capillary System

Yoshito Haba[a] Ryo Iizuka[a] Akira Hayakawa[b]
Kazutami Misaki[a] Ryo Shibata[a] Kei Itoh[a] Hideyuki Mori[a]
Yoshitomo Maeda[a] Manabu Ishida[b] and Hideyo Kunieda[a]

[a]Institute of Space and Astronautical Science,
3-1-1, Yoshinodai, Sagamihara, 229-8510, Japan
[b]Tokyo Metropolitan University,
1-1, Minamiosawa, Hachioji, Tokyo, 192-0397, Japan

ABSTRACT

X-ray characterization measurements of capillary (X-ray Optical Systems Inc) were carried out at the Institute of Space and Astronautical Science (Japan) X-ray beam facility. Since capillary system has a capability of collecting x-rays effectively by the small angle reflections in the narrow tubes, it is expected to apply it for the observation of astronomical x-ray objects.

The depth of focus on the on-axis is 6 mm, and the image size at the focal plane is 0.4 mm (FWHM) with Cu-K_α. By using continuum x-ray (2 to 15 keV) beam, the on-axis efficiency was evaluated to be $\sim$ 20 % (17.7 %, 24.1 % at 4.51 keV and 8.04 keV, respectively). The efficiency decreases gradually toward low energy range ($<$ 6.0 keV), this could be explained by the absorption effect of Si which is one of the constituent element of capillary tubes (SiO_2). The field of view is defined as the off-axis angle at which the efficiency becomes half of the on-axis value. The diameter of the field of view was $\sim$ 22', 19' at 4.51 keV and 8.04 keV, respectively. Capillary has no imaging capability, in other words, the light-concentrating direction is independent from the incident angle of x-ray beam. When the x-ray incident angle varies from -15' to +15', the focused images are distributed within $\sim$ 3'.

From our measurements, we could confirm the performance of capillary and its potential for astronomical applications.

Keywords: X-ray, Optics, Capillary

1. INTRODUCTION

Capillary X-ray optics are composed of bundles of tiny glass tubes. One bundle of capillary tubes is called a polycapillary fiber. Typical diameter of glass tube and fiber are 20 μm and 500 μm, respectively. Thousands of such fibers can be strung through metal grids to form a multi-fiber lens. Schematic view is presented in figure 1 (right panel).

X-rays can be guided by total external reflection on the inner surfaces of the hollow tubes, hence along the curvature of capillary tubes, parallel X-ray beam in a tube is bent toward a focal point. In X-ray astronomy, this property is useful to minimize the detector size at focal plane which improves the signal to noise ratio, since detector background is proportional to the detector (pixel) size.

To verify the utility of capillary optics in X-rays, we measured the X-ray characteristics at different energies and incident angles. Figure 1 shows the capillary (X-ray Optical Systems Inc) we measured. The size of the incident window is 10.8 $\times$ 10.8 [mm^2], and is covered with the Be (38 μm) foil (same foil also covers the capillary exit window). The body length along the optical axis is 64.5 [mm].

Y. Haba: E-mail: haba@astro.isas.ac.jp, Telephone: +81-42-759-8150

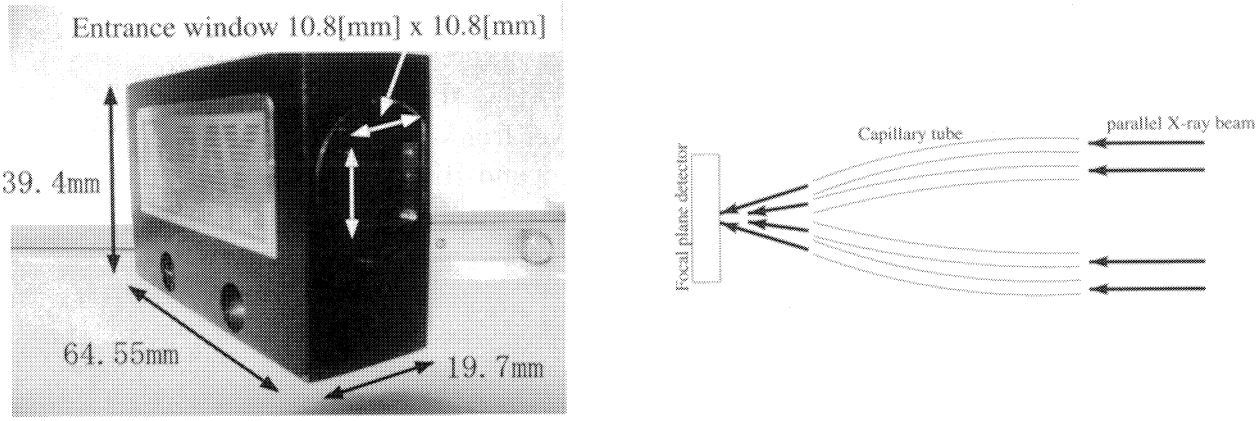

Figure 1. Capillary developed by X-ray Optical Inc (left panel). The schematic view of capillary (right panel).

2. MEASUREMENT SYSTEMS

2.1. X-ray Beam Line at Institute of Space and Astronautical Science (ISAS)

Figure 2 shows a schematic view of the X-ray beam line at ISAS. To achieve a sufficient parallel X-ray beam, X-ray generator is placed far away from capillary, and the beam is collimated by movable slit which is located 30 [m] away from X-ray generator. Since capillary is located 5.4 [m] away from movable slit and we set slit size at 1×1 [mm^2] or 10×10 [mm^2] throughout our measurements, the full diverging angles of X-ray beam are $\sim$14" and $\sim$1.3', respectively.

2.2. X-ray Generator

The X-ray generator (RIGAKU RU-200) has a water-cooled rotary-type X-ray target. Seed electrons are emitted from a thermally heated W filament. The electrons are accelerated by a high bias voltage (50-60 kV) supplied between the filament and the metal rotary target, and they hit the target. The effective spot size is 1×1 [mm^2]. The electrons lose their kinetic energy in the target by bremsstrahlung, ionization, excitation of the characteristic X-ray emission, and heat. We used Ti and Cu as the target metal, whose emission lines appear at 4.51 [keV] and 8.04 [keV] respectively.

2.3. Metal Filters

Because of its large cross section and high fluorescence yield, we usually use the K_α transition of the target metal as the source of the monochromatic X-ray. To reduce the number of continuum X-rays caused by the bremsstrahlung emission, we filter the X-ray beam with a thin metal film.

Since the energy of the K_α line is always slightly lower than the absorption threshold energy, it is available to use the filter with the same metal as the target. So we used a Ti filter with a thickness of 50 [μm] for Ti target. In use of Cu target, however, we use Ni (40 [μm]) filter because the K-edge of Ni falls between the K_α and $K\beta$ lines of Cu and hence more monochromatic beam is expected than those with a Cu filter. The fraction of line photons in the spectrum is 91 %, 86 % for Ti and Cu, respectively.

2.4. Focal-Plane Detectors

We used two kinds of focal-plane detectors, the charge-coupled device (CCD) and the semiconductor (CdZnTe) detector (hereafter CZT) in our measurements.

We adopt a backside-illuminated CCD developed by SITe as the detector. It has a 1024×1024 array of pixels, and the size of each pixel is 24 [μm]. In our measurement we use the CCD in the flux mode not in the photon-counting mode that is usually used in in-orbit observations of X-ray astronomy satellites. In the flux mode, we just count the number of electrons stored in each pixel during an exposure, and the CCD can cope

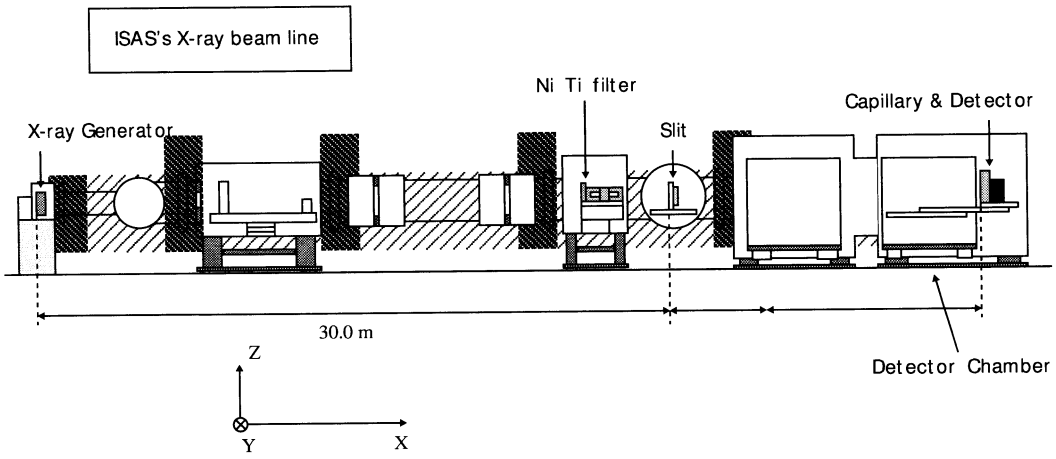

Figure 2. Schematic view of the ISAS's X-ray beam line; Capillary and detector is installed in the detector chamber.

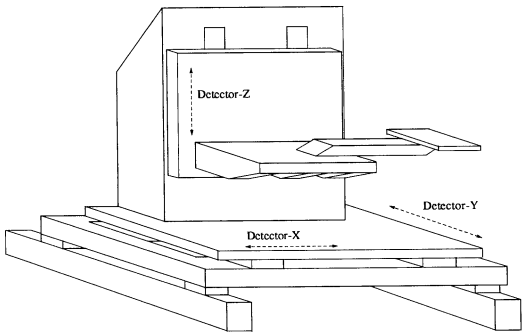

Figure 3. Mechanical stages installed in the detector chamber. Capillary stage (see figure 4) are mounted on the 'Detector mounting table'.

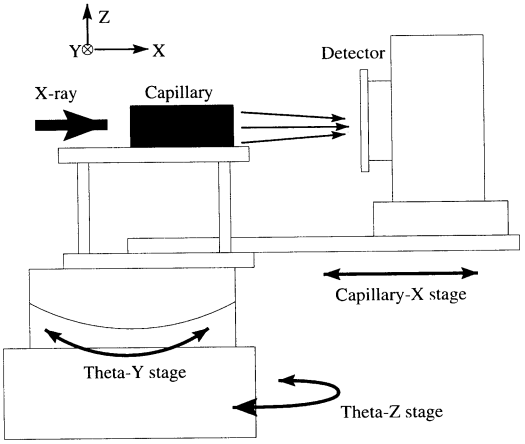

Figure 4. Capillary stages has two rotational stages (Theta-Y, Theta-Z) and one linear stage (Capillary-X).

with considerably higher X-ray flux than in the photon-counting mode. Since information on the incident X-ray energy is completely lost in the flux mode, a highly monochromatic incident beam is required.

XR-100T-CZT developed by Amptek is used to measure energy response of the capillary. CZT has medium energy resolution ($\sim$ 5 % @Cu-K$_\alpha$; 8.04 keV), but has no imaging capability. The detector size is 5 $\times$ 5 [mm^2] and detector thickness is 2 [mm], which achieves the 65 % detection efficiency at Cu-K$_\alpha$.

2.5. Movable Stage

Figure 3 and 4 show several mechanical stages installed in the detector chamber. Three linear stages referred to as Detector-X, Detector-Y and Detector-Z can be moved along the x, y and z axes by stepping motors. In addition, two rotational stages (Theta-Y, Theta-Z) and one linear stages (Capillary-X) are installed on detector mounting table (see figure 3). The Theta-Y and Theta-Z stages are used for off-axis measurements and the Capillary-X stage is used for determination of the focal length.

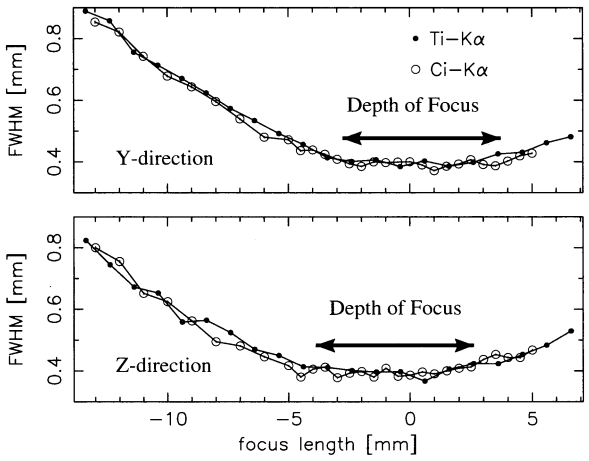

Figure 5. The variation of image size depending on the distance from capillary to detector. The size of X-ray beam is 10 × 10 [mm^2] and energy of beam is 8.04 [keV] (Cu-K$_\alpha$).

3. RESULTS

3.1. Determination of Optical Axis and Focal Length

The optical axis is the maximum transmission axis of the capillary. By moving Detector-Y, Detector-Z, Theta-Y and Theta-Z stages, we could find the best alignment of the optical axis when the number of photon transmitted from capillary is maximum.

In this measurement, we used CCD as a detector and we found that the location of focused image on CCD was slightly different when the position of incident X-ray beam against capillary window is different. This means that the focal length is somewhat different from true value. To obtain the true focal length, we measured the size of focused image when the distance from capillary to detector was varying. Figure 5 shows the relationship between focal length and FWHM of image. The minimum image size of 0.4 [mm] (FWHM) is obtained at the focal distance of 106.8 [mm]. The image size does not become 10 % larger at the focal length within 6 [mm] from the best focus position.

3.2. transmission Coefficient

We measure the transmission coefficient of capillary when Cu-K$_\alpha$ or Ti-K$_\alpha$ X-rays were injected along the optical axis of capillary. The efficiency is defined as ratio of the number of photons transmitted from capillary to that of direct X-ray beam. We adopted 1 × 1 [mm^2] beam to illuminate the center of the capillary window, on the other hand 10 × 10 [mm^2] beam to cover the total capillary window. Table 1 shows the measurement results for each target and different X-ray beam size. It is seen that the transmission coefficient is decreasing as X-ray beam size becomes bigger. So we measure the uniformity of transmission coefficiency by scanning the total window area with 1 × 1 [mm^2] beam. Figure 6 shows the efficiency map in 9 × 9 [mm^2] at Cu-K$_\alpha$ (8.04 keV). We can see the efficiency decrease as beam position shifts outward. This tendency probably reflects the variation of curvature of capillary tube, namely, the number of reflections in a capillary tube increases for outer tubes than inner ones. Here we define the flux amplification of capillary as the ratio of flux transmitted from capillary to flux illuminating the entrance window. Since focused image size is 0.4 [mm] (FWHM) and the size of window is 9 × 9 [mm^2], flux amplification is evaluated to be 155 and 110 at Cu-K$_\alpha$ and Ti-K$_\alpha$, respectively.

Table 1 also shows the energy dependence of transmission coefficient. To investigate this dependence in more detail, we used the CZT as a focal plane detector to obtain the energy spectrum from 2 keV to 13 keV with continuum X-ray emission (bremsstrahlung). Figure 7 shows the energy dependence of transmission coefficient. We expect that the transmission of low energy photons is higher than that of high energy photons, because the reflectivity is decreasing when incident photon energy is higher. However the transmission coefficient is

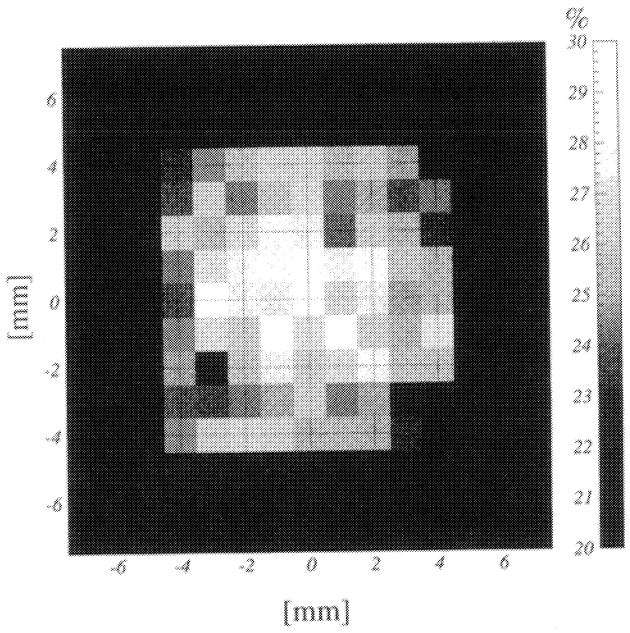

Figure 6. Transmission coefficient map; The beam size of X-ray is 1 × 1 [mm^2] and energy of beam is 8.04 [keV] (Cu-K$_\alpha$).

decreasing as incident photon energy is lower. This tendency is not explained even we take account of the absorption effect of 76 [μm] (entrance + exit) Be window (see figure 7). This inconsistency is discussed in section 4.

Table 1. The transmission coefficiency of each energy and beam size

X-ray energy [keV]	X-ray beam size [mm^2]	Transmission coefficiency [%]
8.04 (Cu-K$_\alpha$)	1 × 1	28.1 ± 0.7
	10 × 10	24.1 ± 1.4
4.51 (Ti-K$_\alpha$)	1 × 1	20.8 ± 0.5
	10 × 10	17.7 ± 1.5

3.3. Field of View

The field of view is defined as the off-axis angle at which the efficiency becomes half of the on-axis value. To determine the field of view of capillary, we first measured the efficiency depending on off-axis angles with 10 × 10 [mm^2] monochromatic X-ray beam (Cu-K$_\alpha$ and Ti-K$_\alpha$) by the CCD as a focal plane detector. We realize configurations of various off-axis angles with Theta-Y (θ_y) and Theta-Z (θ_z) stage. Here $\theta_y = \theta_z = 0$ implies the optical axis of capillary. The measurements were performed at $-30' \leq \theta_y \leq +30'$ with $\theta_z = 0'$ and $-30' \leq \theta_z \leq +30'$ with $\theta_y = 0'$. Figure 8 shows the measured results. The angular response in two directions is very similar to each other and is symmetry around the optical axis. The diameter of the field of view is 19', 22' for Cu-K$_\alpha$ and Ti-K$_\alpha$, respectively. Capillary has no imaging capability, in other words, the light-concentrating direction is independent from the incident angle of x-ray beam. Figure 9 shows the distribution of the light-

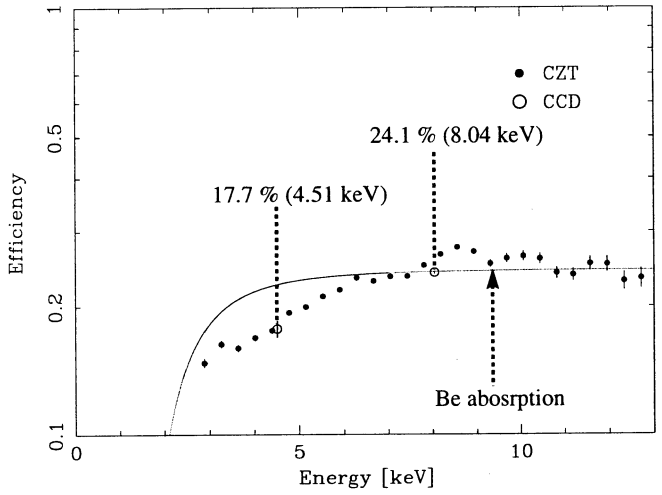

Figure 7. Transmission coefficient depending on incident photon energy; The beam size of X-ray is 10 × 10 [mm^2]

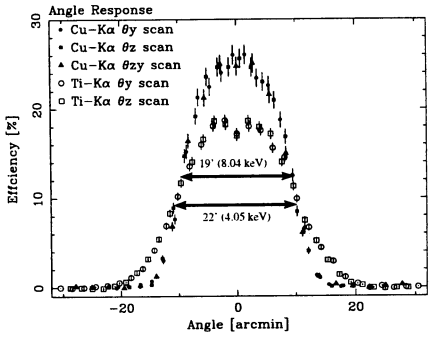

Figure 8. Angular response of capillary. The incident energy is Cu-K_α (filled marker) and Ti-K_α (open marker). The abscissa indicates an off-axis angle θ_y (circle) or θ_z (square).

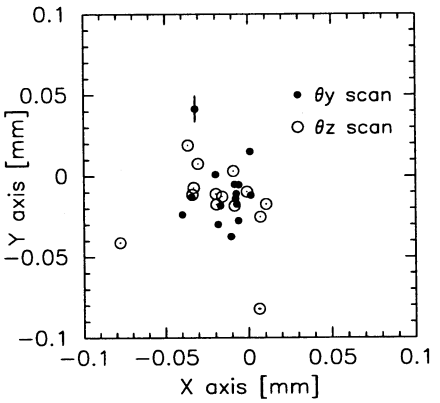

Figure 9. The distribution of the light-concentrating direction. The image at optical axis is focused on X axis = Z axis = 0. Data points are represent the position of focused image on the detector when θ_y (filled circle) or θ_z (open circle) varies from -15' to +15', respectively.

concentrating direction when θ_y and θ_z vary from -15' to +15'. The light-concentrating direction of each off-axis is distributed within $\sim$ 0.1 [mm] on the focal plane detector, which is corresponding to $\sim$ 3'.

In order to investigate the energy dependence of field of view, we performed same measurement with CZT detector with the continuum X-ray beam. Figure 10 shows the relationship between incident photon energy and the field of view. It is clearly seen that the field of view increases gradually toward low energy range, though below $\sim$ 7 keV the field of view is nearly constant or flattened.

4. DISCUSSION

As described in section 3.2, transmission coefficient is significantly reduced toward low energy range. It is difficult to explain this tendency by the absorption effect of Be foil which covers the entrance and exit windows

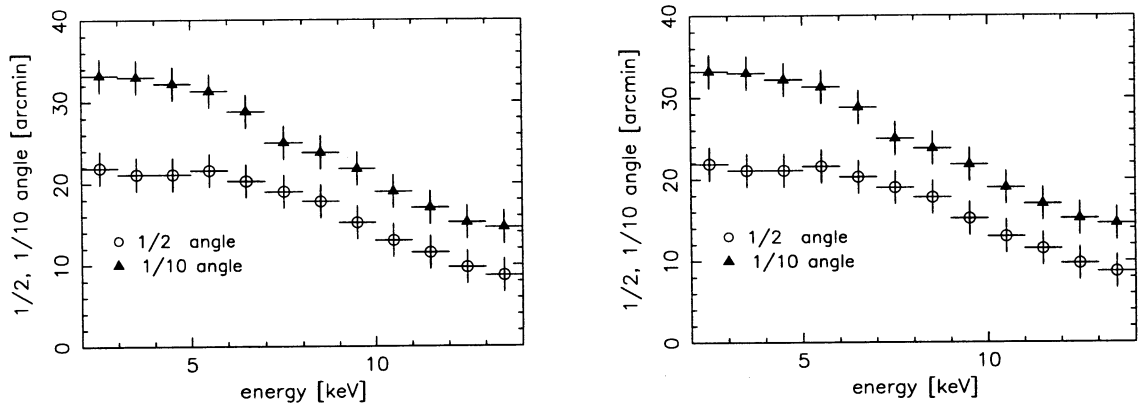

Figure 10. The energy dependence of field of view (left; θ_y scan, right; θ_z scan). 1/2 angle (open circles) implies the diameter when the efficiency becomes half of the on-axis value (i.e. field of view) and 1/10 angle (open triangles) represent the diameter when the efficiency becomes a order of magnitude smaller than that at the on-axis.

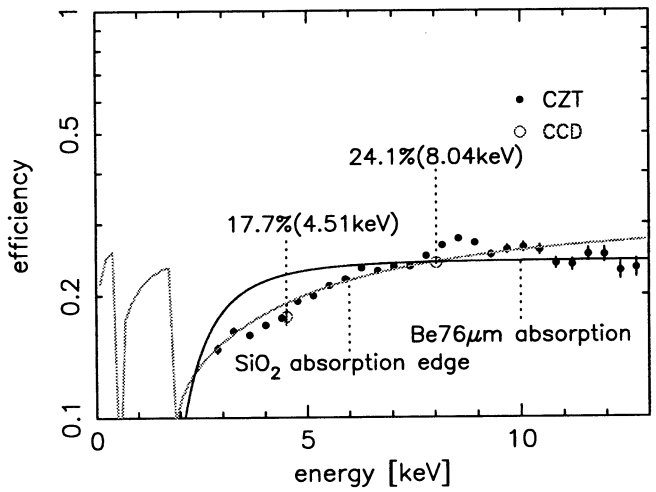

Figure 11. Transmission coefficient as a function of the incident photon energy; The data points are well fitted by the solid curve, which takes into account a grazing incident angle of $\theta = 0.05$ [deg] and 55 times number of reflection.

of capillary. Therefore we consider other absorption effects. Since capillary tubes are made from SiO_2, the absorption edge must appear at 1.8 [keV]. By considering the ideal case of capillary, we evaluated the mean grazing incident angle for tube to be $\sim$ 0.05 [deg]. Figure 11 shows our best fit model (grazing angle is 0.05 [deg], number of reflection is 55 times and the effective lens open area is 35 %). The data is well represented by this model, though the number of reflection is much larger than we expect based on the geometry of capillary. If the 55 times reflection occur, the path length of X-ray beam is much longer than the actual capillary length. This prompts the consideration of more complex configuration (e.g. waviness and roughness of inner wall of tubes) of capillary. Now we try to apply the ray-tracing program, which is basically designed to simulate the response of X-ray telescopes (e.g. Astro-E2).

5. SUMMARY

We carried out X-ray measurements of capillary at the X-ray beam facility of Institute of Space and Astronautical Science (Japan) where the sufficiently parallel X-ray beam is available.

The focal length and the depth of focus is 109.8 [mm] and 6 [mm], respectively, and the image size at the focal plane is 0.4 mm (FWHM) with 10 × 10 [mm^2] X-ray beam. The transmission coefficient is evaluated to be $\sim$ 20 % (17.7 %, 24.1 % at 4.51 keV and 8.04 keV, respectively).

From these results, we obtained flux amplification (gain) of capillary to be 155 and 110 at Cu-K_α and Ti-K_α, respectively.

The field of view was $\sim$ 22', 19' at 4.51 keV and 8.04 keV, respectively. The light-concentrating direction is distributed within $\sim$ 3' when the off-axis angles vary from -15' to +15'. This implies that the capillary can be utilized as a wide-filed-of-view optics in X-ray astronomy.

We are grateful to the X-ray Optical Systems Inc and Opt Science for kindly providing us to use this capillary, which is the key system to the wide field of view observations of celestial X-ray objects.

6. REFERENCES

1. C.H.Russel, "Application of polycapillary optics to hard x-ray astronomy", SPIE Vol. 3113, 1997
2. M.A.Kumakhov, "Advances in x-ray polycapillary optics", SPIE Vol. 3444, 1998
3. M.V.Gubarev, "Experimental investigation of the x-ray capillary system for hard x-ray astronomy", SPIE Vol. 3444, 1998
4. R.Shibata, "X-ray telescope onboard Astro-E. II. Ground-based x-ray characterization", Applied Optics Vol. 40, 2001
5. V.A.Arkadiev, "Method of investigating polycapillaries performance", SPIE Vol. 3115, 1997